NASA Contractor Report 198230

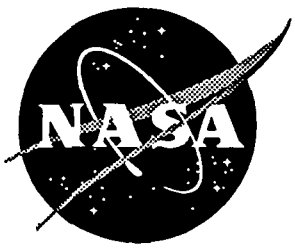

Time-Dependent Corrosion Fatigue Crack Propagation in 7000 Series Aluminum Alloys

Mark E. Mason
University of Virginia, Charlottesville, Virginia

Grant NAG1-745

October 1995

National Aeronautics and
Space Administration
Langley Research Center
Hampton, Virginia 23681-0001

TIME-DEPENDENT CORROSION FATIGUE CRACK PROPAGATION IN 7000 SERIES ALUMINUM ALLOYS

A Thesis

Presented to
the faculty of the School of Engineering and Applied Science

University of Virginia

In Partial Fulfillment
of the requirements for the Degree

Master of Science (Materials Science and Engineering)

by Mark E. Mason
December, 1994

"PAGE MISSING FROM AVAILABLE VERSION"

TIME-DEPENDENT CORROSION FATIGUE CRACK PROPAGATION IN 7000 SERIES ALUMINUM ALLOYS

ABSTRACT

The goal of this research is to characterize environmentally assisted subcritical crack (EAC) growth for the susceptible S-L orientation of aluminum alloy 7075-T651, immersed in acidified and inhibited NaCl solution. This work is necessary in order to provide a basis for incorporating environmental effects into fatigue crack propagation life prediction codes such as NASA-FLAGRO. This effort concentrates on determining relevant inputs to a superposition model in order to more accurately model environmental fatigue crack propagation (EFCP).

Time-based environmental crack growth rates from quasi-static load experiments in the 7075/NaCl system are an order of magnitude too small for accurate linear superposition prediction of da/dN for loading frequencies above 0.001 Hz. A combination of primarily intersubgranular fracture and overload fracture with few high angle boundary cracking features is observed for quasi-static EAC. Anodic dissolution to supply hydrogen to the crack tip process zone and the resulting hydrogen embrittlement (HE) are likely operative for EAC of 7075-T651 in chloride environments. Alternate methods for establishing da/dt, based on enhanced crack tip strain rate ($d\epsilon_{CT}/dt$) to disturb the passive film at the crack tip and enhance hydrogen production and uptake, do not provide a means of enabling linear superposition modeling of EFCP da/dN for frequencies above 0.001 Hz. Specifically, EAC da/dt is not enhanced for estimated crack tip strain rates

from 2 x 10^{-5} to 2 sec^{-1}, imposed by monotonic, ripple, and trapezoidal loading conditions. These observations indicate that passive film rupture may not be the rate limiting crack tip damage mechanism governing EAC of 7075-T651 in chloride.

Fatigue crack propagation rates in the 7075/NaCl system are enhanced five to ten-fold over da/dN in moist air and are over an order of magnitude faster compared to cracking in helium. EFCP da/dN show a weak time-cycle frequency dependence above 0.001 Hz (viz, $da/dN \propto f^{\beta}$, where ß is of order 0.1). The NaCl environmental effect on time-cycle-dependent EFCP, shown to be identical for acidified chromate inhibited and neutral uninhibited environments by comparison with literature results, is identical for the S-L and L-T orientations of 7075-T651, suggesting a minimal involvement of anisotropic high angle grain boundaries. Corrosion fatigue is predominantly intersubgranular for low frequencies and ΔK levels (below 0.1 Hz for ΔK of 9 MPa$\sqrt{m}$), while higher frequencies and ΔK levels produce primarily a transgranular fracture morphology. Compliance estimates of $K_{CLOSURE}$, and comparison with electrical potential based da/dN results, indicate a negligible effect of time-dependent crack closure on the frequency and rise time dependencies of da/dN for moderate ΔK. Trapezoidal loading EFCP experiments indicate a very small effect of hold-time (τ_H) at K_{MAX}. EFCP da/dN increases mildly with increasing loading rise time (t_R) from K_{MIN} to K_{MAX} for a wide range of loading waveforms, indicating that t_R is a more general parameter than frequency for analyzing time-dependent EFCP da/dN.

EFCP rates transition from time-cycle-independent to time-cycle-dependent

at a critical crack growth rate (da/dN_{CRIT}) and frequency (f_{CRIT}). Above f_{CRIT} shorter cycle periods provide less time for diffusion and accumulation of embrittling hydrogen in the process zone, and da/dN becomes time-cycle dependent. Derived from a model of crack tip hydrogen diffusion, a proportionality constant, γ_{CRIT}, relates da/dN_{CRIT} to $(f_{CRIT})^{-0.5}$, and includes the effect of diffusivity of hydrogen in aluminum (D_H), the critical concentration of hydrogen in the process zone for embrittlement (C_{CRIT}), and the concentration of hydrogen at the crack tip surface (C_S). The complex dependence of D_H, C_{CRIT}, and C_S on metallurgical, compositional, and environmental parameters may be qualitatively assessed, however, these parameters cannot be precisely determined from the results of this study. A combination of many possible rate-limiting processes involved in EFCP of 7000-T651(S-L) series aluminum alloys in chloride evidently controls time-cycle-dependent EFCP da/dN above f_{CRIT}. Results indicate the governing rate-limiting reaction changes with ΔK.

Fractographic comparisons indicate that the fracture mode undergoes a transition at identical da/dN_{CRIT} and f_{CRIT} for both 7017-T651(S-L) and 7075-T651(S-L) in chloride. Fracture modes for the S-L orientation of 7475-T651 and 7075-T651 differ, despite nearly equivalent time-cycle dependent EFCP da/dN and identical environments. EFCP of 7000-T651(S-L) series aluminum alloys in NaCl is governed by competitive fracture modes. The crack path that offers the least resistance to cracking, and is favored by process zone mechanics and environment conditions, is operative.

Linear superposition may be used to predict EFCP da/dN in the 7075-T651(S-L)/NaCl system for corrosion fatigue waveforms having K levels in excess of K_{ISCC} for more than 1000 seconds. A conservative approach using da/dN_{CRIT}, for frequencies above where da/dN_{SCC} becomes negligible, coupled with linear superposition below this frequency, is warranted for damage-tolerant life prediction for 7000 series aluminum alloys in aggressive chloride environments.

TABLE OF CONTENTS

LIST OF TABLES

LIST OF FIGURES

LIST OF SYMBOLS

α . . . . . proportionality constant
a . . . . . crack length
a_{ACTUAL} . . . . . optically measured crack length
a_{DCPD} . . . . . DCPD measured crack length
Δa . . . . . crack extension (growth)
B . . . . . specimen thickness
ß . . . . . slope of log EFCP da/dN versus frequency
C . . . . . input constant for ΔK decreasing procedure, linefit constant for da/dN versus ΔK data, Forman equation parameter
°C . . . . . degrees Celsius
C_{CRIT} . . . . . critical concentration of hydrogen in the process zone for HE
C_S . . . . . concentration of atomic hydrogen on the crack tip surface
δ . . . . . crack tip opening displacement
δ_0 . . . . . crack tip gage distance in surface strain model
da/dN . . . . . crack growth increment per fatigue cycle
da/dN_{AIR} . . . . . crack growth increment per fatigue cycle in air
da/dN_{CRIT} . . . . . critical crack growth increment per fatigue cycle
da/dN_{CF} . . . . . crack growth increment per fatigue cycle due to corrosion fatigue
da/dN_{MECH} . . . . . crack growth increment per fatigue cycle due to mechanical process zone damage
da/dN_{SCC} . . . . . crack growth increment per fatigue cycle due to SCC
da/dt . . . . . crack velocity, crack tip strain rate dependent velocity
da/dt_{II} . . . . . quasi-static load Stage II stress corrosion crack velocity
da/dt_{SCC} . . . . . quasi-static load stress corrosion crack velocity
$d\epsilon_{CT}/dt$ . . . . . crack tip strain rate
$d\epsilon_{CRIT}/dt$ . . . . . critical crack tip strain rate for enhanced da/dt
$d\epsilon_{TH}/dt$ . . . . . threshold crack tip strain rate for enhanced da/dt
dK/dt . . . . . change in stress intensity per unit time
D_H . . . . . diffusivity of hydrogen in aluminum
E . . . . . Young's modulus
ϵ . . . . . true strain
ϵ_F . . . . . fracture strain of oxide film
$\Delta\epsilon_P$ . . . . . cyclic crack tip plastic strain range
f . . . . . cyclic loading frequency
f_{CRIT} . . . . . critical frequency for hydrogen accumulation over Δx
γ_{CRIT} . parameter that includes D_H, C_S, and C_{CRIT} for an alloy/environment system
Hz . . . . . cycles per second
i . . . . . anodic current density
kN . . . . . kilonewton
K . . . . . linear elastic stress intensity
ΔK . . . . . cyclic stress intensity

K_0 . . . . . initial stress intensity, curve-fit parameter
K_{IC} . . . . . plane-strain fracture initiation toughness
K_{ISCC} . . . . . threshold stress intensity for stress corrosion cracking
K_{MIN} . . . . . minimum K during fatigue
K_{MAX} . . . . . maximum K during fatigue
K_{TH} . . . . . threshold stress intensity for crack growth in environment
ΔK_{TH} . . . . . ΔK threshold for fatigue crack growth in vacuum
L . . . . . rolling direction of rolled plate
m . . . . . meter, exponent for hold time dependence
ml . . . . . milliliter
mm . . . . . millimeter
mV_{SCE} . . . . . millivolts versus Saturated Calomel Electrode
MPa . . . . . megapascal
μA . . . . . microamp
μm . . . . . micron
n . . . . . Forman equation exponent
N . . . . . newton
ψ . . . . . direct current potential drop function fitting parameter
Ψ . . . . . potential drop function
p . . . . . Forman equation exponent
P . . . . . applied load
θ . . . . . fraction of crack advance due to chemical reaction
q . . . . . Forman equation exponent
Q . . . . . total anodic charge
ϕ . . . . . fractional area of crack undergoing pure corrosion fatigue
r . . . . . curve fit parameter
r_p . . . . . plastic zone diameter
R . . . . . stress ratio
σ . . . . . stress
σ_{YS} . . . . . yield strength
sec . . . . . second
S . . . . . short transverse direction of rolled plate
SEM . . . . . scanning electron microscopy
τ_H . . . . . hold time at K_{MAX}
Δt . . . . . change in time
t . . . . . time
t_b . . . . . time to onset of oxide formation
t_{FALL} . . . . . time from K_{MAX} to K_{MIN}
t_p . . . . . oxide film passivation time
t_r . . . . . time at passive film rupture
t_R . . . . . rise time from K_{MIN} to K_{MAX}
t_U . . . . . time from K_{MIN} to first unloading
T . . . . . long transverse direction of rolled plate
V . . . . . direct current potential drop measurement

V_o . . . . . reference direct current potential drop
wt pct . . . . . weight percent
W . . . . . WOL specimen thickness
Δx . . . . . crack advance increment per a number of fatigue loading cycles, ΔN

CHAPTER 1. BACKGROUND

1.1 PROBLEM

Determinations of the time dependence and crack tip damage mechanisms for materials such as 7075-T651 are required for effective modeling of environmental fatigue crack propagation (EFCP) rates in high strength aluminum alloys. Computer life prediction codes such as NASA FLAGRO empirically model the significant environmental enhancement of fatigue crack growth rates by line fitting fatigue crack growth rate (da/dN) versus stress intensity (ΔK) data using multiple adjustable parameters. [1] Describing time-dependent effects of ΔK and stress ratio (R) on the environmental enhancement of da/dN using empirical models requires a large data base and restricts component life prediction to well characterized material environment systems. The present research seeks to test the linear superposition model for 7075-T651 in aqueous chloride and to suggest improvements to the model based on a clearer understanding of the time dependencies in EFCP of 7075.

1.2 INTRODUCTION

Precipitation hardened high strength aluminum alloys were developed during the early 1940's for aerospace applications, with the first service for peak-aged 7075 in the B-29 bomber. [2] The high strength to weight ratio of these alloys led to widespread use in aircraft structural components. High strength Al-Mg-Zn and Al-Mg-Zn-Cu alloys, designated as 7000 series aluminum alloys, are susceptible

to time-dependent environment-assisted cracking (EAC) for both monotonic and cyclic loading conditions [3-5].

Environmental fatigue crack propagation rate depends on cyclic stress intensity, stress ratio, and a complex interaction of time and environmental variables. [3,6] Early life prediction efforts focused on the linear superposition model to predict trends in EFCP behavior using time-dependent monotonic environmental crack propagation kinetics coupled with mechanical fatigue behavior and loading conditions for high strength steels and aluminum alloy 7079-T6. [4,7] Mechanism-based approaches to model EFCP da/dN have been developed for several 7000 series aluminum alloys based on mass transport and hydrogen embrittlement effects. [8-10] To date, no model has emerged with wide applicability to chloride cracking of 7000 series aluminum alloys under fatigue loading conditions.

1.2.1 Stress Corrosion Cracking (SCC) of High Strength Aluminum Alloys

The quasi-static load environment assisted subcritical crack growth behavior of peak aged 7075 hot rolled plate in the S-L orientation is summarized in Fig 1.1, showing crack growth per unit time (da/dt) as a function of applied stress intensity (K). [4,5,11-13] EAC in this regard is generally intergranular. [5,14] Due to the anisotropic as-rolled plate grain structure, with many high angle grain boundaries oriented parallel to the rolling plane, the most severe monotonic load cracking for this alloy occurs due to tensile loading in the short transverse (S) direction with

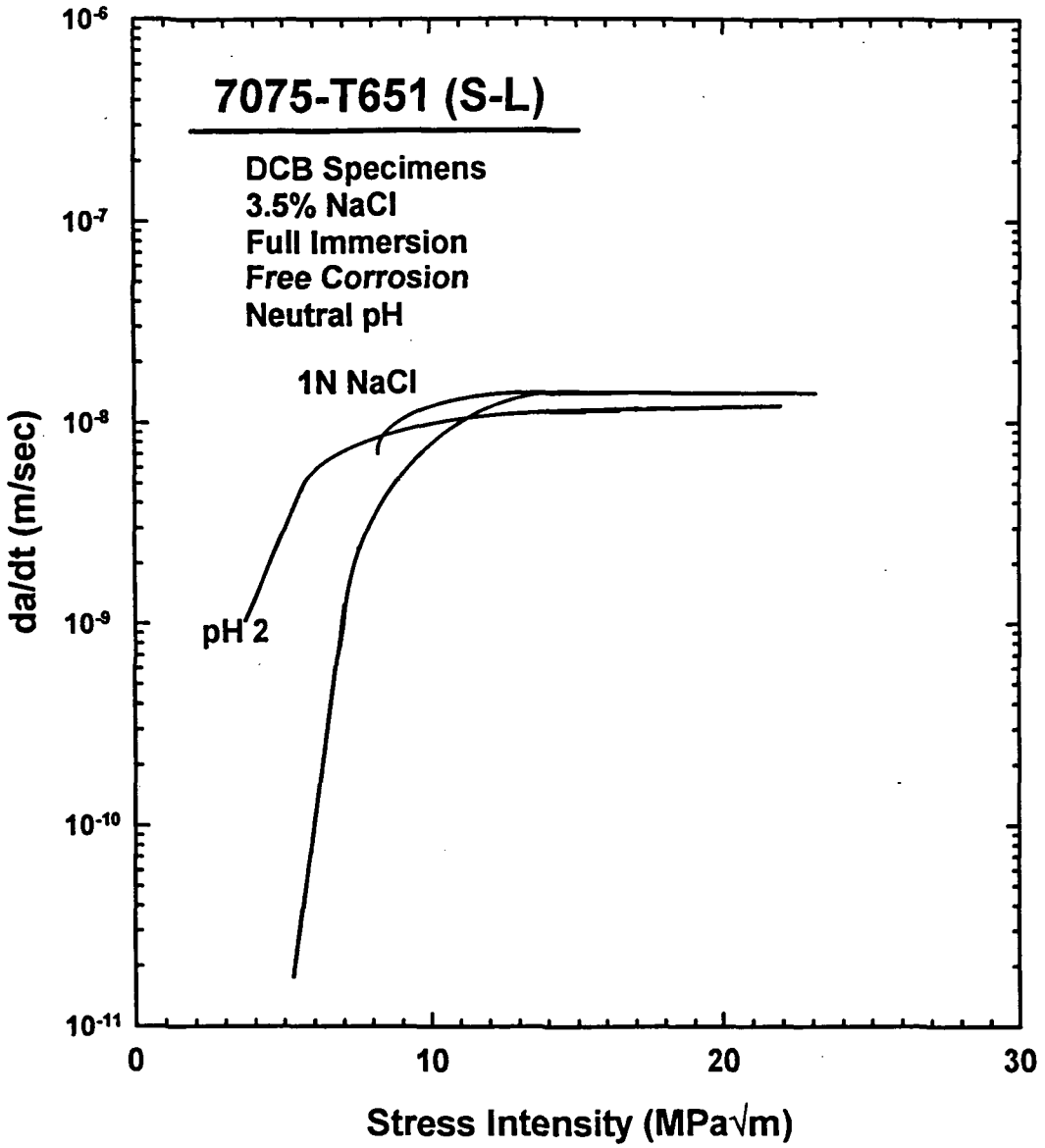

Fig. 1.1. Da/dt versus K for 7075-T651 in 3.5 wt pct NaCl. [4,5,11-13]

stress corrosion crack propagation in the rolling plane in the rolling (L) direction. Above an apparent threshold stress intensity of 5 to 10 MPa$\sqrt{m}$, crack growth rates transition to a K-independent (Region II) velocity (da/dt_{II}). The overaged 7075-T7351 temper is less susceptible to static load cracking than peak aged 7075-T651, with an order of magnitude slower da/dt_{II}. [4]

1.2.2 EFCP of High Strength Aluminum Alloys

Various factors affect EFCP da/dN for 7000 series aluminum alloys, including; cyclic stress intensity, stress ratio, orientation of high angle grain boundaries, microstructure, environment, loading frequency, and cyclic waveform. [3,4] The quasi-static load cracking sensitive peak-aged S-L orientation of 7075, 7079, 7017, and 7475 have been studied to evaluate the time dependency of da/dN in chloride environments. [4,9,10,15,16]

The threshold stress intensity for SCC (K_{ISCC}) relative to the plane-strain fracture initiation toughness (K_{IC}) and the magnitude of da/dt_{II} appear to determine the orientation sensitivity of EFCP, as noted by Kim and Manning. That is, da/dt_{II} must be on the order of or greater than the corrosion fatigue da/dt (approximated by (da/dt)(1/2f) through linear superposition), with adequate cycle time above K_{ISCC} to contribute to fatigue crack propagation (FCP). [17]

Physical metallurgical factors such as precipitate morphology and the distribution of alloying elements may affect the environmental cracking sensitivity of 7075. The nature and distribution of precipitates influence the slip

characteristics of 7000 series aluminum alloys and, via hydrogen embrittlement (HE), are believed to affect susceptibility to both SCC and CF. [14] Enhanced slip reversibility has been implicated in increased fatigue crack growth resistance in vacuum for 7475. [18] However, HE by hydrogen diffusion along localized slip bands in slow strain rate SCC tests has been proposed, leading to speculation of HE due to augmented hydrogen transport in the cyclic plastic zone during CF. [14,19] Dislocation transport of hydrogen has been disputed recently. [20] Alternate suggested hydrogen diffusion paths are dislocation core pipes and grain boundaries. [19] Segregation of Mg along grain boundaries, widely accepted to occur in the as-quenched condition, but uncertain for aged alloys, may increase the chemical activity at grain boundary sites and hence hydrogen entry at grain boundaries. [21] Mg segregation along grain boundaries has been implicated in increased intergranular environmental cracking sensitivity, both SCC and CF, for 7075-T651 in water vapor. [22]

The effects of solution chemistry and applied potential on EFCP were investigated for the L-T orientation of 7075 in chloride environments. Solutions containing halide ions (I, Br, and Cl) generally accelerate EAC. [4] Nitrate inhibitors have been shown to retard EFCP da/dN in chloride; nitrates, chromates, and fluorides inhibit crack growth in distilled water. [4] Investigators have successfully utilized low concentrations of sodium chromate in chloride environments to reduce corrosion products on fracture surfaces. [9,15] Chromate inhibitor reduces passive current density slightly (0.1 to 0.02 A/m^2) with negligible

decrease in EAC da/dt. [15] For uninhibited 3.5 wt pct NaCl environments, applied cathodic potentials less than -1000 mV_{SCE}, relative to open circuit (about -800 mV_{SCE}), decrease EFCP da/dN to dry air crack propagation rates while applied potentials greater than the pitting potential (about -200 mV_{SCE}) increase crack propagation rates. [23,24] For this research, it is important to note that the above studies showed negligible change in EFCP da/dN within ± 50 mV_{SCE} of the open circuit potential.

Loading frequency (f) affects EFCP rates for aluminum alloys such as 7075-T6 in full immersion chloride solutions at ambient temperatures. [4,9,11,15-17,25-27] Da/dN vs f data are summarized in Fig. 1.2, and demonstrate this strong and time-dependent environmental effect for several alloys.[1] [4,9,16,25,28] While da/dN is always frequency-independent for FCP in either vacuum or moist air at frequencies below 50 Hz, three frequency dependencies are observed for the chloride cases. As reviewed by Gangloff and Speidel, so-called *true corrosion fatigue* involves frequency-independent cracking at rates well above the benign environment values, as shown approximately for 7075-T73 in warm water and 7017 in seawater at 25°C for frequencies greater than 10 Hz. [3,4,10] Purely time-

---

[1] The data in Fig. 1.2 were obtained for constant applied ΔK, R, a sinusoidal loading waveform, and S-L crack orientation (loading is parallel to the plate thickness (S) direction and the crack growth direction is parallel to the rolling (longitudinal-L) direction). Modest variations from the constant solution chemistry of 2.5 to 3.5 wt pct NaCl, pH 7, aerated free corrosion potential, and 25°C are noted. All data were obtained for an applied ΔK of 15 MPa$\sqrt{m}$ with the exception of the results for 7075-T6.[15] These data were measured for a single ΔK of 9.5 MPa$\sqrt{m}$ (R=0.3) and extrapolated to 15 MPa$\sqrt{m}$ (R=0.1) by the Forman crack growth rate relationship.

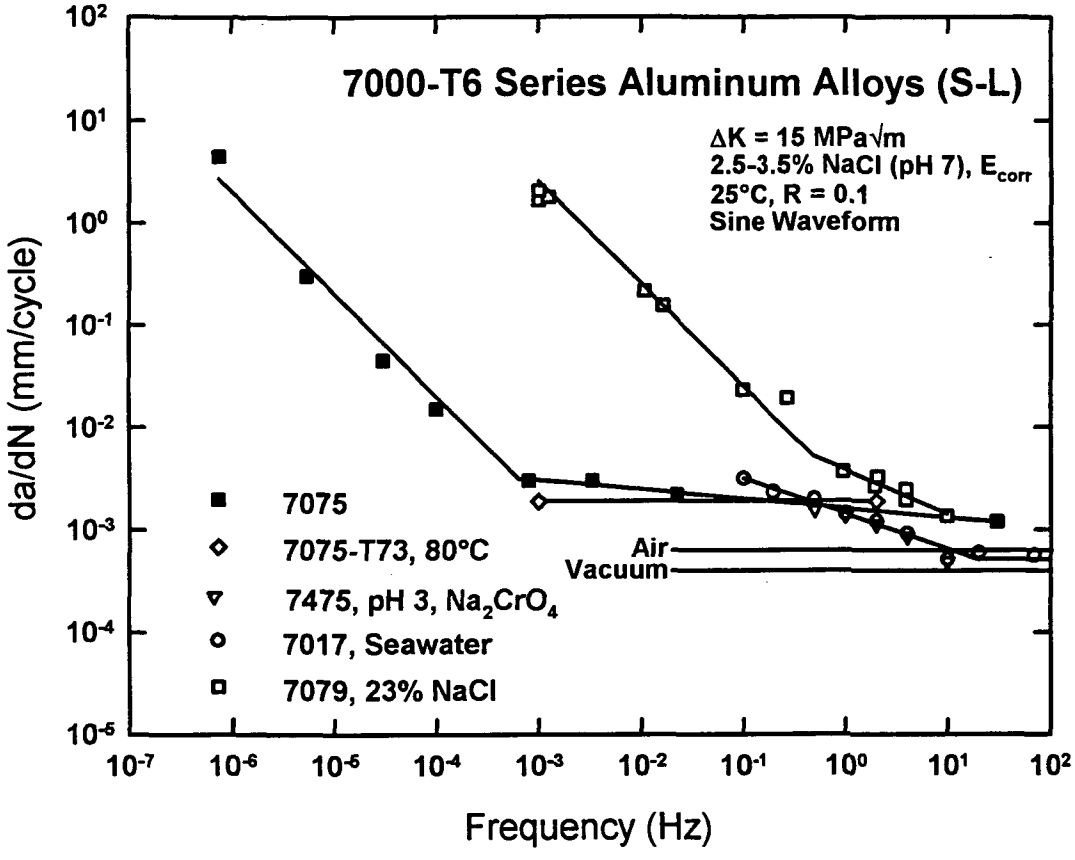

Fig. 1.2. Effect of frequency on da/dN in 7000-T6 series aluminum alloys in NaCl. [4,9,11,15-17,25-27]

dependent FCP is indicated by da/dN data that are proportional to 1/f for 7079 and 7075 at frequencies below 1 and 10^{-3} Hz, respectively. [4,15] Cycle-time dependent corrosion fatigue is characterized by $da/dN \propto f^{-\beta}$, where ß is on the order of 1/2, as observed for 7017 and 7475, and ß of 0.1 for 7075 below 10^{-3} Hz. [9,10,15] The underlying causes for the varied EFCP resistances and frequency dependencies shown for similar 7000 alloys in Fig. 1.2 are not understood.

Cyclic waveform affects EFCP rates for 7075-T651 in aqueous chloride environments. The time dependency of EFCP for the L-T orientation of 7075 has been investigated by varying fatigue loading cycle waveform to impose variable rise time to maximum load, hold time at peak load, and cycle unloading time. [27,29] Selines and Pelloux compared asymmetric waveforms with equal frequencies and variable loading and unloading times, revealing a weak rise time (t_R) dependence expressed as $da/dN = (\Delta K)^n(t_R)^m$ with m = 0.1, for the L-T orientation of 7075-T651 in 3.5 wt pct NaCl. [27] Analysis of independently generated data for sinusoidal loading conditions of 7075-T651 (L-T) in chloride (taking rise time as one-half a cycle period) confirms this trend for a symmetric waveform. [29,30] Similarly, a rise time dependence of m=0.1 was reported for a low alloy pressure vessel steel (A533B-1) in 90°C 3 wt pct NaCl and 90°C distilled water, while m = 0.3 was reported by Ouchi et al. for high strength steel in seawater. [31,32] The mechanistic nature of this time dependency is not clear.

Trapezoidal fatigue loading, with varying hold-time at constant maximum stress intensity (K_{MAX}), was employed to define da/dt vs K data that were useful in

predicting time-dependent EFCP rates in high strength steels and nickel-based superalloys. [29] The average time-based crack growth rate was calculated from the difference in measured da/dN at two τ_H values that differed by approximately 100 times using a linear superposition analysis of stress intensity as a function of time for the trapezoidal waveform. This analysis assumed crack propagation occurred only during time at $K > K_{ISCC}$. Da/dt determined at hold time at K_{MAX} was twenty fold faster than quasi-static da/dt for 300M steel. [29] The implication is that the crack tip strain rates associated with cyclic loading and unloading enhance da/dt over the quasi-static da/dt_{SCC}. In this same study, 7075-T6 (L-T) in chloride exhibited no measurable enhancement of da/dN for hold-times of 0.1 sec and 10 sec. [29]

1.2.3 Modeling EFCP for 7000 Series Aluminum Alloys

The EFCP frequency dependencies shown in Fig. 1.2 can be modeled based on empirical curve-fitting, linear superposition, or mass transport and chemical reaction kinetics. [3,7,33,34] The simple linear superposition approach may be applicable to EFCP in 7000-series aluminum alloys because of the low threshold stress intensity (K_{ISCC} or K_{TH}) of about 5 MPa$\sqrt{m}$ for such alloys, particularly in the S-L orientation. [4,14] This method equates the total environmental da/dN to the sum of the crack growth rate per load cycle due to fatigue damage in an inert environment (da/dN_{MECH}) and the contribution from time and K-dependent environmental cracking ($da/dt_{SCC}(K)$), integrated over a portion

of each fatigue cycle (τ) where K(t) exceeds K_{ISCC}:

$$\frac{da}{dN} = \frac{da}{dN_{MECH}} + \int_{\tau} [\frac{da}{dt_{SCC}}(K)] \, K(t) \, dt \qquad (1.1)$$

τ often defines the loading-only portion of the fatigue cycle where process zone stresses are always tensile. Traditionally, da/dt_{SCC} has been determined by either constant load or constant crack mouth opening displacement experiments, and is K-independent for aluminum alloys in chloride above K_{ISCC}, Fig. 1.1. [14] For this case, and when da/dN_{MECH} is a small fraction of da/dN, Eq. 1.1 leads to the prediction that da/dN depends on 1/f, as observed for 7079 in NaCl (at frequencies less than 1 Hz) and for 7075 (at f < 0.001 Hz, Fig. 1.2). For these two cases, linear superposition provides an effective means of predicting the effects of ΔK, R, f, hold time and wave form on environmental da/dN.

Holroyd and Hardie demonstrated that linear superposition was incapable of describing the magnitude of da/dN and the frequency dependence of FCP for 7017 in seawater (Fig. 1.2). [25] Although K_{ISCC} was low, da/dt_{SCC} from quasi-static load testing was too small to account for the necessary time-dependent enhancement over da/dN_{Mech} through Eq. 1.1. For this case, the time-dependence was considered based on:

$$\frac{da}{dN} = \frac{da}{dt} \frac{1}{\alpha f} \qquad (1.2)$$

where da/dt is the average time-based crack growth rate during a fraction ($1/\alpha$) of the load cycle and may be frequency-dependent. If da/dt increases with increasing frequency, raised to a power (n) on the order of one-half, then da/dN

will vary with $f^{(n-1)}$ or $f^{-\beta}$, as indicated in Fig. 1.2.[2]

The implication of this argument is that da/dt should be measured for crack tip strain rates typical of FCP; quasi-static load experiments may not yield relevant time-based crack growth rates for modeling EFCP da/dN. For example, da/dt could be determined from EFCP experiments conducted with several hold times and analyzed with Eq. 1.1. [29] Alternately, da/dt could be measured by a rising load or rising displacement method that systematically varies crack tip strain rate and stress intensity; the issue is whether such growth rates exceed da/dt_{scc} determined from quasi-static load or displacement experiments. [35] Strain rate-dependent da/dt (proportional to f^{n}) is understandable from the film rupture and transient dissolution/repassivation perspective. [36] Both this mechanism and hydrogen environment embrittlement must be considered to predict time-cycle-dependent EFCP. [3,34,36]

If da/dt_{scc} is not enhanced sufficiently by increased crack tip strain rate, then time-cycle-dependent EFCP da/dN must be governed by other rate controlling crack propagation mechanisms. Wei and coworkers suggested adding a term to the linear superposition model, da/dN_{CF}, representing so called "pure" corrosion fatigue, the synergism of environmental and cyclic loading conditions. Da/dN_{CF} is the crack growth rate for the fraction of the fracture surface where crack propagation is environment-enhanced according to a mechanistic model for EFCP.

---

[2] For purely time-dependent EFCP, da/dt is independent of f and da/dN depends on $1/\alpha f$, as expected from linear superposition.

[8] Da/dN_{CF} is time-cycle-independent for constant ΔK if the crack propagation mechanism is not rate limited.

1.3 OBJECTIVE

The objectives of this research on an EAC-susceptible 7000-series aluminum alloy in aqueous chloride are four-fold: (1) to test static load or displacement-based linear superposition predictions of da/dN vs ΔK and f, (2) to determine if da/dt_{scc} is sufficiently affected by crack tip strain rate to enable improved linear superposition predictions of da/dN, (3) to broadly determine the frequency, load waveform and hold-time dependencies of da/dN, and (4) to speculate on the metallurgical and electrochemical origin(s) of the important variability shown in Fig.1.2. The output of this work will be improved data and understanding on time-cycle-dependent EFCP kinetics for use in component fatigue life prediction codes such as NASA-FLAGRO.

1.4 APPROACH

Constant stress intensity and constant crack mouth opening displacement (CMOD) experiments are performed on the S-L orientation of 7075-T651 in a chromate inhibited acidified chloride environment for comparison with published da/dt_{ii} for 7075-T651 in chloride. Stress intensities are chosen to provide quasi-static EAC fracture surfaces to compare with fatigue and ripple load fracture surfaces at equivalent stress intensities.

Experiments are conducted to explore the effect of applied crack tip strain rate on da/dt for 7075-T651 in sodium chloride. Rising load R-curve-type experiments are utilized in addition to high frequency, low ΔK "ripple" loading. These experiments are designed to increase the strain rate at the crack tip and to determine whether the imposed higher strain rates accelerate environmental damage above quasi-static load da/dt_{scc} values.

Corrosion fatigue crack growth rates at several constant stress intensities are determined from crack lengths measured by the direct current potential difference technique over a wide (10^{2}-10^{-2} Hz) frequency range and for five loading wave forms. Decreasing ΔK experiments are performed under sinusoidal loading at 5 Hz in chloride and air to characterize the da/dN vs ΔK behavior for a wide range of stress intensities.

The linear superposition model is applied to 7075-T651 (S-L) in chloride using da/dt_{scc} measured for environmentally enhanced static load cracking and da/dN versus ΔK for an inert environment. Aspects of the time dependencies in EFCP are explored utilizing crack tip strain rate models. Suggestions are made for modeling EFCP in aluminum alloy 7075.

CHAPTER 2. EXPERIMENTAL PROCEDURE

2.1 MATERIAL

Al-Zn-Mg-Cu alloy 7075 was obtained from the Aluminum Company of America (ALCOA) as 52 mm thick rolled plate. Material was studied in the peak aged, T651 condition (hot rolled, solution heated, stretched 1.5 to 3% permanent set, aged 24 hours at 120 to 124°C, and air cooled). Chemical composition and mechanical properties are given in Table 2.1. The optical micrographs shown in Fig 2.1 reveal large flattened grains elongated in the rolling direction. Average grain dimensions in the longitudinal (L), transverse (T), and short transverse (S) directions are 1 mm, 200 μm and 10 to 50 μm, respectively. This material was previously studied in an ASTM interlaboratory test program on stress corrosion cracking. [37]

Table 2.1: Nominal Chemical Composition and Mechanical Properties of 7075-T651

Chemical Composition (wt pct)

Zn	Mg	Cu	Cr	Mn	Ti	Fe	Si	Al
5.1-6.1	2.1-2.9	1.2-2.0	0.18-0.4	0.3*	0.2*	0.7*	0.5*	bal.

* Maximum wt pct

Mechanical Properties

Yield Strength MPa (ksi)*	Tensile Strength MPa (ksi)*	Elongation Pct*	K_{IC}, MPa$\sqrt{m}$ (ksi$\sqrt{in}$)**
472 (68.4)	540 (78.2)	4.0	22.2 (19.3)

* Loading axis parallel to L. ** S-L orientation.

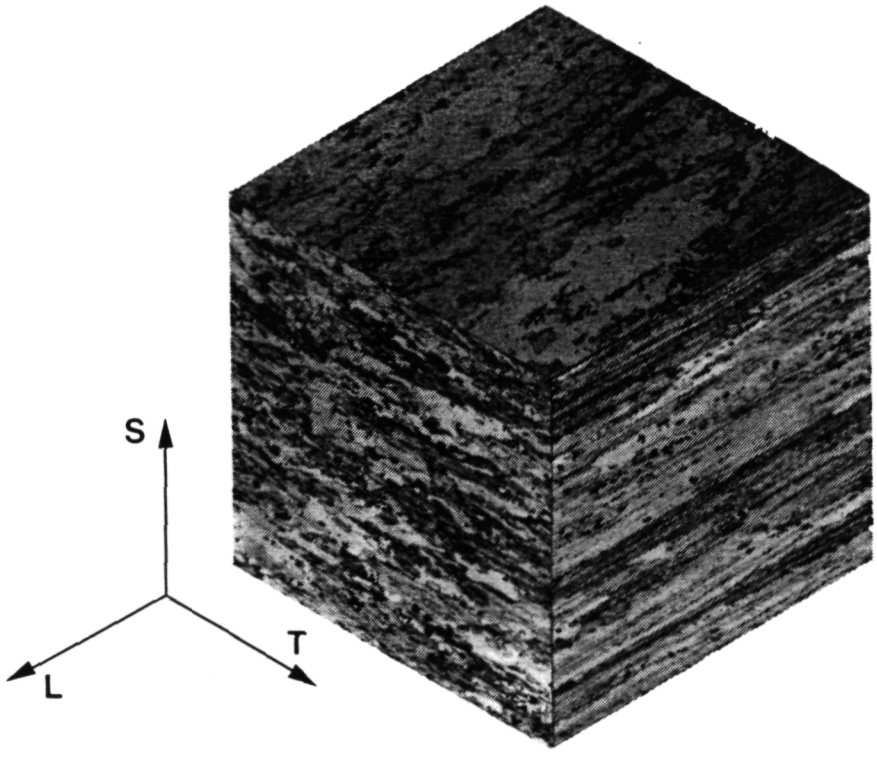

Fig. 2.1. Representative microstructure of AA7075-T651 (52X).

2.2 EAC EXPERIMENTS

A closed loop servohydraulic MTS 810 Material Test System (50 kN load frame with 50 kN load cell and MTS model 458.20 microconsole controller) was interfaced with PC-based Fracture Technology Associates (FTA) software to provide all quasi-static load and fatigue crack propagation rate test conditions. Specimens were ultrasonically cleaned in acetone using a Bransonic model 2200 ultrasonic cleaner for at least 5 minutes to remove any machining debris and oils before testing.

2.2.1 Stress Intensity Calculation

All experiments utilized fracture mechanics methods applied to the wedge-opening-load (WOL) precracked specimen (illustrated in Fig. 2.2) machined from the plate in the S-L orientation. Holes were tapped in specimens to accommodate a working electrode and grounding leads as well as load-line current and front face potential leads. Knife edges were machined in the specimen front face to accommodate a displacement gage. The locations of this instrumentation on the WOL specimen are indicated in the schematic shown in Fig 2.3. Specimens were mounted in the load train via clevises with roller bearings at the load pins to provide free rotation. Applied stress intensity (K) is calculated from measured load and crack length with the standard elastic solution [38]:

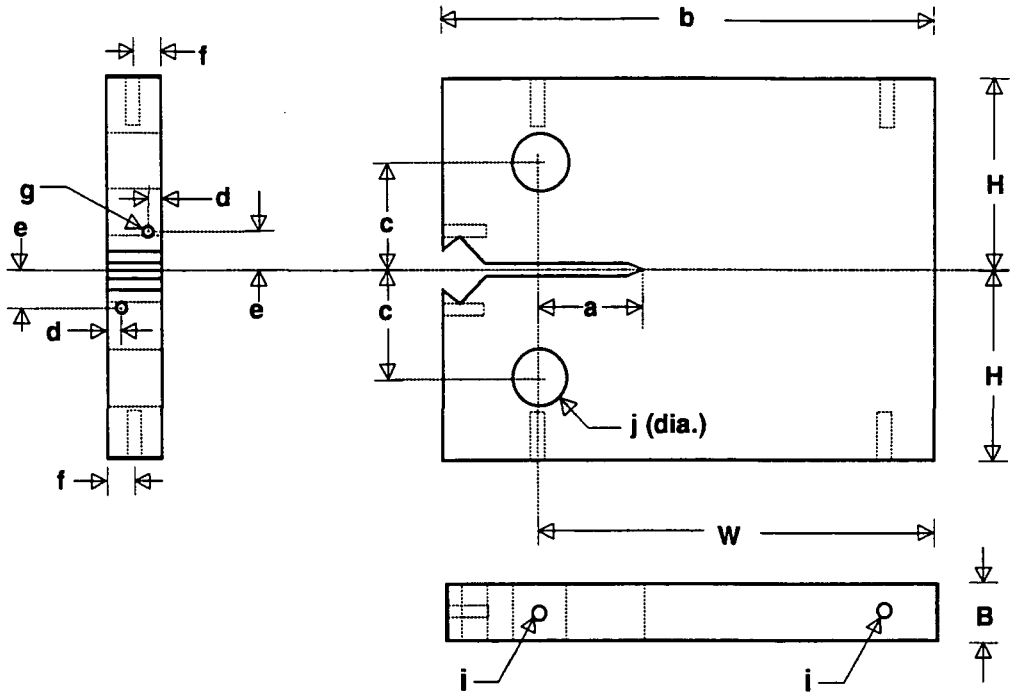

Notch Detail

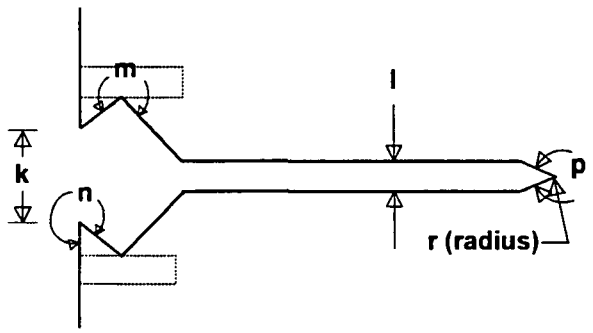

angle	deg	tol.
m	75	±15
n	50	±10
p	30	± 1

	Dim. (mm)	tol.(mm)
a	13.06	± 0.15
b	65.60	± 0.15
H	24.50	± 0.15
W	52.30	± 0.15
B	7.62	± 0.03
c	14.00	± 0.15
d	1.50	± 0.15
e	4.60	± 0.15
f	3.80	± 0.15
k	5.08	± 0.03
l	1.50	± 0.15
r	0.25	± 0.15

hole	spec.	size
g	tapped	2-56
i	tapped	8-32
j	smooth	7.60 ± 0.15 mm

Fig. 2.2. Wedge-opening-load specimen geometry.

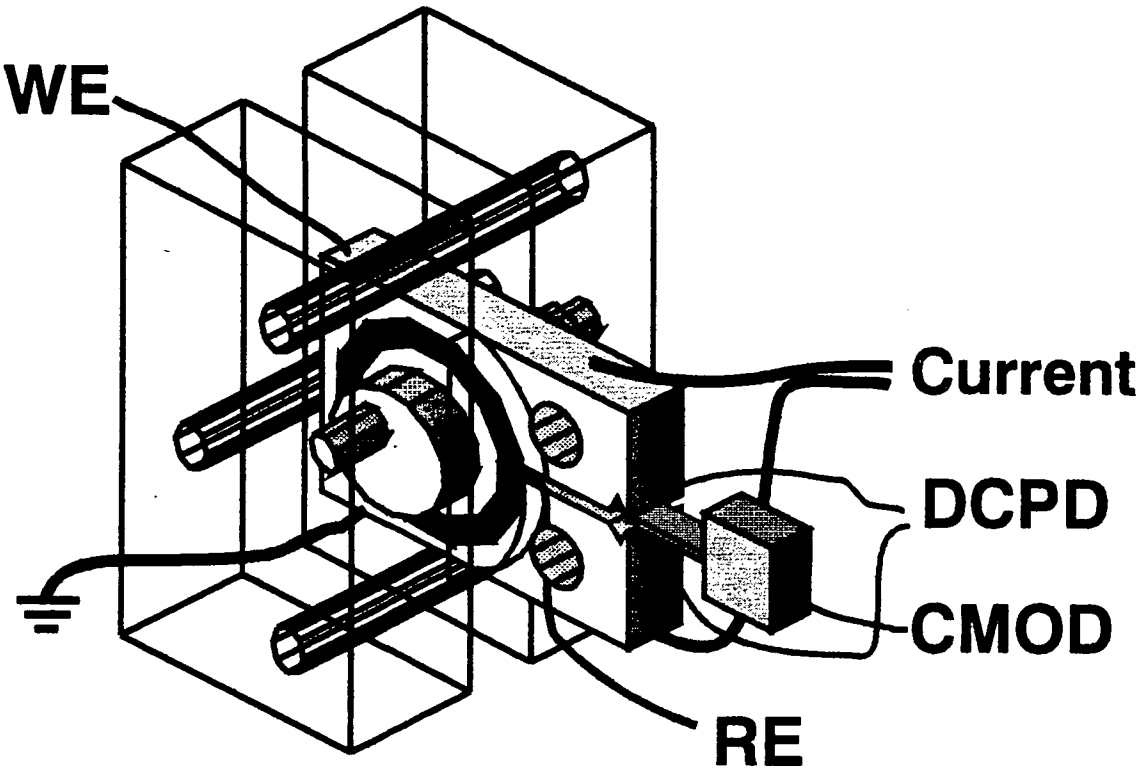

Fig. 2.3. Schematic showing specimen and environmental cell configuration.

$$K = \frac{P}{B\sqrt{W}} F\left(\frac{a}{W}\right) \tag{2.1}$$

$$F\left(\frac{a}{W}\right) = \frac{\left(2+\frac{a}{W}\right)}{\left(1-\frac{a}{W}\right)^{\frac{3}{2}}} \left[0.8072 + 8.858\left(\frac{a}{W}\right) - 30.23\left(\frac{a}{W}\right)^2 + 41.088\left(\frac{a}{W}\right)^3 - 24.15\left(\frac{a}{W}\right)^4 + 4.951\left(\frac{a}{W}\right)^5\right] \tag{2.2}$$

where a = crack length, W = specimen width, B = specimen thickness, and P = applied load.

2.2.2 Crack Length Measurement

The direct current potential difference (DCPD) technique was used to monitor crack length in the WOL specimens. [39] Current leads were attached to the WOL specimen on the top and bottom faces along the load-line. A constant direct current of 10 amperes (± 0.005 A) was applied to the specimen with a Hewlett Packard 6264B power supply. Potential leads were attached with machine screws to the specimen front face approximately 9 mm apart across the notch opening and covered with a small bead of epoxy to further secure the leads. Potential across the crack mouth was then amplified 10^4 times by a Measurement Groups model 2310 signal conditioning amplifier, and corrected for metal-metal contact thermal voltages by reversing current polarity during potential

measurement via a solid state current relay and subtracting thermal voltages. Potential was continuously monitored with the PC based data acquisition system which also controlled the relay and current polarity reversal.

A standardized polynomial equation for the compact tension specimen, relating crack length to potential, was used to determine crack length [39]:

$$\frac{a}{W} = -0.5051 + 0.8857\left(\Psi\frac{V}{V_0}\right) - 0.1398\left(\Psi\frac{V}{V_0}\right)^2 + 0.0002398\left(\Psi\frac{V}{V_0}\right)^3 \quad \textbf{(2.3)}$$

where V is potential, V_0 is the reference potential for a known crack length, and Ψ is the potential drop adjustment function (Eq. 2.5) used only during data analysis (Ψ = 1 during experiments). For experiments which did not utilize Fracture Technology Associates (FTA) fatigue software, V_0 was determined by measuring V for a known crack length such as the fatigue precrack and substituting these values into:

$$\frac{V}{V_0} = 0.5766 + 1.916\left(\frac{a}{W}\right) - 1.0712\left(\frac{a}{W}\right)^2 + 1.6898\left(\frac{a}{W}\right)^3 \quad \textbf{(2.4)}$$

For experiments utilizing FTA fatigue software, visual crack length measurements were made of one or more markings on the fracture surfaces (aided by macroscopic differences in fatigue fracture surface morphology) using Image-Pro Plus image analysis software interfaced with a video camera with a 10-times magnification zoom lens. Specimen thickness, as measured by a micrometer, was used to calibrate the image analysis software. The visual crack length measurements were input into the analysis software along with the corresponding

V values and the V_0 used during the experiment. The function Ψ, having the form:

$$\Psi = \psi V + \Psi_0 \qquad (2.5)$$

was inserted into Eq. 2.3, and ψ and Ψ_0 were calculated to minimize the error between visual crack length observations and crack lengths predicted by equation 2.3 using measured V and test V_0 as inputs. The constants ψ, Ψ_0, and V_0 as well as measured V were applied to Eqs. 2.5 and 2.3 to calculate corrected crack lengths.

For experiments which did not use FTA fatigue software, crack lengths were calculated using a visually measured precrack length to determine V_0 ($\Psi = 1$) and da/dt determined by least squares fitting of the resulting crack length versus time data.

Comparison of post-test crack length measurements, observed at transitions in fracture surface appearance, with uncorrected values given by DCPD during each experiment are shown in Fig. 2.4. DCPD values are within ±20% of actual crack lengths for most cases, with only two measurements (on two separate specimens) having an error in predicted crack length greater than 20%. Approximately 16 specimens are represented in Fig. 2.4.

2.2.3 MONOTONIC LOADING

2.2.31 Constant Load Line Displacement Rate

Experiments to determine the effect of high load line displacement rates on

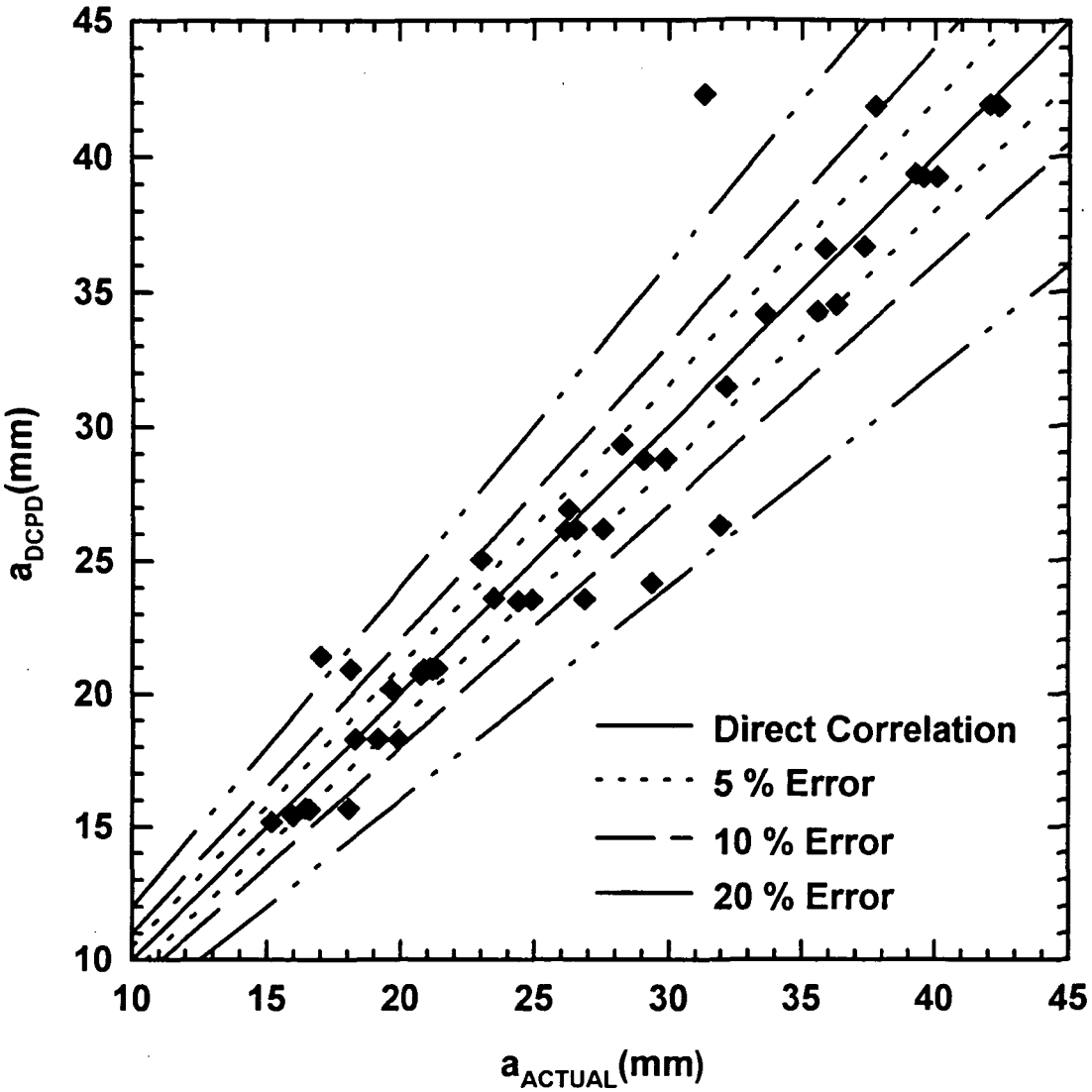

Fig. 2.4. Comparison of post-test crack length measurements, a_{ACTUAL}, with uncorrected DCPD values, a_{DCPD}.

environmental da/dt and K_{TH} were performed at several CMOD rates (CMOD rate and load-line displacement rate are proportional by geometric conversion). Constant displacement rate, as measured by a clip gage at the specimen front face and controlled by FTA monotonic loading software, was utilized to determine the stress intensity at the onset of cracking, K_{TH}, with DCPD measurements utilized to measure crack length. K_{TH} was determined at first deviation of DCPD versus displacement values combined with a corresponding decrease in specimen compliance.

2.2.32 Constant Load Line Displacement

Crack growth under constant load line displacement was used to determine da/dt versus K behavior. Load line displacement was maintained constant by a clip gage at the specimen front face, with the load interactively varied to produce the desired CMOD by FTA monotonic loading software. DCPD, time and load were recorded by computer for data analysis.

2.2.33 Constant Stress Intensity

Fracture mechanics fatigue software was utilized to apply constant stress intensity to the specimen by specifying a ΔK of 0 and R=1. Any deviation from constant $\Delta K = 0$ was due to noise in the load signal, which was less than ± 0.005 V (or $\pm$ 4.45 N for the 890 N/V range used, equivalent to $\Delta K = 0.1$ MPa$\sqrt{m}$ at the a/W of 0.7 limit of validity of Eq. 2.3). Crack length was measured every 5 to 15

minutes with the average potential over each crack extension increment written to a data file for specified increments of 0.10 to 0.03 mm. Due to differences in the DCPD crack lengths and the actual crack lengths, "constant" stress intensity varied by as much as 10 to 20% for the duration of each experiment.

2.2.4 Ripple Load

Ripple load testing was performed under computer control using FTA fatigue testing software maintaining constant K (static) or K_{MAX} and ΔK (ripple load) for segments of crack extension of at least 1 mm. The average DCPD value over every 5 μm increment of crack advance (approximately every 20 minutes at da/dt of 4 x 10^{-9}m/sec), as well as the average cycle number for the crack growth increment (corresponding to time), were recorded by computer. Fracture surfaces between constant K and ripple loading intervals were marked by fatigue loading at a K_{MAX} equivalent to the following ripple loading K_{MAX} and at an R of 0.1. Results are presented as a plot of crack length versus time.

2.2.5 Fatigue

FTA fatigue testing software was employed for all EFCP experiments. Fatigue crack propagation was measured in stress intensity control with load and DCPD providing active feedback for constant applied stress intensity under variable waveform and loading frequency. Two constant ΔK, variable frequency experiments were conducted using FTA compliance based crack length and

control software which provided for measurement of da/dN-ΔK, closure stress intensities, ΔK_{EFF} and da/dN-ΔK_{EFF} according to standardized procedures.[3] [40]. Otherwise, visually corrected DCPD crack lengths using Ψ (Eq. 2.3) to minimize errors were employed for calculations of da/dN and ΔK.

2.2.51 Fatigue Precracking

All specimens were fatigue precracked under constant ΔK conditions of 6 to 9 MPa$\sqrt{m}$ and R of 0.1 to an a/W of approximately 0.3. Precrack ΔK was equal to or less than the first applied ΔK after the precrack, or K_{MAX} was less than the first applied initial stress intensity (K_o). All specimens were precracked in the chloride environment with the exception of the three constant displacement rate experiments.

2.2.52 ΔK Decreasing

Two experiments, one in the chloride environment and one in moist laboratory air, utilized the ΔK decreasing method with constant R (0.1) and K_{MAX} defined by:

$$K_{MAX} = K_{MAX_0} \exp[C(a - a_0)] \qquad (2.6)$$

where K_{MAX} is the maximum stress intensity corresponding to crack length a, K_{MAXo} is the initial maximum stress intensity at a_o, and C is an input constant, equal to -0.059 mm^{-1} and -0.075 mm^{-1} for the chloride and moist air experiments,

---

[3] This work was performed by Mr. Edward Richey, III.

respectively. The specimen dimensions, precracking, ΔK decreasing procedures, and calculation of da/dN conform to ASTM Standard E647-91 (Standard Test Method for Measurement of Fatigue Crack Growth Rates). [40] After completion of each ΔK experiment, the specimens were fractured in air, and visual measurements of initial and final crack lengths were used to calculate ψ and Ψ_o for correcting crack length and ΔK. ΔK decreasing experiments utilized the secant method to determine da/dN.

2.2.53 Constant ΔK: Variable Frequency and Waveform

Constant ΔK EFCP experiments were conducted in load control, varying loading frequency and waveform over crack length increments of at least 2.5 mm as measured by DCPD or unloading compliance, with six to eight frequency segments per specimen. Constant ΔK was computer-maintained by monitoring crack length and adjusting the load waveform. The FTA machine control software accommodated a variety of cyclic loading frequencies, hold-times and waveforms. [41] This procedure allows measurement of steady state EFCP growth rates at fixed ΔK and R, distinguishes small differences in da/dN, and provides a qualitative indication of crack closure. Changing loading conditions often marked the fracture surface for post-test visual observations to facilitate calculation of ψ and Ψ_o. Da/dN for these experiments was calculated via linear regression of corrected DCPD crack length versus loading cycles, N. Two sinusoidal waveform, variable frequency, experiments were conducted utilizing compliance-based crack length

measurements during which closure stress intensities were measured. Frequencies varied from 0.01 Hz to 40 Hz and sinusoidal, trapezoidal, and symmetric and asymmetric triangle waveforms were utilized.

2.2.6 Environment

The polymethyl methacrylate (PMMA) environmental cell shown in Fig 2.3 was used to fully immerse the crack tip in an aerated solution of deionized water, 2.5 wt pct NaCl, 0.5 wt pct Na_2CrO_4, and dropwise added HCl to decrease bulk pH to 3. Solution pH changed by less than ± 0.2, as determined by post-experiment measurements for all experiments. Between experiments, the solution was replaced with a freshly made environment when pH exceeded the $\pm$ 0.2 limit. A single experiment, performed using unloading compliance based crack length measurement, used an environment of 2.5 wt pct NaCl and deionized water without acidification or the chromate inhibitor.

Solution was circulated continuously at 1 ml/sec through the cell and specimen notch parallel to the crack front from a 1 liter reservoir. All experiments were conducted at the open circuit condition, without galvanic coupling of the grounded WOL specimen and test machine. Throughout each experiment, a chloridized silver reference electrode, located within the notch at the specimen midplane, monitored electrode potential which varied by less than $\pm$ 50 mV about -770 mV_{SCE}.

2.3 FRACTOGRAPHY

Fractographic analysis was performed on fracture surfaces using a JEOL JXA-840A Electron Probe Microanalyzer/Scanning Electron Microscope (SEM). Specimens were coated with acrylic spray to protect the fracture surfaces while machining specimens to a size that the microscope could accommodate. SEM specimens were cleaned in acetone using a Bransonic model 2200 ultrasonic cleaner. Stereoimaging was accomplished by taking one micrograph, tilting the specimen 7° about the microscope stage y axis, realigning the specimen to maintain the same field of view, refocusing, and photographing the tilted image.

CHAPTER 3. RESULTS

3.1 MONOTONIC LOAD EAC

3.1.1 Quasi-Static Load Cracking

3.1.11 Background

The quasi-static load/CMOD stress corrosion cracking behavior of 7075, in the susceptible S-L orientation and T651 temper, is summarized by the literature results in Fig. 1.1. [5,12,13] For full immersion (FI) in neutral and pH 2 NaCl at free corrosion electrode potentials, SCC is characterized by K-independent cracking at a rate of about 10^{-6}m/sec, transitioning to a threshold between 5 and 10 MPa$\sqrt{m}$. Extensive long-term results from multiple-laboratory testing of 7075-T651 (S-L) in 3.5 wt pct NaCl (FI) compare favorably with the results in Fig. 1.1.[42]

In contrast to the data in Fig. 1.1, Colvin et al. reported an approximate da/dt_{scc} of 5 x 10^{-9} m/sec based on alternate immersion (AI) aqueous NaCl exposure of this same heat of 7075 (Table 2.1) in the T651 temper and for constant displacement. [37] Rechberger reported that da/dt_{scc} equaled 2 x 10^{-9} m/sec at a K of 10 MPa$\sqrt{m}$ and increased to 1.5 x 10^{-8} m/sec at 18 MPa$\sqrt{m}$ for 7075-T651 (S-L) in neutral NaCl (FI) and at constant load; SCC was not K-independent. [15]

3.1.12 Crack Growth Rate Results

Several constant stress intensity segments of crack growth were used to

determine quasi-static crack growth rates, da/dt_{scc} in the Stage II K-independent region. The results of these experiments are summarized in Table 3.1 and presented in Fig. 3.1 for comparison with literature results from Fig. 1.1. The slope of a least squares linear regression line, fit to corrected DCPD crack length versus time data (da/dt_{scc}), is given in Table 3.1; as well as the stress intensity range calculated from post-test corrected crack lengths. (Errors in crack length, as measured by DCPD, account for variations from constant K). Table 3.1 shows the total crack growth increment measured visually using image analysis, Δa, the time

Table 3.1 - Crack growth and growth rate measurements of quasi-static EAC of 7075-T651(S-L) in aqueous chloride.

Control Mode	Specimen	Δa (mm)	Δt (sec)	$\Delta a/\Delta t$ (mm/sec)	Linear Regression da/dt_{scc} (mm/sec)	K (MPa$\sqrt{m}$)
const CMOD	T6-04	2.94	675400	4.4×10^{-6}		20.3-20.1
const K	T6-07	1.43	410454	3.5×10^{-6}	4.0×10^{-6}	11-13
const K	T6-23	1.61	527814	3.0×10^{-6}	3.4×10^{-6}	17.3
const K[4]	T6-23	0.2-1.5	469160-469248	$0.3 - 3.0 \times 10^{-6}$	$0.5 - 2.0 \times 10^{-6}$	9.0

duration of the constant K segment, Δt, and $\Delta a/\Delta t$ calculated from these two values for comparison with da/dt_{scc} determined by linear regression. Note the long duration of each experiment, the modest amount of subcritical crack extension and

[4] Linear regression produced a poor fit of a straight line to these a(N) data. Approximately 90% of the crack growth for this segment occurred in the first hour at 9 MPa$\sqrt{m}$ (da/dt of 2×10^{-4} mm/sec) with the remaining 10% of growth over 130 hours (da/dt of 5×10^{-7} mm/sec). The former result may be due to complex effects of crack surface electrical shorting while the later indicates K-dependent Stage I da/dt with K_{Iscc} of about 9 MPa$\sqrt{m}$.

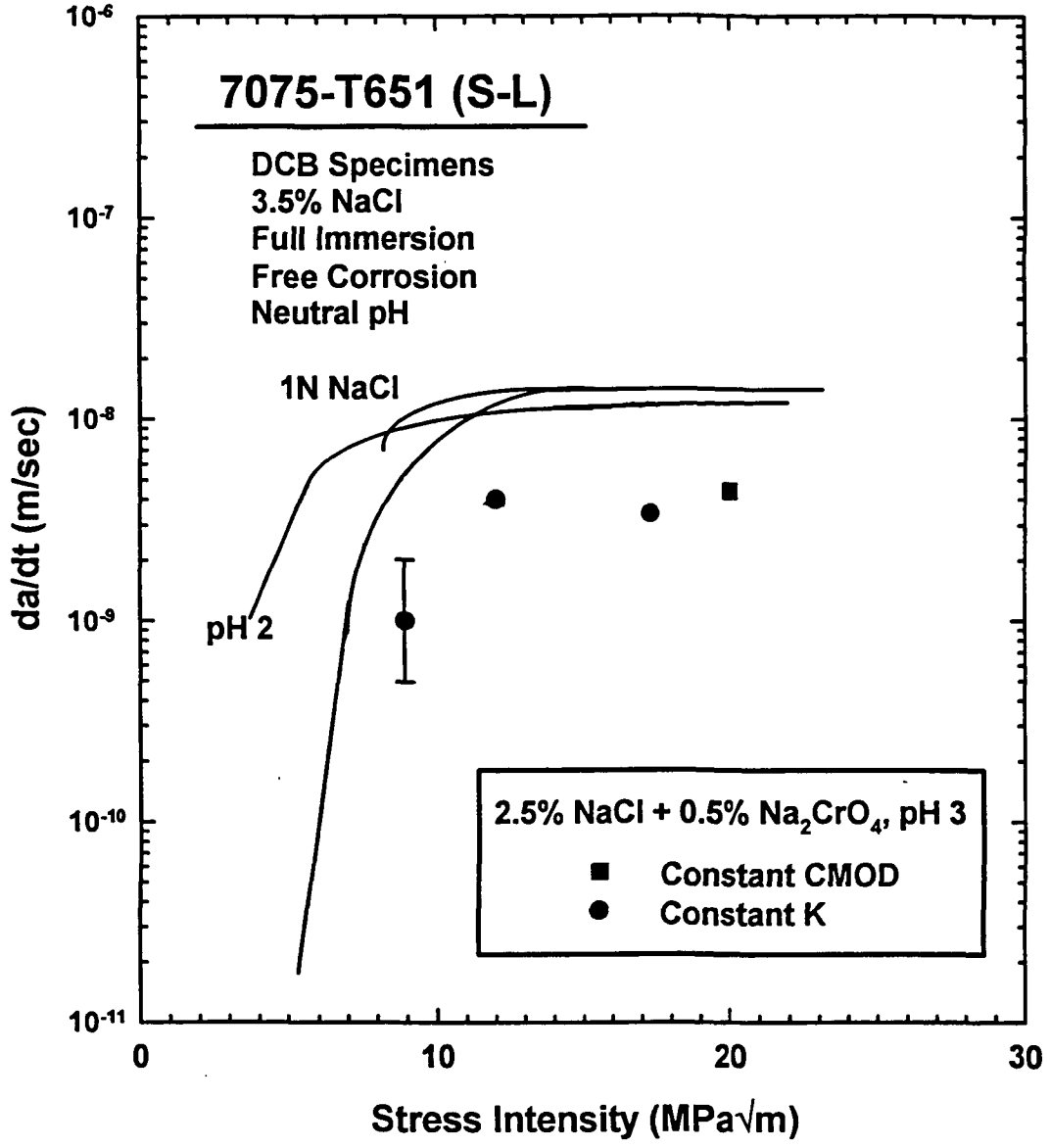

Fig. 3.1. Effect of stress intensity on da/dt showing K-independent da/dt_{II} above K_{ISCC} for 7075-T651(S-L) in chloride [4,5,11-13].

the low values of da/dt_{scc}.

Da/dt_{scc}, plotted as points (● for constant stress intensity and ■ for constant CMOD) in Fig. 3.1., show approximately K-independent cracking. However da/dt_{scc} values range from 2.0 to 4.4 x 10^{-9} m/sec, exhibiting some variability, and are slower than the literature results. The da/dt_{scc} reported by both Colvin and Rechberger are two to five times faster than the da/dt_{scc} in Table 3.1.

Both average da/dt and the continuity of EAC are difficult to determine given the very slow cracking kinetics in this system. Utilization of DCPD to measure crack length is complicated by effects on DCPD measurements including, but not limited to, crack shorting and temperature. Under constant K control, load is computer controlled utilizing DCPD to monitor crack length. If DCPD shows an incorrectly high crack length, load is reduced to maintain constant stress intensity and the actual applied K level is lower than intended. Reduced stress intensity levels near K_{Iscc} may cause K-dependent da/dt, as suggested the constant stress intensity results at a K of 9 MPa$\sqrt{m}$.

Problems with DCPD data acquisition during the constant CMOD experiment caused an instantaneous increase in DCPD equivalent to 1.5 mm of crack growth during the experiment, indicating a burst of crack growth. Under CMOD control an increase in DCPD and crack length should be accompanied by a drop in load or increase in load-line displacement; neither occurred. The increase in DCPD was probably due to an unidentified problem in the DCPD hardware such as a loose potential drop lead. The discontinuity in the crack length versus time data

precluded linear regression analysis. Da/dt_{scc} was determined by dividing visually measured total crack growth (Δa) by the time duration of constant CMOD (Δt). No evidence for discontinuous crack growth was detected in the load versus time results.

Thermal effects obscure DCPD crack length versus time data, hence there is no strong evidence from DCPD to support discontinuous EAC. Crack length versus time data for a constant K of 17.3 MPa$\sqrt{m}$ presented in Fig. 3.2 show the sensitivity of DCPD to fluctuations in ambient temperature that makes differentiation of discontinuous crack growth from thermal effects difficult. Arrows in Fig. 3.2 indicate two to five hour periods of nil or negative crack velocity as recorded by DCPD, probably caused by specimen cooling. Small decreases in DCPD due to reduced environment temperature, coupled with slow crack growth rates (approximately 3×10^{-6} mm/sec), could cause an apparent decrease in DCPD, inhibit data storage which is triggered by increasing DCPD, and reduce the average potential stored when temperature or crack length increase DCPD to a level sufficient to trigger data averaging and storage. In each instance indicated by an arrow, data storage is inhibited for more than three hours and the average potential stored reflects the influence of thermally affected low DCPD values on the average DCPD for the preceding period of crack propagation. Additionally, the arrows are spaced at approximately 24 hour intervals, indicating effects of daily laboratory temperature fluctuations.

Da/dt_{scc} shown in Fig. 3.1 and Table 3.1 provide input for application of the

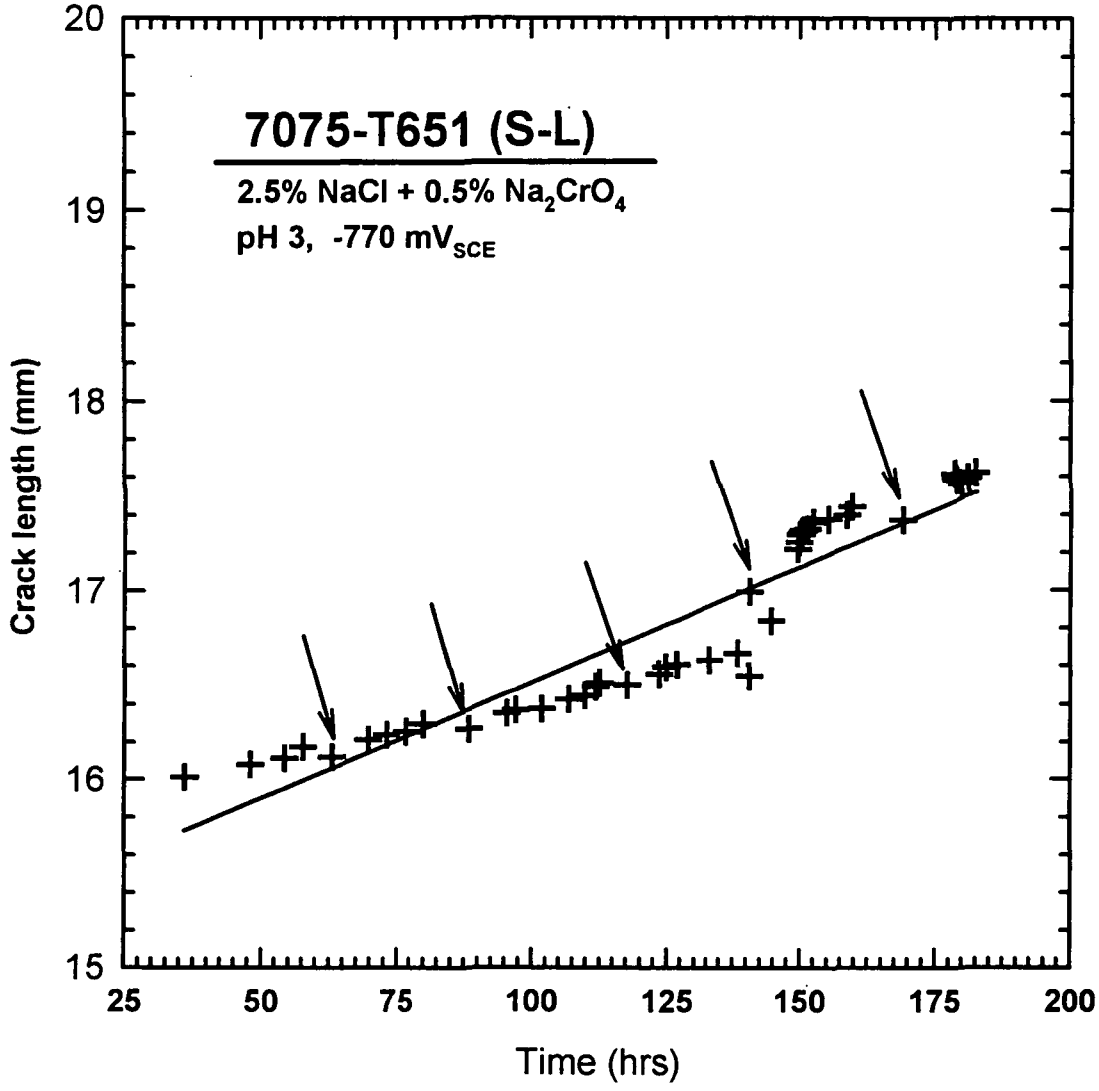

Fig. 3.2. Crack length as a function of time for a constant K of 17.3 MPa√m for 7075-T651(S-L) in aqueous chloride. Arrows indicate where data storage was inhibited for more than 3 hours by thermal effects.

linear superposition model for corrosion fatigue of this heat and orientation of 7075-T651 in this specific chromate inhibited acidified chloride environment. Difficulties in determining da/dt_{scc} are attributed to the very slow cracking kinetics seen for 7075-T651(S-L) in this study.

3.1.2 EAC Under Constant Load Line Displacement Rate

3.1.21 Background

The crack tip strain rate ($d\epsilon_{CT}/dt$) during constant load or displacement measurements of K_{Iscc} and da/dt is low for 7075-T651 in chloride due to low levels of the three factors that control $d\epsilon_{CT}/dt$; crack tip creep deformation, dK/dt, and da/dt. [3,36] Strain rate, and perhaps da/dt, are increased if the precracked specimen is subjected to a monotonically increasing K at a fixed CMOD rate. Rechberger reported that da/dt_{scc} varied by 5-fold (between 4×10^{-9} and 2×10^{-8} m/sec) as dK/dt increased from 7×10^{-6} to 10^{-4} MPa$\sqrt{m}$/sec for 7075-T651 in 3.5 wt pct NaCl, however the results do not indicate that da/dt systematically changes with increasing dK/dt. [15]

High crack tip strain rates may enhance cracking and hence decrease the stress intensity level where crack extension is first detected, K_{TH}. Ford and Silverman reported that K_{TH} decreased with increasing rate of loading for sensitized 304 stainless steel in high purity water at 95°C where K_{TH} was determined from variable loading rate CF experiments. [43] Pao and coworkers indicate the transition where K_{TH} becomes greater than K_{Iscc} for cracking in the rolling plane of

7075-T651. Pao and coworkers report a K_{TH} of 11 MPa$\sqrt{m}$ at a low K rate of 10^{-4} MPa$\sqrt{m}$/sec (CMOD rate of 2 x 10^{-6} mm/sec) for 7075-T651(S-T) in a 3.5% NaCl environment, plotted as ● in Fig. 3.3. [44] Extensive data, reported by Dietzel and Schwalbe, from similar rising-load SCC experiments with 2024-T351 (S-L) in full immersion neutral NaCl are plotted as a solid line in Fig. 3.3. [35] A sharp transition, *from* K_{TH} *equalling* K_{ISCC} *at low loading rates to* K_{TH} *equalling* K_{IC} *at faster* rates, was observed at the applied CMOD rate of 3 x 10^{-7} mm/sec. The scatter band for 2024 moist air K_{IC} is shown in Fig. 3.3; K_{IC} is CMOD rate independent in moist air for 2024.

3.1.22 Crack Growth Results

Limited results of fixed CMOD rate experiments, performed with 7075-T651 (S-L) in moist air and chloride, are plotted with the comparable results for 2024 and 7075 in Fig. 3.3. A single EAC experiment was conducted with 7075-T651(S-L) in chloride at a fixed CMOD rate of 2 x 10^{-5} mm/sec (■). The results in Fig. 3.3, plotted as the K level where crack extension was first easily detected by DCPD (K_{TH}) versus CMOD rate, show that K_{TH} equals K_{IC} (□) for mechanical failure in moist air. Measured values of K_{IC} are equal for the S-L orientation of 7075-T651 at both standard and slow loading rates. Comparison of the chloride results for 7075 with 2024 suggests the transition shown by the dashed line in Fig. 3.3 from K_{ISCC} to K_{IC}, at a CMOD displacement rate of about 10^{-6} mm/sec.

Da/dt, measured during the rising load NaCl experiment represented in Fig.

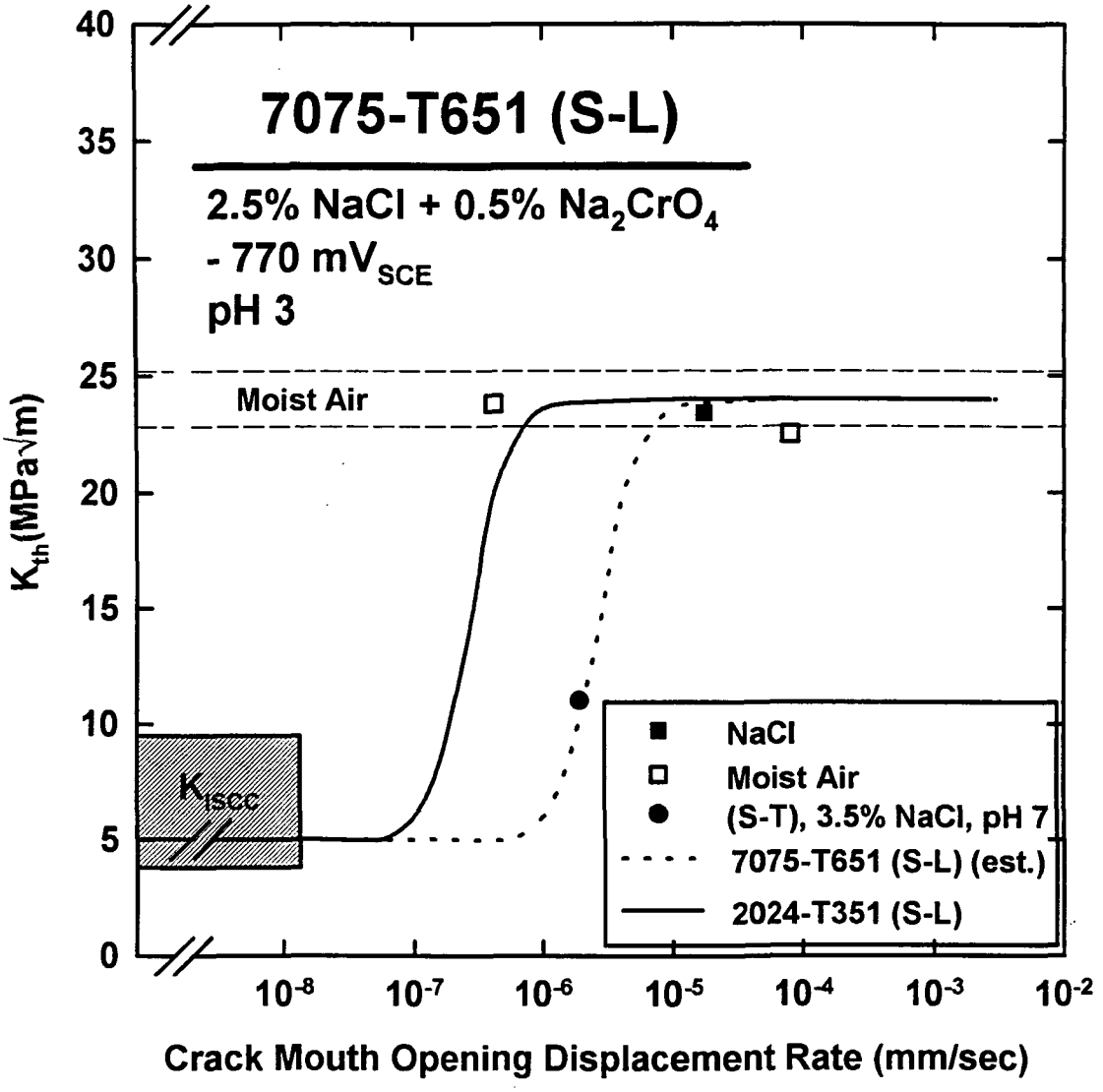

Fig. 3.3. Threshold stress intensity for onset of environmental cracking versus CMOD rate for the S-L orientation of 7075-T651 in moist air and chloride, and 2024-T351 in chloride. [35,44]

3.3, equalled 2 to 6 x 10^{-9} m/sec. Similar-rate rising load experiments in moist air produced an apparent da/dt of 1 to 2 x 10^{-9} m/sec at higher K. Da/dt was measured by fitting a straight line to the corrected crack length (from DCPD) versus time data, starting at the first visually detectable increase in slope before K_{Ic}. This result for benign environment mechanical cracking is probably due to temperature and plasticity enhanced resistivity, and not subcritical crack growth. Accordingly, da/dt from the NaCl rising load experiment is essentially equal to the quasi-static load da/dt_{scc} values presented in Fig. 3.1.

Considering the displacement rate of 2 x 10^{-5} mm/sec, K_{Ic} is achieved in 6.5 hours. If da/dt were enhanced by 5 to 10 times above da/dt_{scc}, then between 0.4 and 0.8 mm of environmental crack growth would be produced. The complex effects of temperature and plasticity on DCPD measurements are small compared to these crack growth increments, and enhanced da/dt should be measurable. The rising load rates represented in Fig. 3.3 (■) did not enhance da/dt prior to mechanical failure. Faster loading rates would produce a similar result and slower rates would produce da/dt equivalent to da/dt_{scc}. [15] Accordingly, no additional rising load rate experiments were conducted.

3.1.3 EAC Under Ripple Load

3.1.31 Background

The superposition of a small amplitude cyclic stress intensity, on a constant or slowly rising K, could destabilize mechanically the crack tip surface to enhance

electrochemical activity and hence increase da/dt above da/dt_{SCC}. While Bayles and coworkers reported that 7075-T651 is susceptible to enhanced chloride cracking under high frequency, low ΔK "ripple" loading, the stress intensity amplitude employed was sufficiently large to produce process zone fatigue damage. [44,45]

3.1.32 Crack Growth Rate Results

Crack length versus time results for a specimen subjected to constant K followed by superimposed small amplitude ΔK ripple loading are presented in Fig. 3.4. The fatigue precracked specimen was held under constant stress intensity of 11 to 13 MPa$\sqrt{m}$ for a period of 120 hours, the crack velocity results for this segment, 3.5 x 10^{-9} m/sec (specimen T6-07) are presented in Table 3.1. The specimen was then fatigued at a ΔK of 11 MPa$\sqrt{m}$ (K_{MAX} = 13 MPa$\sqrt{m}$) to mark the fracture surface for post test visual crack length measurements.

The data plotted in Fig. 3.4 show a negligible difference between the constant stress intensity case and the addition of the low ΔK ripple load. The sinusoidal ripple load, with ΔK of 0.7 MPa$\sqrt{m}$ and K_{MAX} of 13 to 14.5 MPa$\sqrt{m}$ (variation in K_{MAX} was due to post test crack length corrections affecting calculated K values), was applied at a frequency of 5 Hz for 51 hours. For this 5 Hz segment, a least squares line fit to the corrected DCPD crack length versus time data in Fig. 3.4 shows a da/dt of 3.6 x 10^{-9} m/sec. $\Delta a/\Delta t$ is not available because the boundary between the marking fatigue crack and the 5 Hz segment was not

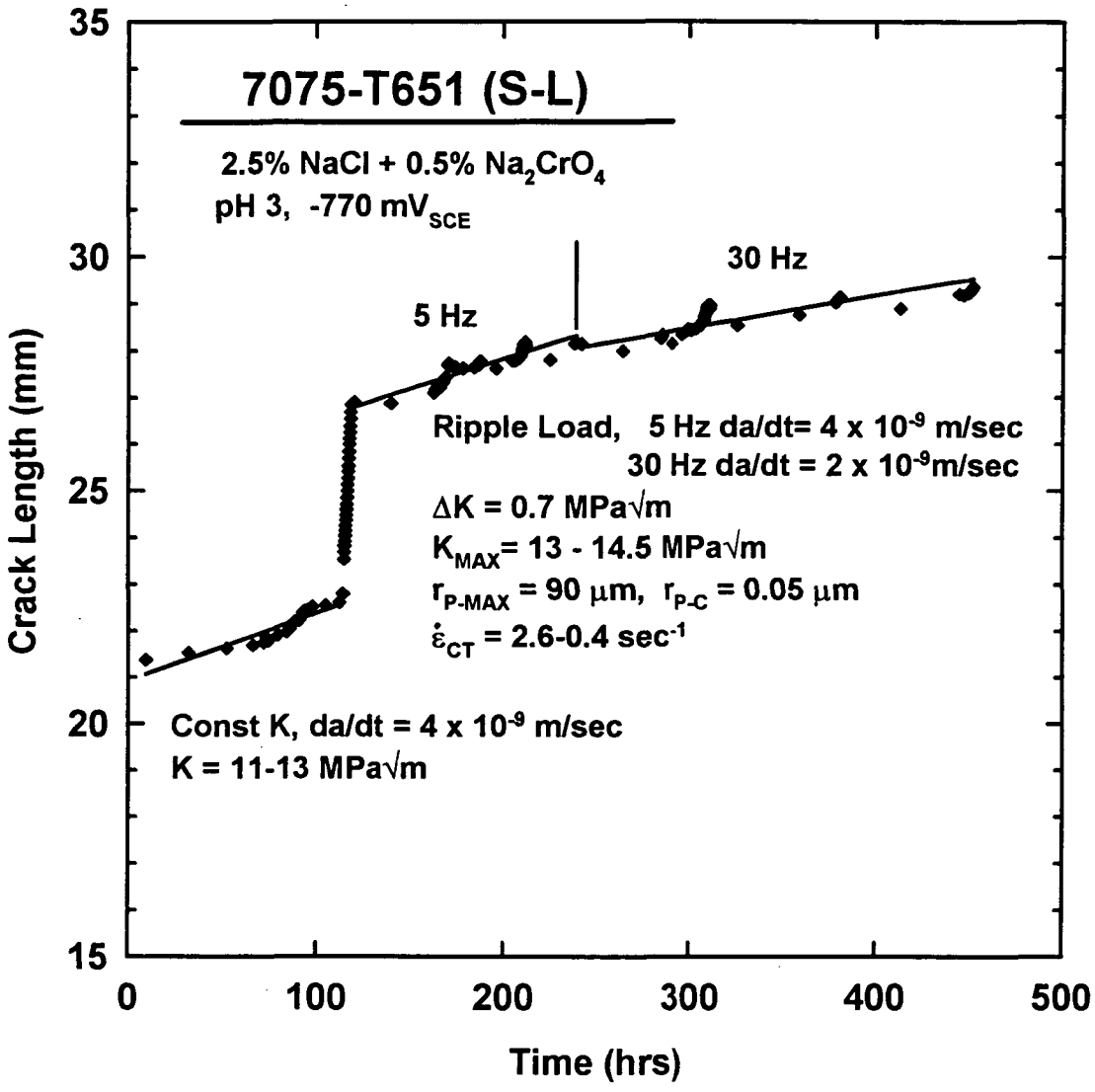

Fig. 3.4. Crack length as a function of time for low amplitude ΔK ripple loading of 7075-T651(S-L) in chloride.

visible. A 30 Hz sinusoidal ripple load was then imposed with the same loading parameters for 282 hours (12 days), producing a line fit da/dt of 1.9 x 10^{-9} m/sec. Measurements using SEM fractographs indicate a Δa of 1.2 mm with $\Delta a/\Delta t$ of 1.2 x 10^{-9} m/sec.

The low ΔK of 0.7 MPa$\sqrt{m}$ may have been sufficient to cause cyclic process zone damage and hence fatigue crack propagation. Results from Pao and coworkers show an apparent ΔK_{TH} of 1 MPa$\sqrt{m}$ with da/dN of 8 x 10^{-10} m/cycle for 7075-T651(S-T) in 3.5 wt pct NaCl at an R of 0.9 and frequency of 5 Hz. [44] The 5 Hz ripple load da/dt is equivalent to a da/dN of 8 x 10^{-10} m/cycle while the 30 Hz da/dN is 7 x 10^{-11} m/cycle, both at an R of 0.95. Crack propagation rates, da/dt and da/dN, are within the ranges for either subcritical crack propagation due to the high sustained K_{MAX} or threshold corrosion fatigue crack propagation.

SEM fractography may provide a means to determine the crack tip damage mechanisms for this case of ripple loading.

3.2 Environment Enhanced Fatigue Crack Growth

3.2.1 Effect of Environment on da/dN versus ΔK

3.2.11 Background

The limited data on the effect of ΔK on EFCP da/dN for crack propagation parallel to the rolling plane of 7075-T651 indicates a significant enhancement of da/dN due to chloride environments. [11,46] Santner and Kumar reported an order of magnitude increase in da/dN in 3.5% NaCl at 0.2 Hz over da/dN in

nitrogen gas for 7075-T651 in both the S-T and T-L orientations at an R of 0.1. [46] At 20 Hz and R of 0.1, Baldantoni observed an enhancement of da/dN of five to thirty-fold for 3.5% NaCl over FCP in argon gas, with the greater environmental enhancement at low ΔK, decreasing to five-fold at high ΔK. Green and Knott reported EFCP da/dN for 7475-T651, a low impurity version of 7075, in an environment identical to the present study, showing a five to ten-fold increase in chloride da/dN at a frequency of 0.5 Hz over 4 Hz moist air da/dN.

Notably, the L-T orientation of 7075-T651 shows an identical enhancement of da/dN in NaCl. Dill et al. reported an increase in chloride da/dN of four times over dry air (< 10% relative humidity) values for the L-T orientation at a zero stress ratio and frequency of 10 Hz. [29] A larger ten-fold increase in EFCP da/dN was observed for the L-T orientation by Selines and Pelloux; specimens were tested at 10 Hz,a slightly higher R of 0.016, and in an environment of 3.5 % NaCl. [27] The literature results show chloride environments enhance fatigue crack propagation up to approximately ten-fold above less aggressive gas environments for 7075-T651.

3.2.12 Fatigue Crack Growth Rate Results

ΔK decreasing experiments were performed to obtain chloride and moist air fatigue crack propagation rates for 7075-T651 in the S-L orientation at 5 Hz and R of 0.1. The results, plotted as da/dN versus ΔK, are presented in Fig. 3.5. For comparison, fatigue results for 7075-T651 in the L-T orientation in inert helium (ΔK

> 10 MPa√m) and dynamic vacuum (ΔK < 10 MPa√m) are represented by the dashed line. [47] Figure 3.5 shows that EFCP da/dN is enhanced five to ten-fold over rates in moist air and over an order of magnitude faster compared to cracking in helium.

The da/dN versus ΔK behavior in chloride at 5 Hz, shown in Fig. 3.5, is identical to that reported for 7475-T651(S-L) at 0.5 Hz in the same environment for the range of ΔK levels examined. [9] The data for 7475-T651 extend to higher ΔK due to the ΔK increasing method used and the slightly higher K_{IC} of the cleaner alloy. The moist air results for the peak aged 7075 and 7475 are identical as well, showing a transition in slope of da/dN versus ΔK between 6 and 8 MPa√m. A transition in slope is often associated with a change in fracture mode, however, no SEM fractography was performed to confirm this observation. No slope transition is indicated for the chloride data in Fig. 3.5.

A simple power law relation was fit by linear regression methods to the chloride da/dN using an equation of form:

$$\frac{da}{dN} = C\Delta K^n \qquad (3.1)$$

with C equal to 3.03×10^{-6} and n of 2.44 (da/dN as mm/cycle and ΔK as MPa√m). The resulting fit of this equation is plotted as a solid line through the chloride data in Fig. 3.5. Equation 3.1 is applied in later data analyses to adjust EFCP da/dN at variable ΔK so that da/dN results may be compared at a single constant ΔK.

To predict plasticity-induced crack closure effects, in a later section, the

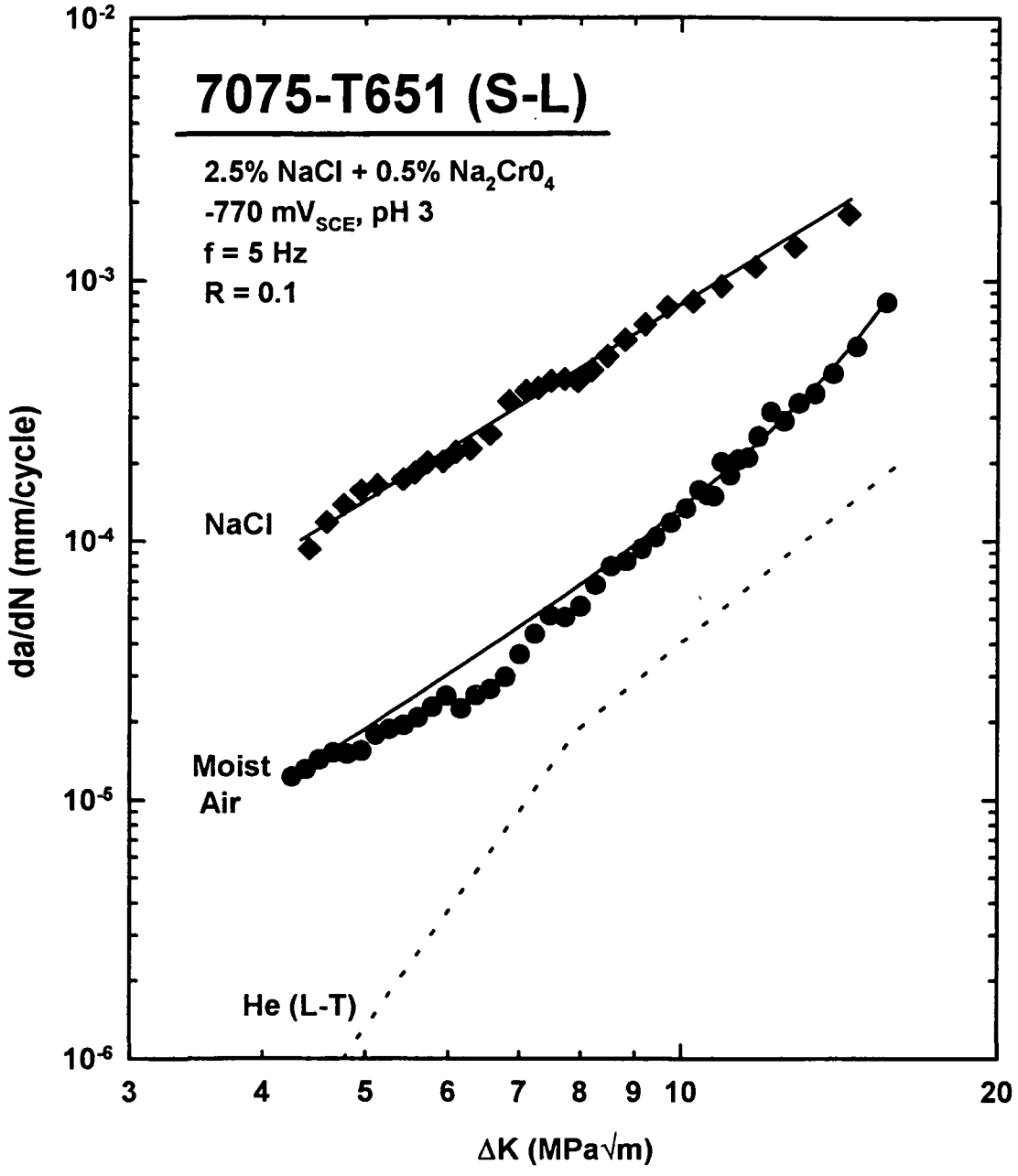

Fig. 3.5. Effect of ΔK on da/dN for 7075-T651(S-L) in chloride, moist air, and inert environments. [47]

Forman equation was fit to the moist air ΔK-decreasing data. [1] The Forman equation, given by:

$$\frac{da}{dN} = \frac{C\Delta K^n (1-f)^n \left(1-\frac{\Delta K_{th}}{\Delta K}\right)^p}{(1-R)^n \left(1-\frac{\Delta K}{(1-R)K_{IC}}\right)^q} \qquad \textbf{(3.2)}$$

relates da/dN to ΔK, the crack closure function (f), ΔK_{th}, K_{IC}, R, and empirical constants (C, p, q, and n). A ΔK_{TH} of 0.509 MPa√m and f of 0.3249, both functions of stress ratio, were calculated for an R of 0.1. The constants determined using an interpolative model for moist air at an R of 0.1 were: $C = 8.428 \times 10^{-7}$ and n = 2.192 (da/dN as mm/cycle and ΔK as MPa√m) [1] for fixed p of 0.5 and q of 1. Initially p and q were fit using the capability of the interpolative model to determine C, n, p, and q. The values for the constants ($C = 5.148 \times 10^{-6}$, n = 5.773, p = -21.56, and q = -0.2167), despite a better fit to the data, could not be utilized to predict the effect of high stress ratio on da/dN versus ΔK since predicted da/dN (Eq. 3.2) was unreasonably large for ΔK levels over 9 MPa√m and for R above 0.3. Equation 3.2, using a p of 0.5 and q of 1, produced a more accurate prediction of increase in EFCP da/dN at a ΔK level of 9 MPa√m from an R of 0.1 to an R of 0.5. The fit, using p of 0.5 and q of 1, is plotted as a solid line through the moist air data in Fig. 3.5. The resulting line gives a relatively good fit to the data above a ΔK of 8 MPa√m and allows prediction of the effect of a stress ratio of 0.5 on da/dN at ΔK levels as high as 10 MPa√m.

3.2.2 Effect of Sinusoidal Frequency on EFCP da/dN

3.2.21 Background

The wide range of frequency dependencies reported for 7000 series aluminum alloys was presented in Fig. 1.2 and summarized in Section 1.2.2. Rechberger's data for 7075-T651 (S-L) in chloride indicate a weak time-cycle dependence above 0.001 Hz for 7075-T651(S-L) in chloride, however there are limited data for frequencies greater than 0.02 Hz. Da/dN for 7475 and 7017 at ΔK of 15 MPa$\sqrt{m}$ and frequencies greater than 0.1 Hz indicate a strong time-cycle dependence, $f^{-0.5}$. It is unclear why Rechberger's data do not show this rate limited behavior and instead indicate a weaker $f^{-0.1}$ dependence.

3.2.22 EFCP Results

DCPD and compliance determined crack length versus loading cycle data for variable frequency segments of constant ΔK sinusoidal loading are presented in Fig. 3.6. Frequency was changed after an increment of crack growth at fixed ΔK for a single specimen. The average applied ΔK for each experiment is noted beside the corresponding data in Fig. 3.6; unloading compliance results are distinguished by the applied ΔK levels of 9.1 and 15.1 MPa$\sqrt{m}$. The remaining two ΔK levels are based on DCPD measurements; four separate specimens are represented in Fig. 3.6. The compliance experiment at a ΔK of 9.1 MPa$\sqrt{m}$ was performed in a neutral, uninhibited 2.5 wt pct NaCl solution. This figure shows the utility in applying the constant ΔK method in combination with DCPD or unloading

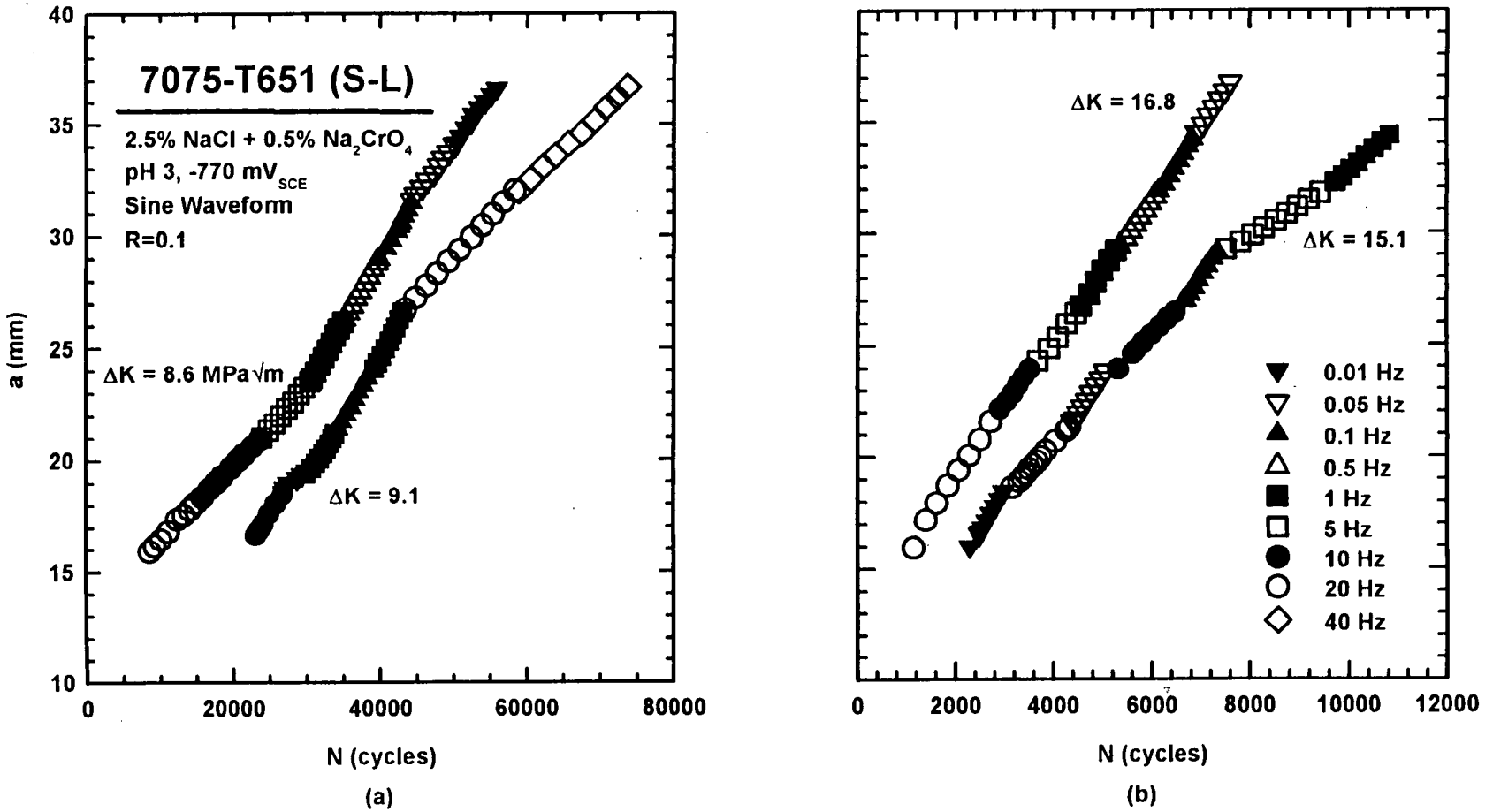

Fig. 3.6 Crack length versus loading cycles for variable frequency constant ΔK and R loading of 7075-T651(S-L) in NaCl.

compliance to distinguish small changes in da/dN due to changing loading frequency.

Trends in fatigue crack propagation rate as a function of loading frequency are observed by plotting da/dN versus frequency at a constant ΔK. In Fig. 3.7 da/dN results obtained by DCPD (▲ for ΔK of 8.5 MPa$\sqrt{m}$ and ▼ for 16.7 MPa$\sqrt{m}$), and da/dN from the compliance based experiments (■ for 15.1 MPa$\sqrt{m}$ and ● for 9.1 MPa$\sqrt{m}$), are plotted versus loading frequency. For each experiment, a parallel Paris law relationship given by Eq. 3.1 was used to adjust da/dN to account for small differences in applied ΔK. FCP rates for this alloy in moist air and inert environments are plotted in Fig. 3.7 to indicate the magnitude of the NaCl effect on da/dN.

No effect of chromate inhibitor on EFCP da/dN is seen in Fig. 3.7. Da/dN for both chromate inhibited acidified and neutral uninhibited solutions are identical and show a mild time-cycle frequency dependence when adjusted for comparison at a single ΔK level of 9 MPa$\sqrt{m}$.

EFCP rate decreases mildly with increasing frequency for both ΔK levels, showing a weak frequency dependence; slopes of the line fit including the DCPD and compliance da/dN are -0.060 ($\pm$0.014) for ΔK of 15 MPa$\sqrt{m}$ and -0.025 ($\pm$0.026) for ΔK of 9 MPa$\sqrt{m}$. These slopes are nearly statistically equal based on the 95% confidence interval estimates shown in parentheses. The trend in frequency dependency shown in Fig. 3.7 for ΔK of 15 MPa$\sqrt{m}$ is consistent with the literature findings for 7075-T6 in Fig. 1.2, but is in contrast to the $f^{-0.5}$ relationship

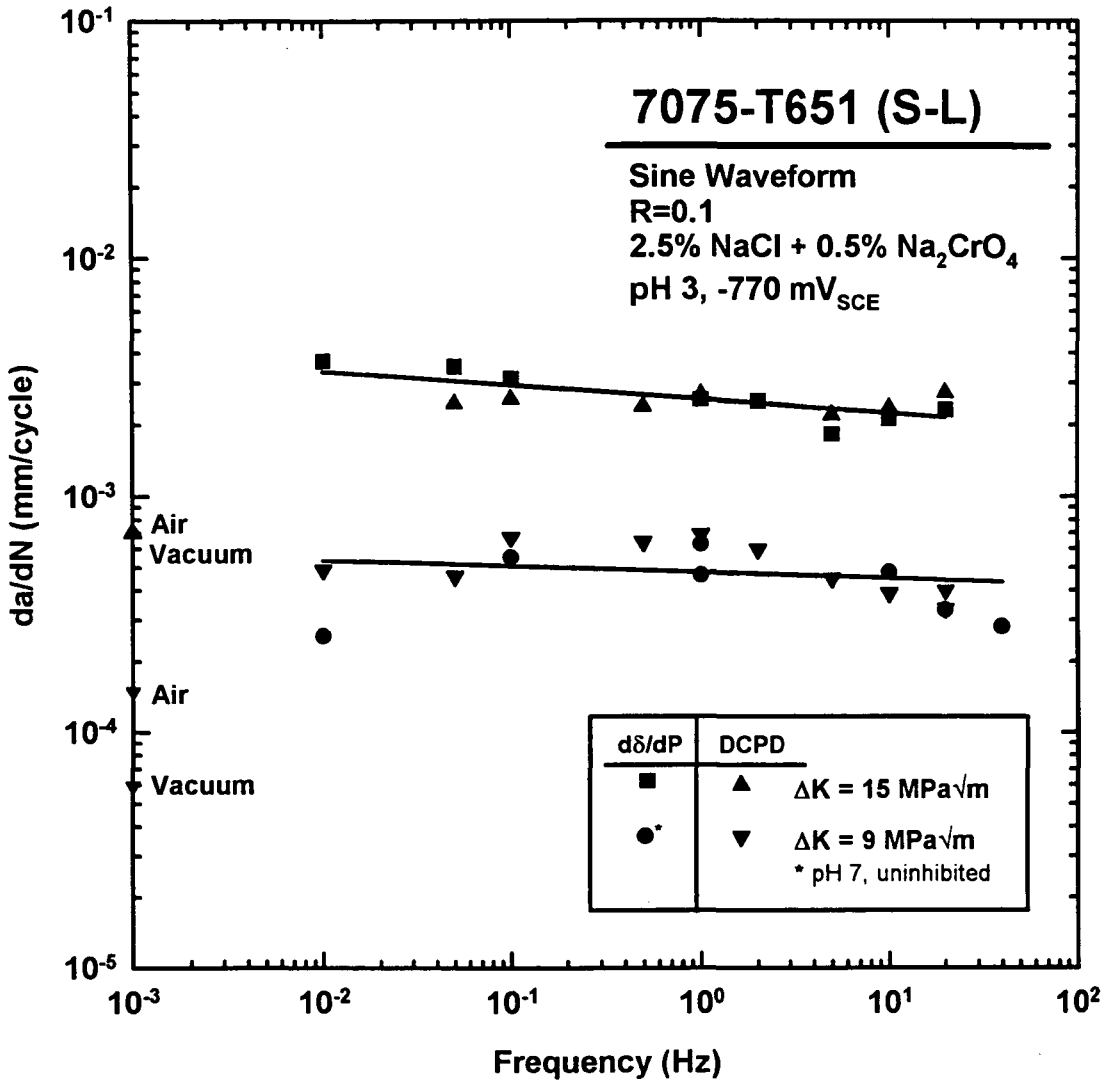

Fig. 3.7. Effect of frequency on EFCP da/dN for constant ΔK loading for 7075-T651(S-L) in chloride.

reported for 7017 and 7475. [9,10] More complex relationships between da/dN and f are plotted and considered in the Discussion.

3.2.23 Fatigue Crack Closure

Time-based crack closure could affect measured EFCP da/dN by accumulation of corrosion debris at the crack tip which could wedge the crack open, increase the minimum stress intensity (K_{MIN}), and decrease ΔK. For example, the weaker frequency dependence shown by the constant ΔK DCPD data at 15 MPa$\sqrt{m}$ (compared to compliance) may be caused by time-based crack closure effects amplified by the chosen sequence of waveform frequency indicated in Fig. 3.6. For the DCPD experiments, frequency was decreased while specimen immersion time in the aqueous environment increased. Time-dependent crack closure could increase the minimum K in the load cycle where crack surface contact occurs, $K_{CLOSURE}$, above K_{MIN}. $K_{CLOSURE}$ is defined as the stress intensity at a 2% deviation in unloading compliance and ΔK_{EFF} is the difference between K_{MAX} and $K_{CLOSURE}$. If ΔK_{EFF} is reduced due to increased specimen immersion time, then da/dN may be reduced for later frequency segments at the low frequencies, in the case of the DCPD data. That is, enhanced intrinsic da/dN at lower frequencies may be reduced by decreasing ΔK attributed to time-dependent corrosion debris accumulation and enhanced crack closure. The compliance-based da/dN followed a sequence of loading frequencies for 15.1 MPa$\sqrt{m}$ (0.01 Hz, 20 Hz, 0.05 Hz, 10 Hz, 0.1 Hz, and 1 Hz) chosen to minimize this potential complicating effect. While

a slightly stronger frequency dependency, Fig. 3.7 shows that da/dN for both frequency sequences are in good agreement, especially at frequencies above 0.5 Hz. The da/dN at a ΔK of 9 MPa$\sqrt{m}$ followed an identical sequence as the compliance-based da/dN for 15.1 MPa$\sqrt{m}$.

Unloading compliance measurements were used to estimate crack closure and to examine the effect of closure on the frequency dependence of da/dN at a constant ΔK of 15 MPa$\sqrt{m}$. ΔK, ΔK_{EFF}, and $K_{CLOSURE}$ are presented in Fig. 3.8a versus specimen immersion time and Fig. 3.8b versus loading cycles for the high ΔK (15 MPa$\sqrt{m}$) experiment in acidified inhibited chloride. $K_{CLOSURE}$ increases with specimen immersion time from 2.7 MPa$\sqrt{m}$ to 5.5 MPa$\sqrt{m}$ and is above the K_{MIN} of 1.5 MPa$\sqrt{m}$, suggesting a role of crack closure due to corrosion product accumulation. Accordingly, ΔK_{EFF} decreases with time.

If intrinsic effects of stress ratio on FCP above R of 0.5 and at a ΔK level above 9 MPa$\sqrt{m}$ are assumed negligible for moist air, and crack closure is attributed solely to plasticity in the crack wake, then ΔK is equivalent to ΔK_{EFF} and $K_{CLOSURE}$ is less than K_{MIN}. By this view, equivalent da/dN at a R of 0.1 and 0.5 have identical ΔK_{EFF} with the difference in ΔK levels due to plasticity induced crack closure. Accordingly, $K_{CLOSURE}$ may be estimated from this difference for R of 0.1. $K_{CLOSURE}$ of 5.3 MPa$\sqrt{m}$ is estimated for EFCP at a ΔK of 15 MPa$\sqrt{m}$, R of 0.1, and da/dN of 3×10^{-3}mm/cycle by determining ΔK for an R of 0.5 (ΔK_{EFF}) to obtain an equivalent da/dN (Eq. 3.2) in moist air. Since estimated $K_{CLOSURE}$ due to plasticity is nearly equal to $K_{CLOSURE}$ shown in Fig. 3.8 for chloride measured by the global

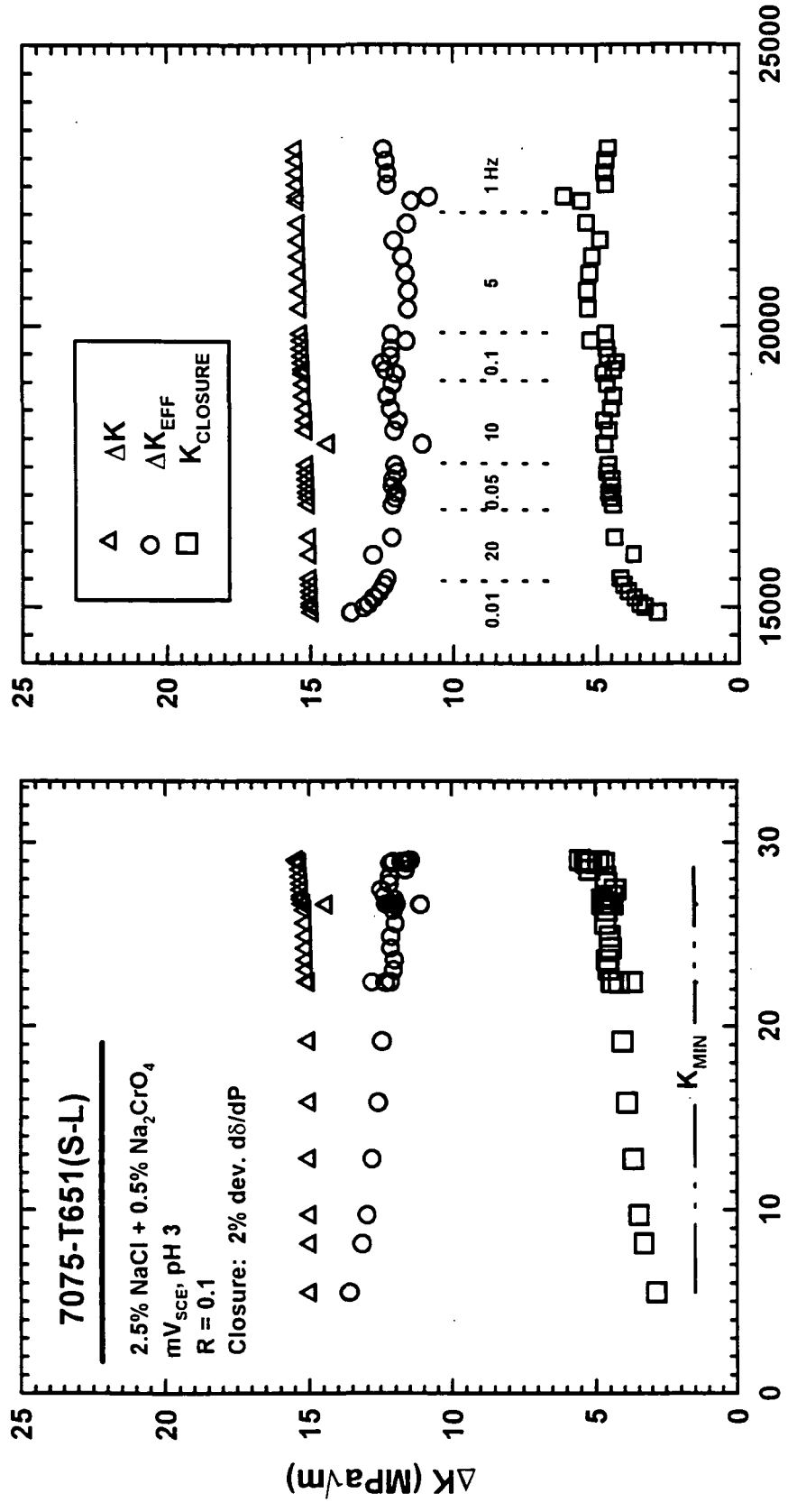

Fig. 3.8. Effect of (a) specimen immersion time and (b) frequency on closure stress intensities for the S-L orientation of 7075-T651 in chloride.

compliance method, plasticity induced closure cannot be eliminated as a possible cause for the closure seen in Fig. 3.8. Plasticity may explain $K_{CLOSURE}$ at short environmental exposure times, but not the time dependence of $K_{CLOSURE}$.

Figure 3.8b shows that $K_{CLOSURE}$ is frequency independent and approximately 5 MPa$\sqrt{m}$ for frequencies greater than 0.01 Hz. In contrast to the higher frequency segments, the 0.01 Hz frequency segment $K_{CLOSURE}$ increases by 1.5 MPa$\sqrt{m}$ due to the 14 hours necessary for 2 mm of crack propagation. The shorter time required to complete the remaining frequency segments minimized the effect of mildly increasing $K_{CLOSURE}$ with specimen immersion time seen in Fig. 3.8a. The influence of changes in $K_{CLOSURE}$ on frequency dependent da/dN at frequencies greater than 0.01 Hz and a ΔK of 15 MPa$\sqrt{m}$ is negligible and the frequency dependence indicated in Fig. 3.7 for ΔK of 15 MPa$\sqrt{m}$ is reasonably intrinsic.

Despite apparent decreasing ΔK_{EFF}, da/dN did not change with specimen immersion time for the 0.01 Hz frequency segments, suggesting that the global compliance measurement of $K_{CLOSURE}$ is not a meaningful estimate for ΔK of 15 MPa$\sqrt{m}$. Closure may reduce da/dN at ΔK of 15 MPa$\sqrt{m}$ and for longer specimen immersion times, however, corrosion product induced closure had negligible effects on the da/dN-frequency dependence at a ΔK of 15 MPa$\sqrt{m}$ and for the specimen immersion times in this study.

Da/dN for ΔK of 9 MPa$\sqrt{m}$ in 2.5 wt pct NaCl is identical to da/dN for chromate inhibited acidified 2.5 wt pct NaCl for frequencies above 0.01 Hz. Differences in the chosen frequency sequence (see Fig. 3.6) do not appear to have

affected the frequency dependence of da/dN. Identical da/dN indicate that the five times higher passive current density in the uninhibited environment [15] causes no resolvable increase in corrosion product induced crack closure.

Figure 3.7 shows that a more aggressive uninhibited environment does not appear to affect the frequency dependence of da/dN at an R of 0.1. $K_{CLOSURE}$ was measured at a lower ΔK level of 9 MPa$\sqrt{m}$ in neutral uninhibited chloride to determine the effect of time-dependent closure on $K_{CLOSURE}$ and ΔK_{EFF}. An environmental cell leak precluded calculation of specimen immersion time and may have affected the crack closure estimates for 7075-T651 in neutral uninhibited NaCl, presented in Table 3.2. Average values for applied ΔK, ΔK_{EFF}, and $K_{CLOSURE}$ are given in Table 3.2, showing $K_{CLOSURE}$ varying from 3.3 to 5 MPa$\sqrt{m}$, as measured at a 2% deviation in unloading compliance, without a frequency or segment time dependence. The results in Table 3.2 and Fig. 3.8 indicate that $K_{CLOSURE}$ does not depend on frequency. It is interesting to note that $K_{CLOSURE}$ equals 4 $\pm$ 1 MPa$\sqrt{m}$ for ΔK levels of 9 and 15 MPa$\sqrt{m}$, suggesting a non-ΔK-dependent crack closure mechanism such as corrosion debris wedging the crack tip open.

While time dependent crack closure effects on ΔK and da/dN may be mildly immersion time-dependent, results presented in Figs. 3.6 to 3.8 and Table 3.2 show that corrosion product induced crack closure is difficult to quantify. Comparison of compliance estimations with DCPD results indicate a negligible effect of closure on the frequency dependence of da/dN for ΔK of 9 and 15 MPa$\sqrt{m}$.

Table 3.2 Crack closure measurements and da/dN for constant ΔK EFCP of 7075-T651(S-L) in uninhibited NaCl

Sequence #	Time (sec) t_{START}-t_{FINISH}	Frequency (Hz)	Average ΔK^* (MPa√m)	Average ΔK_{EFF} (MPa√m)	Average $K_{CLOSURE}$ (MPa√m)
2	256500	0.01	9.0	4.9	5.0
4	46000	0.1	9.1	6.3	3.7
3	4116	1	9.0	4.6	5.3
5	4104	1	9.2	6.8	3.3
1	480	10	9.0	5.1	4.8
6	742	20	9.3	6.5	3.7
7	407	40	9.4	5.3	5.0

*R=0.1

3.2.3 Effect of Hold Time at K_{MAX} on EFCP da/dN

3.2.31 Background

The previous success in determining da/dt versus K behavior, based on trapezoidal loading for SCC susceptible high strength steels and to a limited extent 7075-T651 (L-T), is summarized in Section 1.2.2. The S-L orientation of 7075-T651 has both a lower threshold for static load cracking, K_{ISCC}, and a higher da/dt_{SCC} than the L-T orientation [17] and may prove a better candidate for enhanced da/dt due to trapezoidal fatigue loading conditions. Enhanced da/dt measured during hold time at K_{MAX} may provide a more useful input of da/dt for prediction of EFCP da/dN via the linear superposition model (Eq. 1.2).

3.2.32 EFCP Results

Trapezoidal loading results for several hold times at K_{MAX} are presented in

Fig. 3.9 as crack length versus loading cycles. The corresponding plot symbol, hold time, and controlled-constant ΔK are compiled in Table 3.3 with the da/dN from a least squares fit of crack length versus time. Results from Dill and Saff for 7075-T651 (L-T) in 3.5 wt pct NaCl, included in Table 3.3, show similar da/dN for comparable hold times and ΔK levels.

Table 3.3 Effect of hold time at K_{MAX} on EFCP da/dN for 7075-T651(S-L) in chloride.

Plot Symbol	Hold Time (sec)	ΔK^* (MPa$\sqrt{m}$)	da/dN (mm/cycle)
○	0.1	10.4	0.78×10^{-3}
●	50	10.4	0.68×10^{-3}
△	0.1	14.7	1.60×10^{-3}
▲	50	13.4	1.17×10^{-3}
□	0.1	11.9	0.97×10^{-3}
■	5	11.9	1.10×10^{-3}
◇	25	8.7	0.65×10^{-3}
**	0.1	10.4	0.56×10^{-3}
**	10	10.4	0.56×10^{-3}

** Results for 7075-T651(L-T) in 3.5 wt pct NaCl. [29] *R = 0.1

Measured da/dN, adjusted using Eq. 3.1 for comparison at a single ΔK, are plotted vs hold-time at K_{MAX} in Fig. 3.10. Da/dN is essentially constant for relatively rapid rise/fall (t_{RISE} and t_{FALL} each equal to 0.025 sec) trapezoidal waveforms with hold times of 0.1, 5, and 50 seconds. Although mild corrosion-induced closure may account for the small fall in da/dN with increasing τ_H at the higher ΔK, this is more likely due to experimental error and the limited data. Time dependent crack

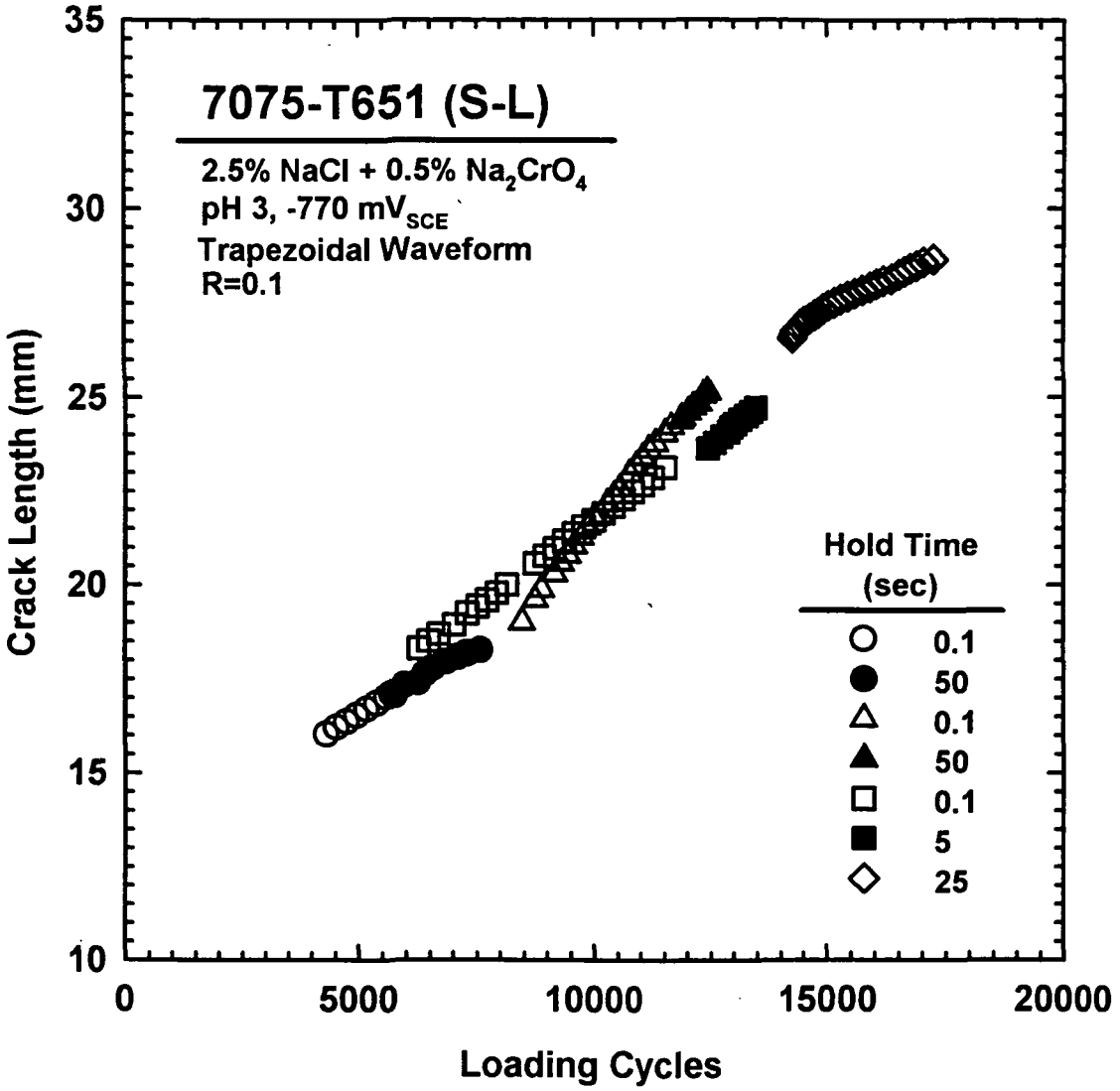

Fig. 3.9. Crack length versus loading cycles for trapezoidal loading of 7075-T651(S-L) in chloride.

closure effects on da/dN versus τ_H are minimized by alternating long and short hold time test segments. In contrast da/dN increases mildly with increasing τ_H for the lower ΔK case ($da/dN \propto \tau_H^m$, where $m = 0.014 \pm 0.030$), consistent with the results for EFCP under sinusoidal loading (Fig. 3.7). For 7075-T6 in the S-L orientation, results from corrosion fatigue experiments at two constant stress intensities indicate no strong hold-time-dependence for the loading and unloading rates and times tested.

3.2.4 Effect of Rise Time to K_{MAX} on EFCP da/dN

3.2.41 Background

The dependence of EFCP da/dN on fatigue cycle rise time to K_{MAX} for constant ΔK and R is summarized in Section 1.2.2 for high strength steels and 7075-T651. Da/dN is proportional to t_R^m where m is nominally 0.1 for 7075-T651 in the L-T orientation. [27,29,33] Since this time dependence is weak, the constant ΔK method is well-suited to resolve the effect of load rise time for 7075-T651 in the S-L orientation.

3.2.42 EFCP Results

Constant ΔK and R EFCP experiments were conducted to examine the effect of t_R on da/dN. Results in Fig. 3.11 show a vs N data for constant ΔK segments and two specimens of 7075-T651 (S-L) in NaCl. Rise time is varied in the slow/fast to fast/slow sequence, while maintaining total cycle period as a constant (see +

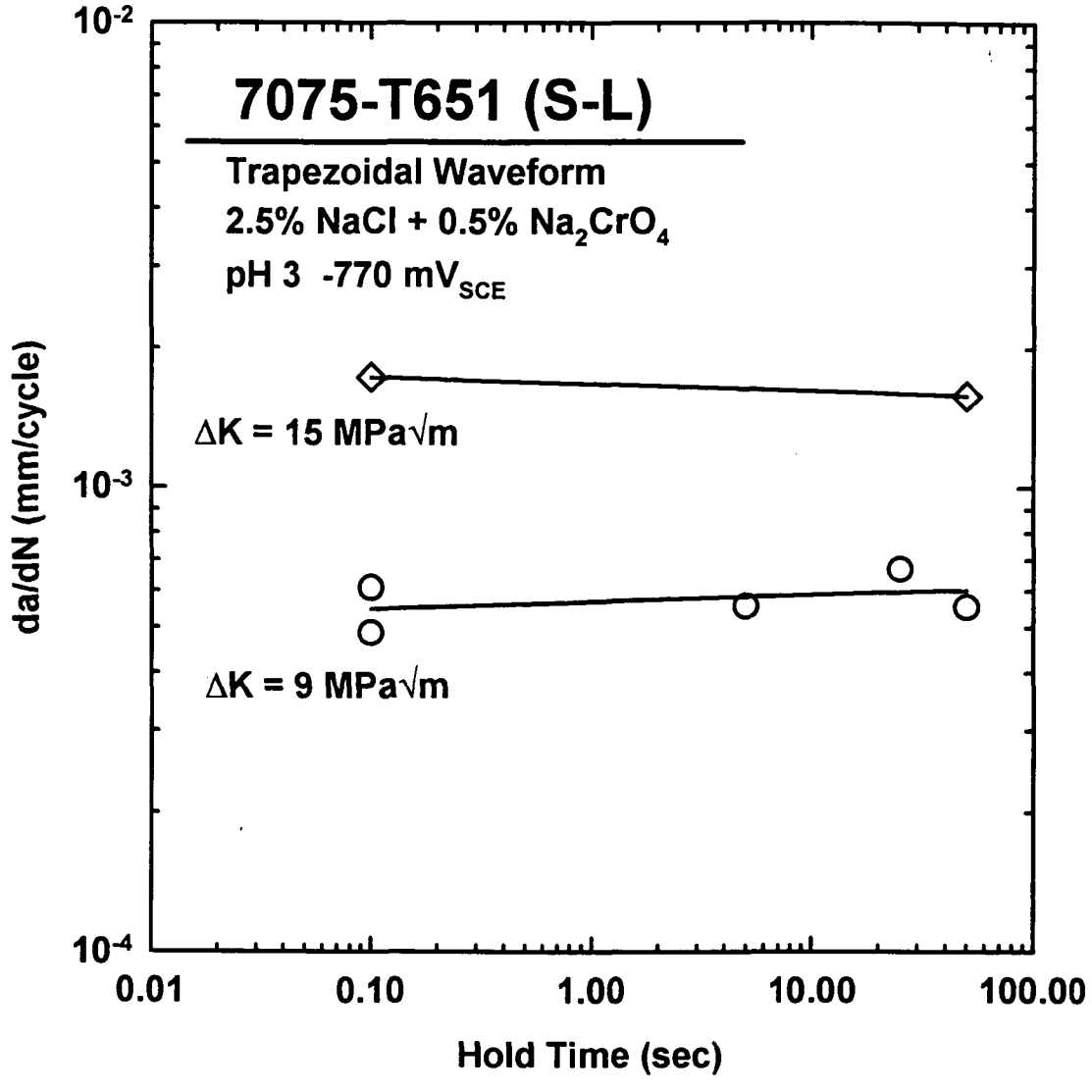

Fig. 3.10. Fatigue crack growth rate versus hold time at K_{MAX} for 7075-T651(S-L) in chloride.

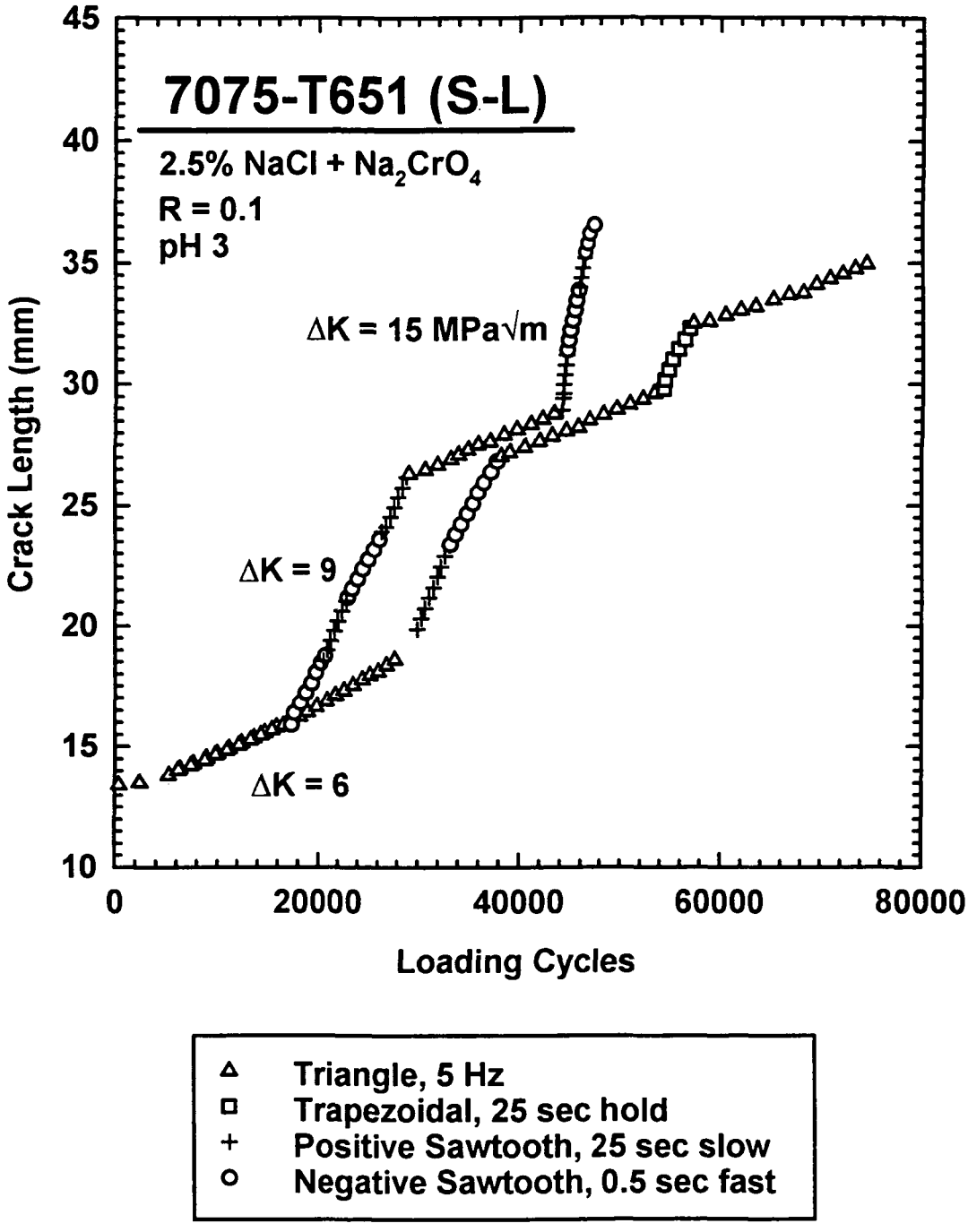

Fig. 3.11. Crack length versus loading cycle for asymmetric loading waveforms for 7075-T651(S-L) in chloride.

to ○), and a subtle decrease is noted in the crack growth rate. Triangle waveforms at a ΔK of 6 were included to mark the fracture surface for post-test crack length determinations and a single trapezoidal loading segment was performed at a ΔK of 15 MPa√m which was included with the results presented in the previous section.

EFCP results are plotted in Fig. 3.12 in terms of da/dN vs the rise time to K_{MAX} for constant ΔK segments including triangular, asymmetric triangular with either a slow/fast or a fast/slow rise/fall sequence (Fig. 3.11), trapezoidal (Fig. 3.9), and sinusoidal (Fig. 3.6) K(t) loading functions. Small differences in applied ΔK were accounted for by the wide-range EFCP rate relationship (see Fig. 3.5). Least squares analyses applied to the data from this study at an R of 0.1 show that da/dN is proportional to t_R^m, where m is 0.074 (±0.018) for ΔK of 9 MPa√m and 0.080 (±0.021) for ΔK of 15 MPa√m. The results in Fig. 3.12 are in excellent agreement with data (●) for peak-aged 7075 (L-T) orientation; da/dN is proportional to t_R raised to the 0.10 power. [27] Austen and Walker reported a similar rise time dependence of m = 0.1 for a low alloy pressure vessel steel (A533B-1) in 90°C 3 wt pct NaCl and 90°C distilled water. [48] Ouchi et al. showed a similar dependence of da/dN on t_R, with m equalling 0.3 for a moderate tensile strength alloy steel in NaCl. [31]

3.2.43 Fatigue Crack Closure

The effect of fatigue crack closure on the rise time dependency of da/dN,

specific to corrosion debris produced in the chromate inhibited chloride environment, was investigated by conducting a constant ΔK triangle waveform experiment at a load ratio of 0.5. The resulting EFCP rates are plotted (♦) in Fig. 3.12. Da/dN is increased at each rise time by 30% in response to the increase in R from 0.1 to 0.5. Calculations using a Forman relation, fit to the moist air da/dN vs ΔK data in Fig. 3.5 to account for plasticity induced closure, predict a 200% increase in da/dN from R of 0.1 to 0.5 at ΔK of 9 MPa√m. As with previous results, the data in Fig. 3.12 do not allow a differentiation between corrosion product debris, plasticity induced crack closure and an intrinsic effect of R on EFCP da/dN. Since a substantial amount of plasticity induced closure is predicted, the result in Fig. 3.12 can not be interpreted based on an intrinsic effect of stress ratio on EFCP. The R of 0.5 results show the same rise time-dependence as the findings for the lower stress ratio. In all cases examined at the lower R, da/dN values were essentially equal when determined at constant ΔK, but at varying crack length and hence varying total solution exposure time during the experimental sequence (e.g., Fig. 3.11). Crack closure has not affected the rise time dependence of da/dN.

3.2.5 Effect of Orientation on EFCP da/dN

Comparisons between literature data and the new results in Figs. 3.5, 3.7, 3.10, and 3.12 show that crack orientation has no resolvable effect on EFCP in 7075-T651 in aqueous NaCl for the frequency regime above 0.001 Hz. This is in

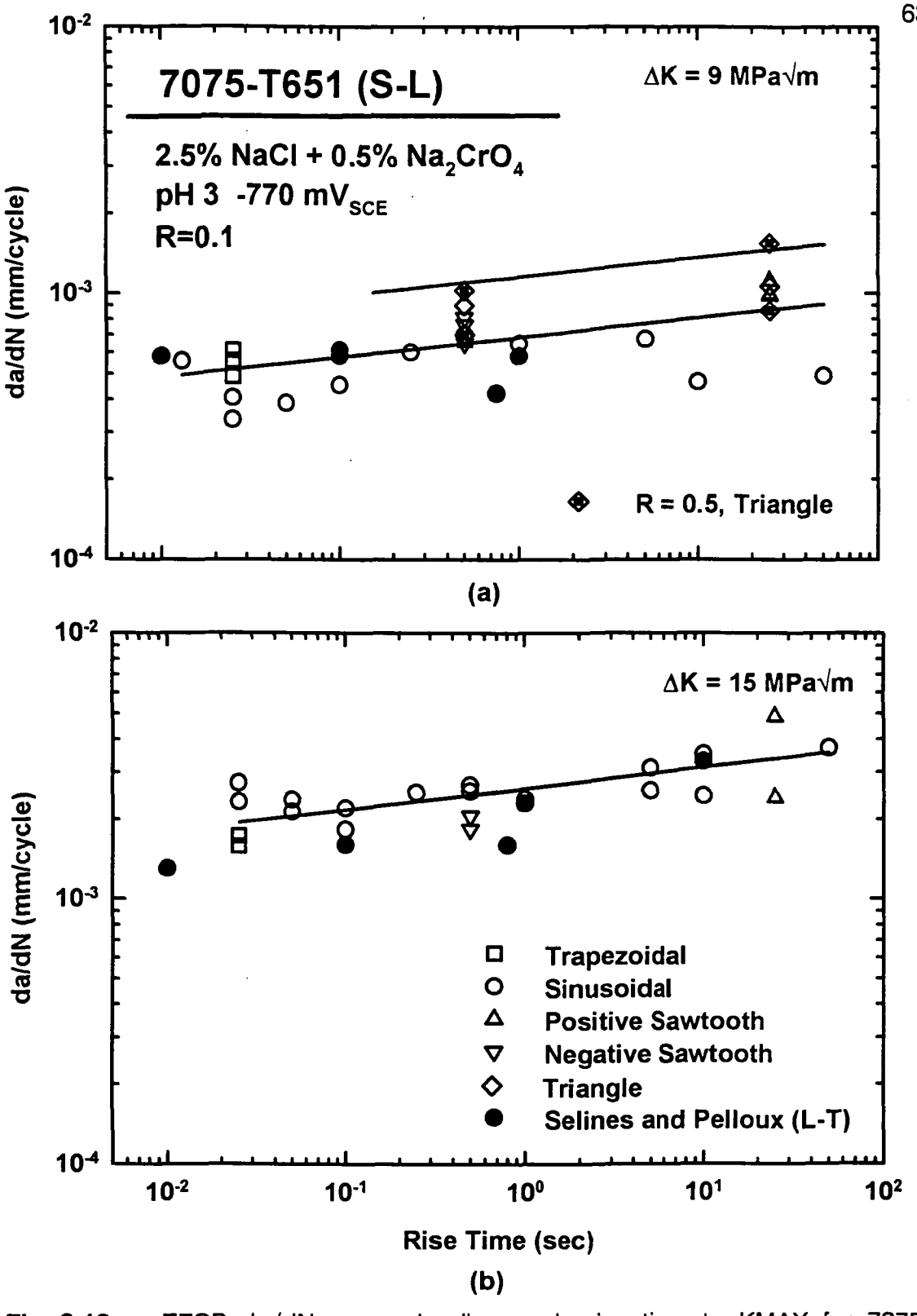

Fig. 3.12. EFCP da/dN versus loading cycle rise time to KMAX for 7075-T651(S-L) in chloride. [27]

contrast to the well-known effect of crack orientation on $da/dt_{scc}(K)$. [5,14] Specifically, the S-L results in Fig. 3.7 are identical to limited da/dN values reported for 7075-T651 in the L-T orientation. [27,29] EFCP rates for trapezoidal loading of the S-L orientation (Fig. 3.10) are similar to literature data on trapezoidal loading of L-T 7075-T6. [29] The environmental effect on fatigue crack growth is identical for the S-L and T-L orientations with asymmetric triangular loading (Fig. 3.12). [27] The S-T and T-L orientations of peak aged 7075 exhibited identical FCP rates at a higher stress ratio (R=0.5) for both inert nitrogen and aggressive chloride environments. [46]

Since these corrosion fatigue crack growth rates are orientation-independent, it is reasonable to conclude that mildly time-cycle-dependent EFCP does not occur along high angle grain boundaries which are arrayed anisotropically in 7000 series aluminum alloy microstructures. Rather, EFCP may involve more isotropic intersubgranular or brittle transgranular damage processes.

3.2.6 Summary of EFCP da/dN

The results of all EFCP experiments with S-L 7075-T651 in aqueous chloride are summarized in Fig. 3.13 and compared to the results of the continuous ΔK-decreasing experiment with this alloy in moist air and peak aged 7075 in inert environments. [47] Constant stress ratio ΔK-decreasing NaCl results at 5 Hz (Fig. 3.5) are represented by the smaller solid diamonds (♦) in Fig. 3.13 as described by the Paris power-law relation shown by the solid line. The large symbols (♦) for

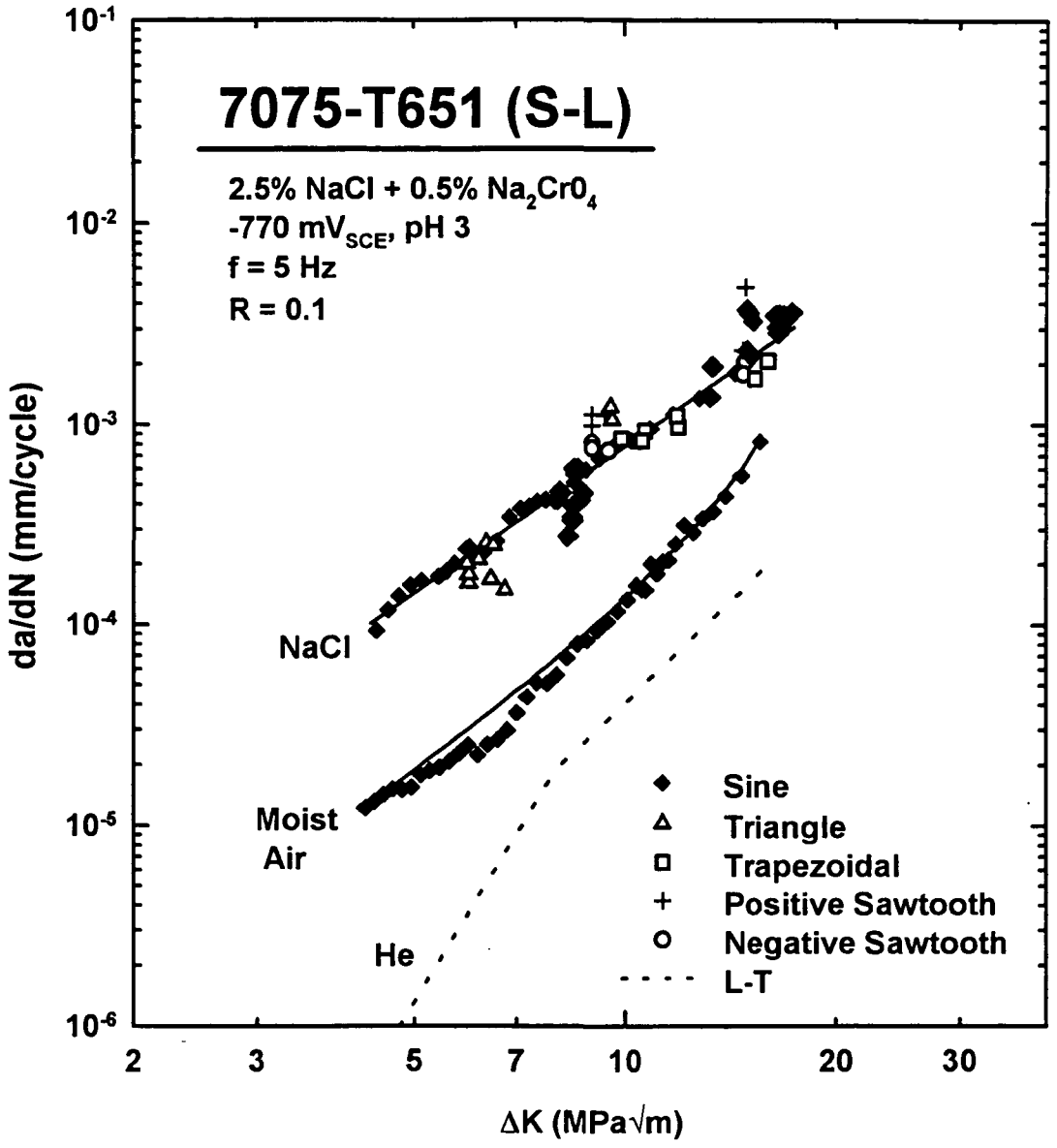

Fig. 3.13. EFCP data for 7075-T651/NaCl under several loading frequencies, waveforms, and ΔK control formats. [47]

sinusoidal loading represent results from constant ΔK, variable frequency experiments (Fig. 3.7). The 5 Hz ΔK-decreasing results are in good agreement with the data from the various constant ΔK experiments with sinusoidal loading, as well as with the data for trapezoidal (Fig. 3.10) and triangular (Fig. 3.12) K(t) functions.

3.3 Scanning Electron Microscopy of Environment Enhanced Fracture

3.3.1 SCC Fractography

Scanning electron microscope fractographs representative of the SCC fracture surface are presented in Fig. 3.14 for K-independent cracking at: (a) K of 18.7 MPa$\sqrt{m}$ and da/dt_{scc} of 1.4×10^{-9}, and (b) K of 20 MPa$\sqrt{m}$ and da/dt_{scc} of 4.4×10^{-9} m/sec. Crack propagation is from top to bottom. Both K levels are typified by large flat rippled fracture regions lying parallel to the rolling plane, labeled 1 in Figs. 3.14a and b. The length and width of type 1 features correspond to average grain dimensions (T of 100 to 200 μm, L of 1 mm) on the short transverse cracking plane. This observation implicates stress corrosion crack growth along favorably oriented crystallographic planes within grains or, since no river markings were observed, more probably along grain boundaries. Stereo imaging of the fracture surfaces shows that the bright features, labeled 2, are steps, probably both intergranular and transgranular, connecting flat areas. Additionally, fracture surfaces from higher K levels are populated with rough surface features, labeled 3, typically adjacent to the steps. Generally the portion of fracture surface area

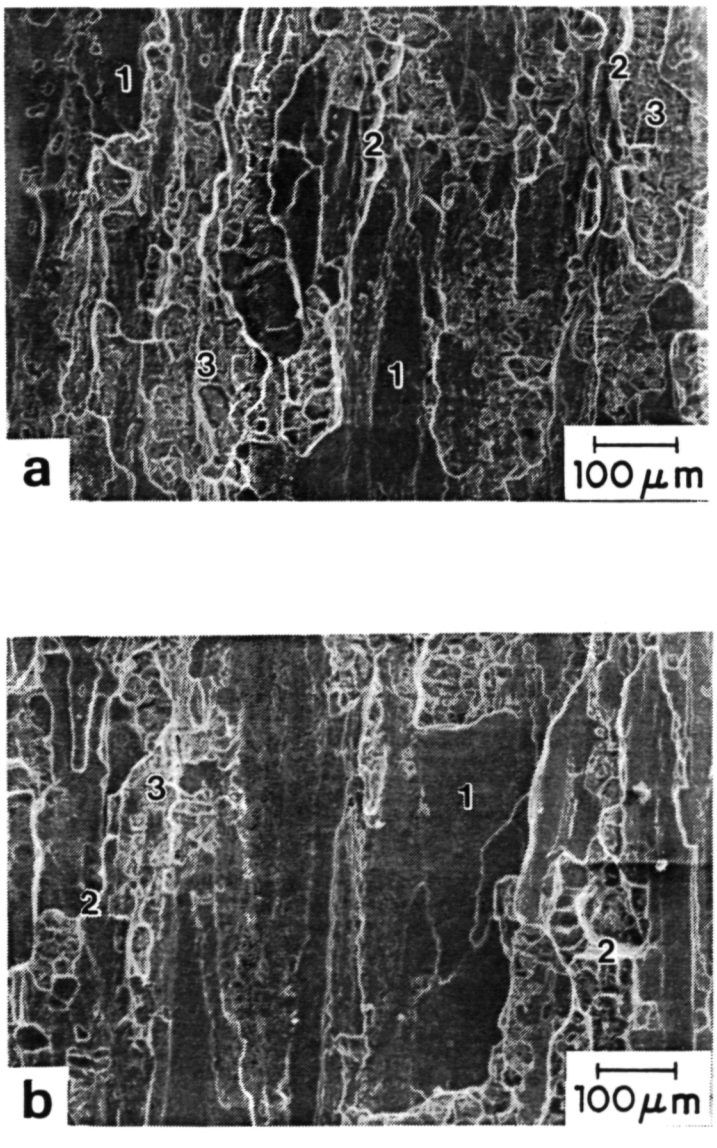

Fig. 3.14. SEI SEM fractograph of 7075-T651(S-L)/NaCl at (a) K of 18.7 MPa√m and (b) K of 20 MPa√m showing flat areas (type 1), transgranular steps (type 2), and rough (type 3) features. Crack propagation is from top to bottom.

covered by Type 1 features decreases with increasing K while Type 3 features become more dominant as K increases. Type 2 features account for a small fraction of fracture surface area for stress intensities examined.

Figures 3.15a, b, and c are fractographs of a flat rippled (1) area produced at a K of 11 MPa$\sqrt{m}$ (da/dt_{scc} of 3.5 x 10^{-9} m/sec). Type 1, 2, and 3 features are observed at low magnifications in Fig. 3.15a, with the lower arrow indicating the Type 1 feature shown at a higher magnification in Fig. 3.15b and the upper arrow indicating the type 1 feature shown in Fig. 3.15c. Higher magnification fractographs (Fig. 3.15b and c) reveal 1 to 5 μm facets on the Type 1 feature. As shown by arrows in Fig. 3.15b, facets are partially obscured by what are likely corrosion products since this segment of crack surface was immersed in solution for over 300 hours. An estimate, based on a passive current density of 0.02 A/m^2 [15], yields a corrosion penetration rate of 2.5 nm/hr, corresponding to the loss of approximately 0.75 μm of alloy from the surface in 300 hours; corrosion may have distorted an initially sharper feature. [49] Figure 3.15c shows a similar flat area, within 200 μm of Fig. 3.15b and under identical constant K loading, that has a more clearly faceted appearance. Since the typical subgrain size for unrecrystallized 7075 type alloy variants is 1 to 10 μm, [50] an intersubgranular fracture path is possible for the flat rippled fracture regions. Alternately, Type 1 features are grain boundary cracking, as suggested by Holroyd and Hardie for corrosion fatigue of 7017-T651(S-L) in unpolluted seawater, which had an identical fracture morphology to that shown in Fig. 3.15c.

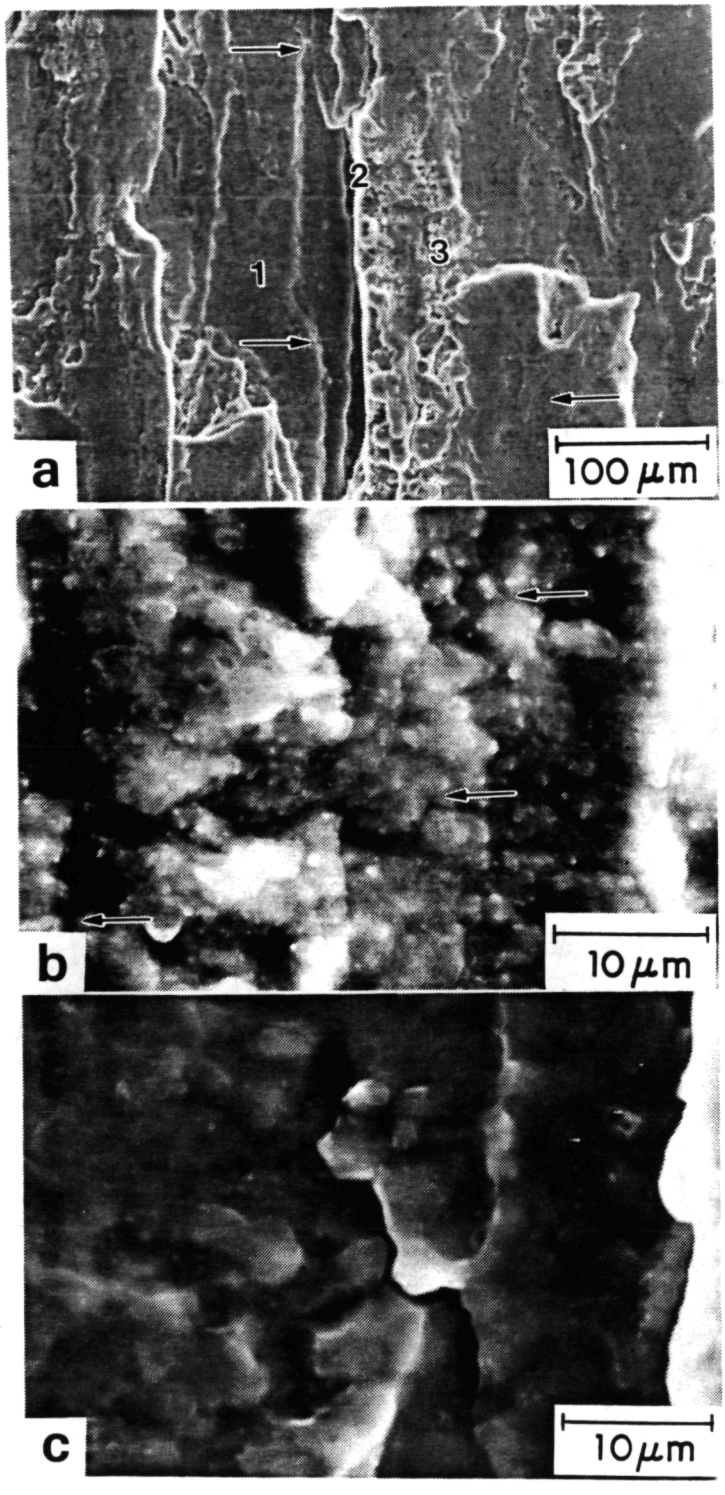

Fig. 3.15. SEI SEM fractographs of 7075-T651(S-L) stress corrosion crack surface features: (a) flat areas at 11 MPa√m; (b) higher magnification of (a) showing facets (marked by arrows) and corrosion debris; (c) higher magnification of (a) showing facets only.

A fractograph of an air overload fracture surface for S-L oriented 7075-T651 is presented in Fig. 3.16a and compared with the fractograph in Fig. 3.16b, showing the rough features labeled 3 to the right of center in Fig. 3.14b. The rough regions in SCC are similar to air overload fracture. While da/dt_{scc} is constant, the similarity of these Type 3 rough areas to air overload fracture surfaces, and the increasing abundance of rough areas observed at higher stress intensities, supports the notion of local tunneling SCC cracks. [15] Higher applied stress intensities would favor a larger area fraction of overload fracture, the Type 3 morphology, between tunneling SCC cracks. Dimples, denoted by arrows in Fig. 3.16b, are revealed in the step regions. However, fractured constituent particles observed in the rough areas in air overload fracture are not observed in Type 3 features for SCC.

Environment crack growth segments were produced by constant ΔK and ripple loading experiments, adjacent to quasi-static EAC surfaces at comparable stress intensity levels, for fractographic comparison. The fractographic results in Figs. 3.14 to 3.16 are compared with SEM analyses of ripple loading and constant ΔK segments in ensuing sections.

3.3.2 Fractography of Ripple Loading Fracture

Figure 3.17 shows the adjacent 5 and 30 Hz ripple loading fracture surfaces, bracketed by fatigue crack growth at ΔK of 11 MPa$\sqrt{m}$ for 7075-T651 (S-L) in NaCl. In all fractographs crack propagation is from top to bottom. The bright area below

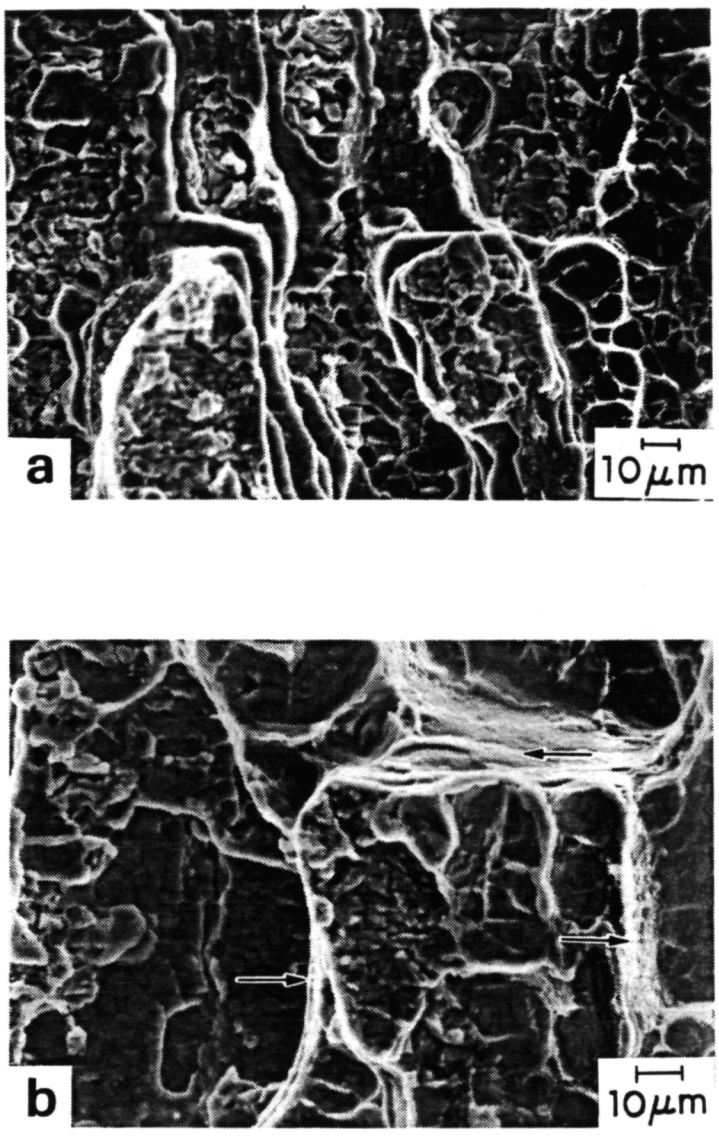

Fig. 3.16. SEI SEM fractographs of 7075-T651(S-L) of (a) overload fracture in air showing typical overload surface features of cracked particles and dimples; (b) quasi-static environmental cracking showing rough, region 3 (denoted by arrows), SCC features. Crack propagation is from top to bottom.

the arrow in Fig. 3.17 is the 30 Hz ripple loading segment. The 5 Hz segment of ripple loading produced 1 mm of crack growth above the arrow, preceding the 30 Hz segment. This fractograph confirms the approximately 1 mm of crack growth for the 30 Hz segment measured by DCPD. The 30 Hz segment is easily distinguished from the following overload fracture surface and a transition from the 5 Hz to 30 Hz is seen. However, the 5 Hz segment cannot be clearly differentiated from the ΔK of 11 MPa$\sqrt{m}$ crack surface.

Closer examination of the 5 Hz ripple (Fig. 3.18a) and 30 Hz ripple (Fig. 3.18b) surfaces at the specimen midplane shows two features resembling those seen prominently in high stress intensity SCC (see Fig. 3.16b). Rough areas, similar to Type 3 fracture in SCC are present on the ripple loading fracture surface and labeled 3 in Fig. 3.18. High magnification fractography of the 30 Hz ripple loading surface in Fig. 3.18b is shown in Fig. 3.19a. Comparison of the regions denoted by arrows in Fig. 3.19a with air overload fracture surfaces (see Fig. 3.16a) shows similarities also noted for Type 3 SCC cracking. As in SCC, steps with ductile features, labeled 2 in Figs. 3.18a, 3.18b, and 3.19a, connect relatively flat fracture regions and appear bright in SEM fractography.

In contrast to the SCC-like Type 2 and 3 features, the flat areas denoted by small arrows in Fig. 3.18 show features characteristic of corrosion fatigue fracture. Higher magnification fractography of a typical flat area denoted by the large arrow in Fig. 3.18a is shown in Fig. 3.19b, revealing brittle striations similar to those reported for corrosion fatigue of 7075 in 0.2 N NaCl at a ΔK of 15 MPa$\sqrt{m}$. [23]

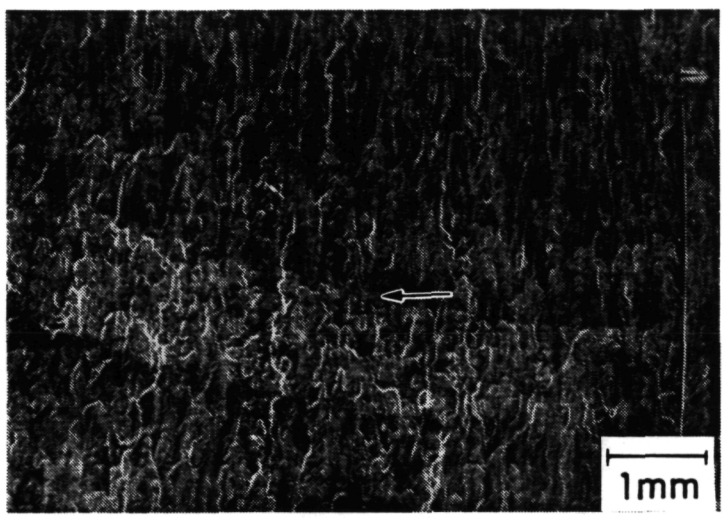

Fig. 3.17. SEI SEM fractograph of 7075-T651(S-L)/NaCl under low amplitude ripple loading showing macroscopic surface features for 5 Hz (above arrow) and 30 Hz (below arrow) ripple loading. Crack propagation is from top to bottom

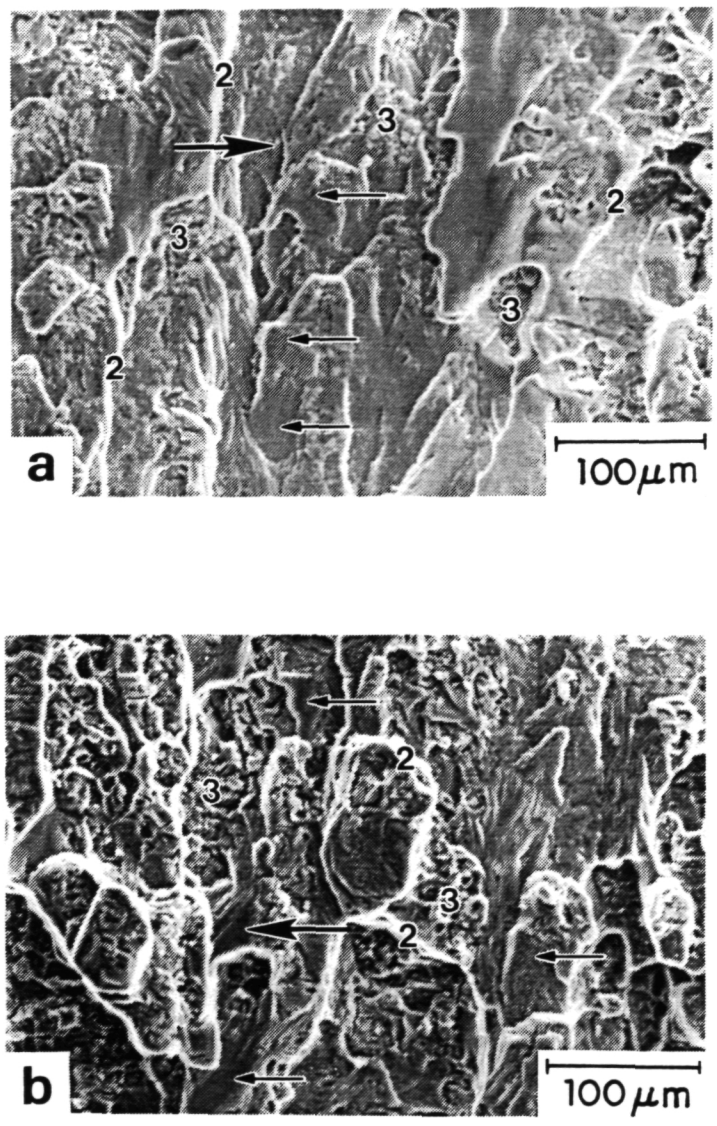

Fig. 3.18. SEI SEM fractographs of 7075-T651(S-L) under low amplitude (ΔK of 0.7 MPa$\sqrt{m}$) high sustained K_{MAX} (11 MPa$\sqrt{m}$) ripple loading showing Type 2 and Type 3 SCC features for both (a) 5 Hz and (b) 30 Hz ripple loading. Features typical of corrosion fatigue are observed for flat areas (marked by arrows).

The features in Fig. 3.19b that appear similar to Type 1 facets produced by SCC do not appear faceted at higher magnifications and are dissimilar to Type 1 SCC features identified as facets (Fig. 3.15). Although similar to high K SCC at low magnifications, the ripple loading surfaces appear striated and fatigue-like at higher magnifications. High magnification fractography revealed that the facets observed in flat areas on the ripple loading fracture surfaces were more similar to brittle striations than the Type 1 facets observed in SCC. The facets in Fig. 3.15c do not show a striation-like periodicity as seen in Fig. 3.19b for ripple loading. In addition, the facets in Fig. 3.19b appear slightly smaller than the SCC facets shown in Fig. 3.15.

While both 5 Hz and 30 Hz ripple load fracture surfaces have regions of brittle striations, a fractograph of another common type of striated feature, denoted by a large arrow in Fig. 3.18b and observed only on the 30 Hz ripple surface, is presented in Fig. 3.19c. The striation spacing of about 1 μm does not correspond to da/dN and the mating fracture surface was not examined to determine whether the striations are due to plastic deformation or crystallographic-type brittle cracking. These striations are not similar to brittle striations reported for corrosion fatigue of 7075 in 0.2 N NaCl at ΔK of 15 MPa$\sqrt{m}$ [23] and are quite different from those shown in Fig. 3.19b. The striation morphologies shown in Fig. 3.18b and c were equally prevalent on the 30 Hz ripple loading fracture surface.

The fracture surfaces of both the 5 Hz and 30 Hz ripple segments resemble those seen for corrosion fatigue cracks in 7075-T651(S-L)/NaCl (see Fig. 3.20 to

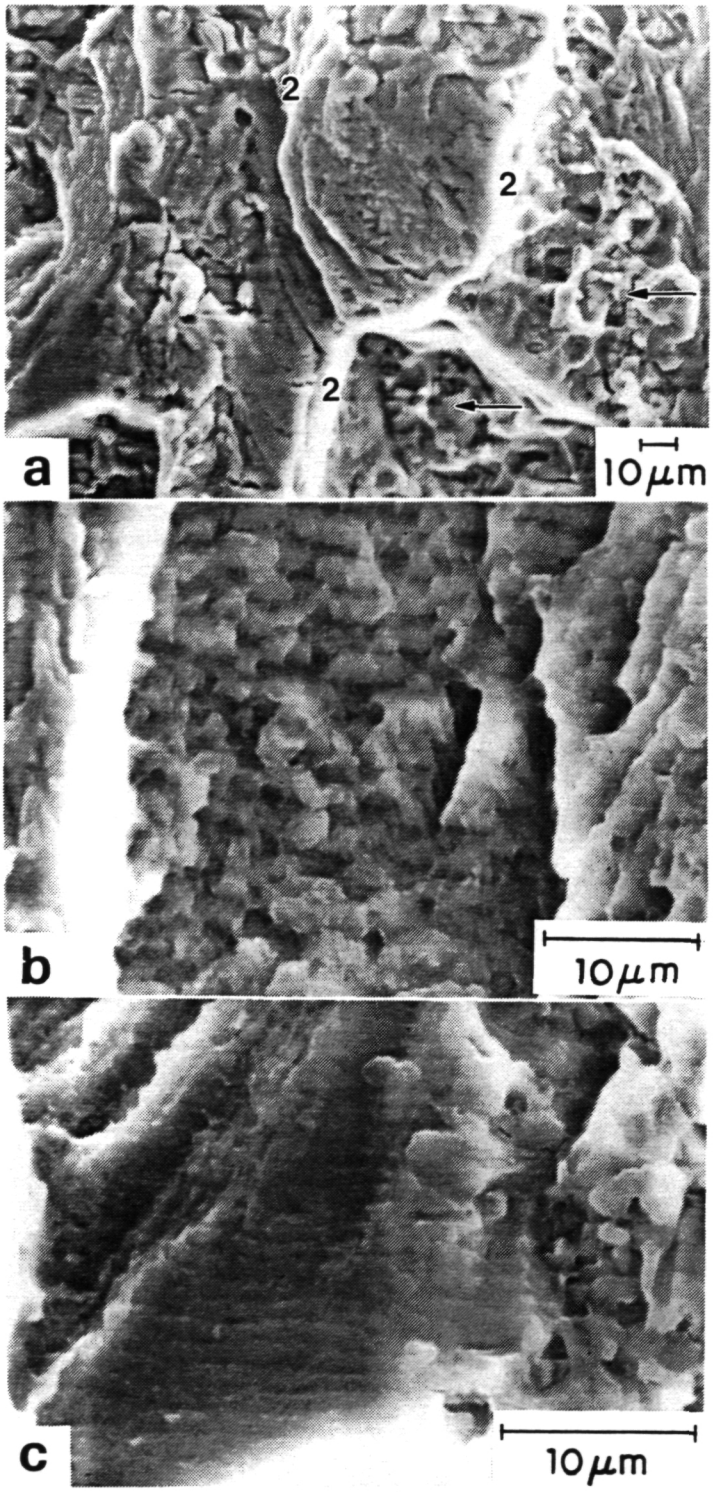

Fig. 3.19. SEI SEM fractographs of 7075-T651(S-L) under ripple loading in NaCl showing: (a) rough fracture regions for 30 Hz (marked by arrows), similar to Type 3 SCC features; (b) brittle striations observed for both 5 Hz and 30 Hz ripple loading; (c) striations observed only on 30 Hz ripple loading fracture surface.

3.23) at loading frequencies above 5 Hz. From these observations it appears that crack propagation during the ripple loading experiments was by near-threshold corrosion fatigue. Intergranular or intersubgranular quasi-static SCC was not promoted by the faster crack tip strain rates, consistent with the similar values of da/dt presented in Fig. 3.4.

3.3.3 Fractography of Constant ΔK Fatigue Fracture

SEM fractographs of EFCP are presented in Fig. 3.20a through d for two ΔK levels (15 MPa√m and 8.5 MPa√m) and two frequencies (20 Hz and 0.01 Hz) for 7075-T651 (S-L) in chloride. Crack propagation is from top to bottom. Four types of fracture surface features, labeled A, B, C, and D in Fig. 3.20 through Fig. 3.23, are present for these ΔK and frequency ranges.

At a frequency of 20 Hz and ΔK of 15 MPa√m (Fig. 3.20a), the fracture surface consists of rough flat regions, labeled A, which are macroscopically similar to the rough regions in SCC, identified as overload fracture by comparison to air overload fracture surfaces. While Fig. 3.20a shows Type A features covering most of the fracture surface, the proportion of Type A features decreases with frequency as seen for ΔK of 15 and frequency of 0.01 Hz in Fig. 3.20b.

Figures 3.21a,b and c show Type A areas that resemble air overload fracture surfaces for EFCP at a wide range of ΔK and frequencies. High magnification fractography reveals that, unlike the Type 3 features observed in SCC, which were associated with overload fracture, the Type A features have a

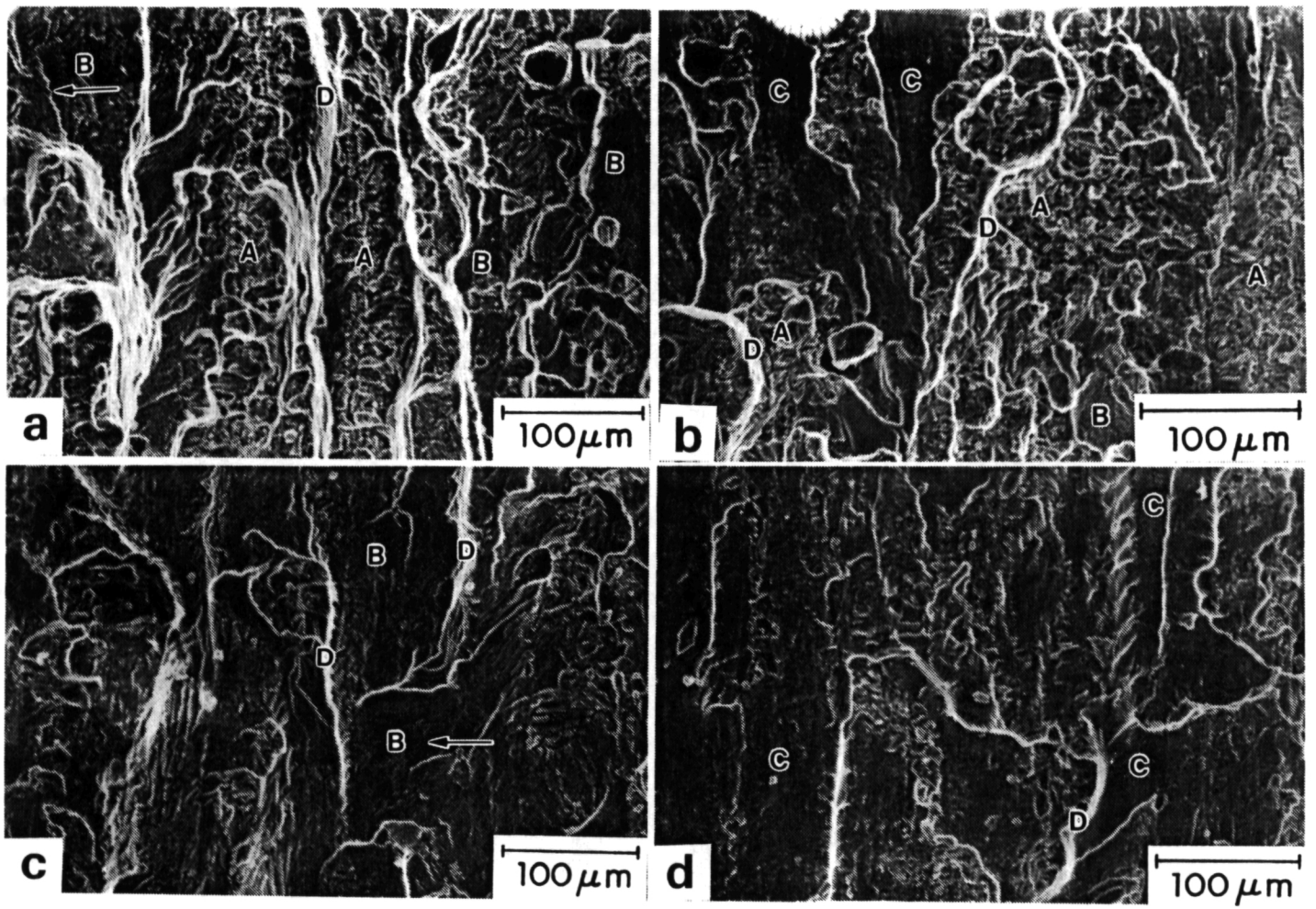

Fig. 3.20. SEI SEM fractographs of 7075-T651(S-L)/NaCl corrosion fatigue (R=0.1) fracture surfaces showing typical rough (A), flat (B and C), and step (D) features at (a) ΔK of 15 MPa√m, 20 Hz (b) ΔK of 15, 0.01 Hz (c) ΔK of 8.4 MPa√m, 20 Hz (d) ΔK of 8.7 MPa√m, 0.01 Hz. Arrows denote locations of Fig. 3.21a (upper) and Fig. 3.21b (lower).

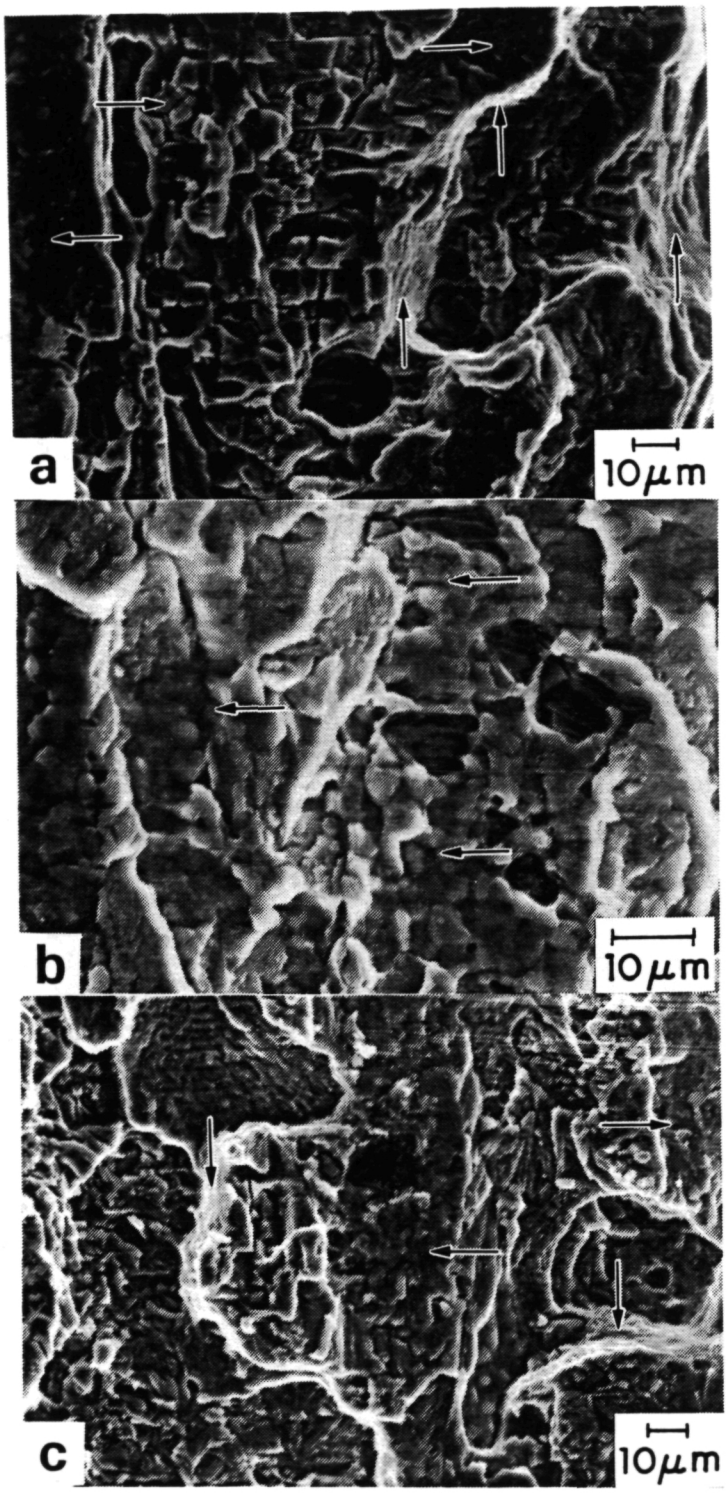

Fig. 3.21. SEI SEM fractographs of 7075-T651(S-L)/NaCl corrosion fatigue fracture surfaces showing rough flat areas at: (a) ΔK of 17 MPa$\sqrt{m}$ and 2 Hz; (b) ΔK of 6.3 MPa$\sqrt{m}$ and 5 Hz; (c) ΔK of 15 MPa$\sqrt{m}$ and 0.01 Hz. Faceted fracture features (marked by horizontal arrows) and transgranular steps (vertical arrows) are observed.

predominantly faceted appearance. Faceted fracture features are present on an increasing area fraction of Type A fracture surfaces as ΔK decreases (Fig. 3.21b) and frequency decreases (Fig. 3.21c). The facets within Type A fracture surfaces, denoted by horizontal arrows in Fig. 3.21b and Fig. 3.21c, are similar to facets observed in intersubgranular SCC. The proportion of fracture surface Type A features were observed to decrease with decreasing ΔK, as shown in Fig. 3.20a versus c and Fig. 3.20b versus d.

The faceted appearance of Type A features implicates grain boundaries as a possible fracture path since cracking along high angle grain boundaries may have a faceted appearance. Alternately, the dissimilarity between the features in Fig. 3.21b and mechanical overload in air (Fig. 3.16a) could indicate intersubgranular EFCP. Increasing proportion of Type A features with increasing ΔK, the similarity to SCC overload features, and intersubgranular cracking features could indicate hydrogen enhanced fracture involving subgrain boundaries.

Two types of flat and relatively smooth regions are observed and denoted by B and C on the fractographs for both low and high ΔK in Fig. 3.20. Type B and C features are difficult to differentiate at low magnifications unless the brittle striation spacing (Type B) is well defined and visible as in the area denoted by B in Fig. 3.20b.

Figures 3.22a and b show high magnification fractographs of typical type B flat fracture surface features, characterized by a morphology that appears similar to Type C at low magnifications ($<$200X). The area in Fig. 3.22a is indicated by an

arrow in Fig. 3.20a and the arrow in Fig. 3.20c shows the location of Fig. 3.22b. Stoltz and Pelloux identify features similar to Type B as brittle striations for fatigue cracks in 7075-T6(L-T) tested in distilled water. [23] Type B features were observed at frequencies above 1 Hz for ΔK of 8.5 MPa$\sqrt{m}$ and at all frequencies for ΔK of 15 MPa$\sqrt{m}$. The proportion of Type B features within flat fracture surfaces increased with increasing frequency for all frequencies examined for ΔK of 15 MPa$\sqrt{m}$ and above 1 Hz for ΔK of 8.5 MPa$\sqrt{m}$.

The high magnification fractograph of Type C features seen in Fig. 3.23 is of a fracture surface produced by a ΔK of 11 MPa$\sqrt{m}$ and a frequency of 5 Hz. Figure 3.23 shows faceted fracture identical to the faceted intersubgranular fracture observed in SCC (see Fig. 3.10). Stereo imaging of the features in Fig. 3.23 reveals that the right half, as divided by the crack down the center is on a higher plane than the more clearly faceted left half. The facets on the right half of the fractograph appear to be plastically deformed, perhaps by the closure-producing mating fracture surface which may have prevented contact between the left half and its mating fracture surface. SEM fractographs of intergranular corrosion fatigue of 7017 in seawater show an identical facet morphology for frequency independent da/dN. [10] Rechberger identified these regions as intergranular and reported intergranular striations for a ΔK of 7.6 MPa$\sqrt{m}$ and higher R of 0.31 in 3.5 wt pct NaCl. [9] Intergranular striations were not observed in the limited amount of high magnification fractography performed.

Typically connecting Type A, B, and C morphology are bright areas, labeled

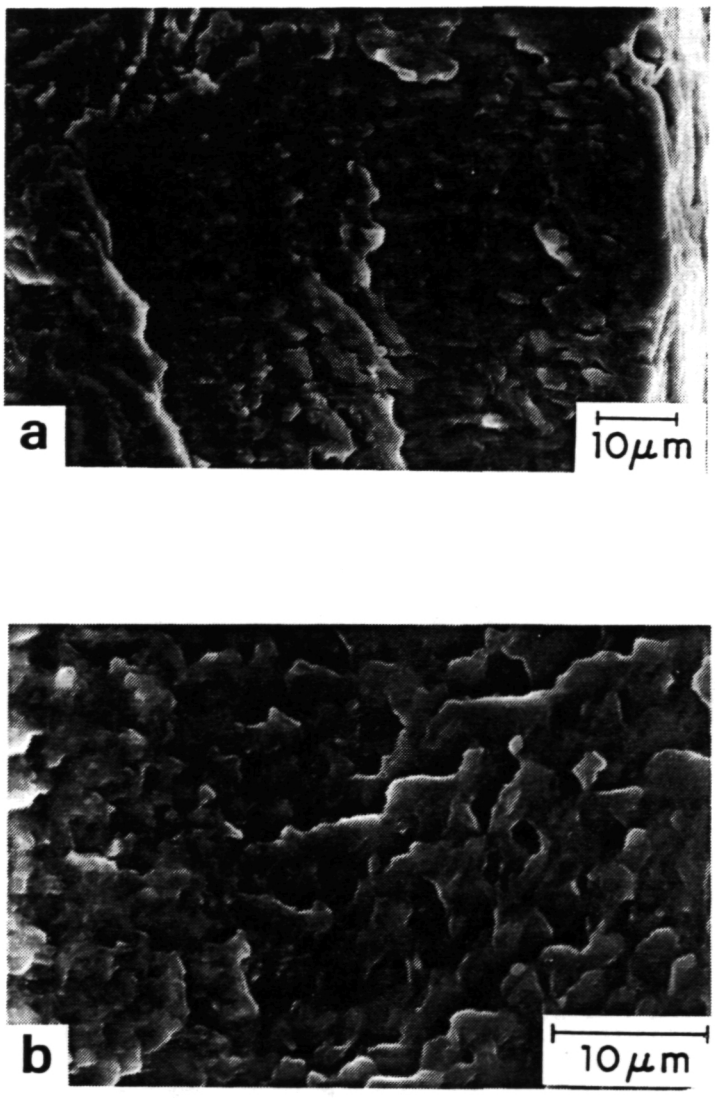

Fig. 3.22. SEI SEM fractographs of corrosion fatigue fracture surfaces of 7075-T651(S-L)/NaCl showing typical brittle striation (Type B) morphology.

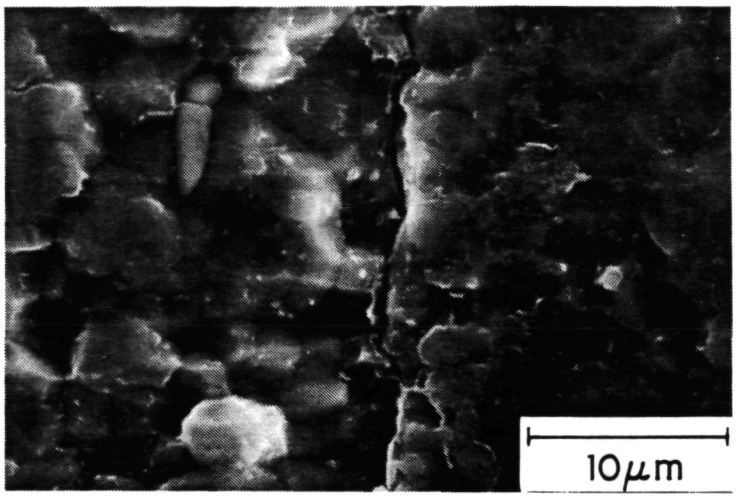

Fig. 3.23. High magnification SEI SEM fractograph showing corrosion fatigue facets and plastic deformation of facets due to interference with the mating fracture surface for 7075-T651(S-L) in NaCl.

D, identical to the transgranular step fracture regions seen in SCC (see Fig. 3.14). As with SCC fractographs, stereo imaging shows that the bright areas are steps with ductile features, connecting relatively flat fracture regions of varying morphology. Figure 3.21 shows examples of steps produced at a ΔK of 17 MPa$\sqrt{m}$ and frequency of 2 Hz (Fig. 3.21a), and ΔK of 15 MPa$\sqrt{m}$ and frequency of 0.01 Hz (Fig. 3.21c) with a characteristic ductile dimpled overload fracture mode area indicated by vertical arrows. The relative heights of the steps appeared to decrease with ΔK, consistent with smaller cyclic plastic zone sizes affecting diminished volumes of material ahead of the advancing corrosion fatigue crack.

EFCP of 7075-T651 (S-L) in chloride at high ΔK (eg., 15 MPa$\sqrt{m}$) is characterized by a mixture of intersubgranular and transgranular fracture morphologies, with the area fraction of intersubgranular faceted fracture increasing with decreasing frequency. The proportion of the flat features containing brittle striations decreased with decreasing frequency. Brittle striations were observed for all frequencies at a ΔK of 15 MPa$\sqrt{m}$, however, no brittle striations were observed below 1 Hz for a ΔK of 8.5 MPa$\sqrt{m}$; intersubgranular and rough overload fracture were most prominent for the low ΔK and frequencies below 1 Hz. Steps between flat fracture regions (Types A, B, and C) showed ductile fracture features and the height of the steps decreased with decreasing ΔK.

3.4 CONCLUSIONS

1. Da/dt_{scc} values are consistent with K-independent cracking above a K_{Iscc} of 5 to 10 MPa$\sqrt{m}$. However, da/dt_{scc} ranges from 0.3 to 4.4 x 10^{-9} m/sec and is slower than literature results.

2. Primarily intersubgranular fracture at low stress intensity, with an increasing area fraction of overload fracture similar to mechanical overload in air and transgranular steps at stress intensities approaching K_{IC}, is observed for SCC of 7075-T651(S-L) in an acidified chromate inhibited chloride environment under constant CMOD or constant stress intensity loading. High angle boundary cracking was not a prominent feature for SCC for 7075-T651(S-L) in this study.

3. Imposed constant crack mouth opening displacement rate does not accelerate environmentally enhanced da/dt above da/dt_{scc}.

4. Da/dt is not enhanced by high frequency-low amplitude cyclic loading, designed to increase crack tip strain rate, in conjunction with a high sustained stress intensity.

5. SEM fractography of the 5 Hz and 30 Hz ripple loading fracture surfaces

shows corrosion fatigue features. No intersubgranular cracking indicative of SCC or low frequency corrosion fatigue is observed.

6. Fatigue crack propagation rates for 7075-T651(S-L) in chromate inhibited, acidified NaCl solution are enhanced five to ten-fold over rates in moist air and are over an order of magnitude faster compared to cracking in helium.

7. Results from a single constant ΔK experiment (9 MPa$\sqrt{m}$), and comparison with literature results for the S-L and L-T orientations, indicate that EFCP da/dN are identical for acidified chromate inhibited and neutral uninhibited environments.

8. EFCP da/dN for 7075-T651(S-L) in NaCl shows a weak time-cycle frequency dependence above 0.001 Hz. Above 0.001 Hz, EFCP da/dN is proportional to f^{β} where β approximately equals 0.1.

9. Corrosion fatigue is predominantly intersubgranular for low frequencies and ΔK levels (below 0.1 Hz for ΔK of 9 MPa$\sqrt{m}$) for the S-L orientation of 7075-T651 in NaCl, with regions of transgranular fracture in the form of brittle striations, and steps between flat areas of intersubgranular fracture. Higher frequencies and ΔK levels showed primarily a transgranular fracture morphology.

10. For 7075-T651 in the S-L orientation, results from corrosion fatigue experiments at two constant stress intensities indicate a very small effect of hold-time for the loading and unloading rates and times tested.

11. EFCP da/dN is proportional to t_R^m for a wide range of rise times, where m is approximately 0.1 for both symmetric and asymmetric loading waveforms for 7075-T651(S-L) in acidified chromate inhibited NaCl.

12. The NaCl environmental effect on time-cycle-dependent fatigue crack growth is identical for the S-L and L-T orientations of peak aged 7075, suggesting a minimal involvement of anisotropic high angle grain boundaries.

13. Compliance estimations of $K_{CLOSURE}$ and comparison with DCPD results for EFCP of 7075-T651 in NaCl indicate a negligible effect of time-dependent crack closure on frequency and rise time dependencies of da/dN for ΔK of 9 and 15 MPa$\sqrt{m}$. Intrinsic effects of stress ratio on da/dN in chloride were inseparable from the contributions of time-dependent closure.

Chapter 4. Discussion

4.1 Linear Superposition Modeling

4.1.1 Background

The success in modeling EFCP da/dN for high strength steels and precipitation hardened aluminum alloys in chloride using linear superposition (Equation 1.1) is attributed to high da/dt_{scc} relative to mechanical da/dN times frequency and low K_{iscc} relative to K_{ic}. [17] For example, time dependent EFCP for 7079-T651 is predicted by linear superposition. [4] However, 7079-T651 (S-L) has a high da/dt_{scc} (10^{-5} m/sec in saturated NaCl solution) which limits practical application of the alloy in aggressive environments. [4,14]

7075-T651 is a widely used high strength aluminum alloy; K_{iscc} of 5 MPa$\sqrt{m}$ and well known stress corrosion cracking susceptibility in the S-L orientation (see Fig. 3.1) indicate that 7075-T651 is an ideal candidate for modeling EFCP da/dN via linear superposition, and for studying the complex time and strain rate dependencies of da/dN. [5,12,13]

4.1.2 Model Application

For linear superposition modeling, $da/dt_{scc}(K)$ was equated to the average measured K-independent Stage II velocity of 4×10^{-9} m/sec (see Table 3.1) for 7075-T651 (S-L) in NaCl, and assuming no crack growth below a K_{iscc} of 5 MPa$\sqrt{m}$. FCP rates for L-T 7075-T651 in helium or vacuum comprised the mechanical component. [47] Equation 1.1 was integrated numerically to yield the predicted

EFCP rates that are shown in Fig. 4.1 for fixed frequencies between 0.01 and 20 Hz, with K varying sinusoidally as a function of time. [1] These predictions are compared with experimentally determined corrosion fatigue data, generated with sinusoidal loading at 5 Hz and presented previously in Fig. 3.5.

Linear superposition underpredicts substantially 5 Hz EFCP rates for 7075-T651 in NaCl, as similarly reported for 7017 and 7475. [9,10] This error is attributed to the slow da/dt_{SCC} compared to the one to two orders of magnitude increase in actual aqueous da/dN values over inert helium. Due to the low value of da/dN_{SCC} relative to da/dN_{MECH}, predicted EFCP rates do not show an inverse frequency dependence for frequencies above 0.01 Hz.

At ΔK of 15 MPa$\sqrt{m}$, the measured EFCP rate is 2×10^{-3} mm/cycle. Applying Eq. 1.1 and a frequency independent da/dt_{SCC} of 4×10^{-6} mm/sec, da/dN_{SCC} provides a dominant contribution at frequencies less than 0.001 Hz. The da/dN_{CF} term, introduced by Wei and coworkers to account for time-cycle dependent EFCP da/dN, appears to dominate the frequency dependence of da/dN above 0.001 Hz because da/dN_{SCC} is small. [8] Figure 1.2 confirms that da/dN depends on f^{-1} for 7075, but only for frequencies less than 0.001 Hz. Linear superposition may be used with confidence to predict EFCP da/dN in the 7075-T651(S-L)/NaCl system for sinusoidal frequencies below 0.001 Hz, and more generally, for corrosion fatigue waveforms having K levels in excess of K_{ISCC} for more than 1000 seconds. The EFCP behavior of 7079 shown in Fig. 1.2 is modeled similarly by linear superposition with da/dN_{SCC} becoming a dominant

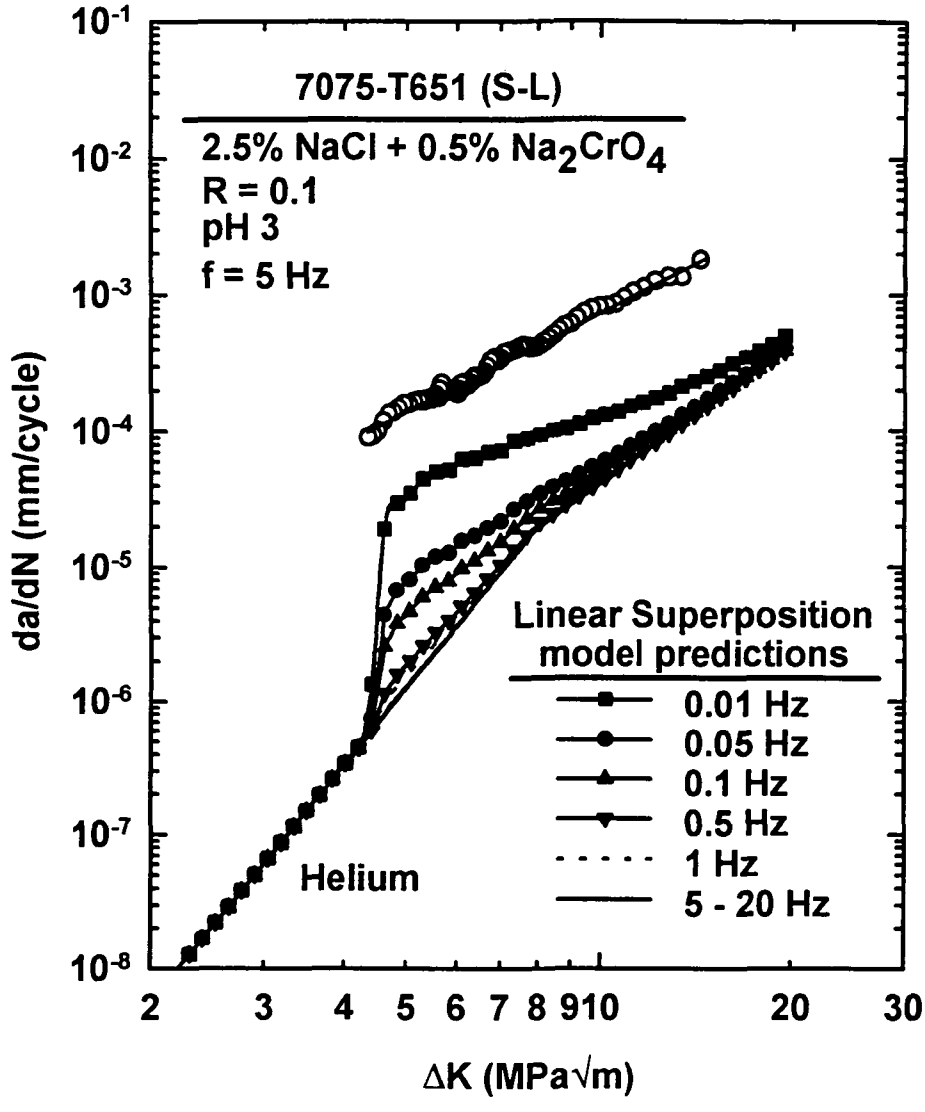

Fig. 4.1. Linear superposition model predictions of EFCP da/dN for 7075-T651(S-L) system compared with measured da/dN vs. ΔK at a frequency of 5 Hz and R of 0.1. [47]

factor below 1 Hz, consistent with the higher da/dt_{scc} of 10^{-5} m/sec. The reason for the several order of magnitude increase in da/dt_{scc} for 7079 is not known. [4,5]

Linear superposition fails to predict the mild time-cycle frequency dependence, between $f^{-0.1}$ and $f^{-0.5}$, observed for 7000 series alloys at frequencies where da/dN_{scc} becomes vanishingly small. [9,10,16] There are at least two possibilities for the failure of the linear superposition model to predict EFCP rate. Da/dt may be significantly enhanced by higher crack tip strain rates during a fatigue loading cycle compared to quasi-static loading; the accelerated da/dt needs to be determined and applied to the model. Alternately, da/dN_{CF} occurs by a different and competitive crack tip damage mechanism, and therefore must be considered separately from da/dN_{scc}.

4.2 Time-Dependent Environment Enhanced Fatigue Crack Propagation

The experimental results for 7075-T651 (S-L) in aqueous NaCl illustrate the complexities of describing EFCP in a fatigue life prediction code such as NASA FLAGRO. While K_{Iscc} is low, da/dt_{scc} is slow and the simple linear superposition of this quasi-static cracking rate with da/dN_{MECH} only describes frequency, ΔK, waveform and R-value effects on da/dN for slow loading frequencies below about 0.001 Hz and rise times above 500 seconds. Strong environmental effects on da/dN are none-the-less observed for higher frequencies, as illustrated by the data in Fig. 3.7. The effect of crack tip strain rate on EAC, and particularly on rate-limited hydrogen embrittlement ahead of the advancing fatigue crack, is discussed.

4.2.1 Hydrogen Embrittlement Mechanism for EAC in 7075

The role of hydrogen embrittlement in SCC of 7000 series aluminum alloys has been established by various experimental techniques and circumstantial evidence, including observations of stress corrosion crack growth. [51] The reversibility of preexposure embrittlement [51], the SCC susceptibility of specimens under cathodic potentials [52], and results showing susceptibility to embrittlement of 7075 by cathodically-precharged hydrogen [52-54] implicate hydrogen embrittlement participation in SCC. 7075 shows a greater susceptibility to cracking under Mode I loading, where the triaxial stress state assists hydrogen induced intergranular fracture, while Mode III cracks are claimed to propagate by anodic dissolution. [55] These results and others have collectively shown that both anodic dissolution and hydrogen embrittlement participate in subcritical crack propagation for 7000 series aluminum alloys in chloride environments. While anodic dissolution is necessary to supply hydrogen, the following discussion assumes EAC is largely due to HE with anodic dissolution accounting for a negligible proportion of crack advance and da/dt.

As in SCC, anodic dissolution to supply hydrogen to the crack tip process zone and the resulting dominant hydrogen embrittlement are likely operative in EFCP of 7075-T651 in chloride environments. [3,17] Explanations for ΔK-based transitions in fracture mode, and from time-cycle independent to time-cycle dependent da/dN, have been proposed based on HE for peak-aged 7475 and 7017 in chloride. [9,10] Enhanced da/dN dependent on water vapor pressure, at

low levels where anodic dissolution is not expected, supports HE in the cyclic process zone for EFCP. [22,26]

Hydrogen embrittlement models for corrosion fatigue of 7000 series aluminum alloys in chloride are based on a complex series of reactions which supply atomic hydrogen to the highly strained crack tip process zone. [3,9,10,17] These reactions are illustrated schematically in Fig. 4.2 and may be categorized as follows: reactions one through four govern production and uptake of hydrogen at the crack tip; five controls hydrogen transport within the crack tip process zone; and six and seven involve hydrogen partitioning to microstructural trap sites and process zone embrittlement. [3] For the following analysis, surface reaction rates and solution mass transport are assumed to be sufficiently fast to be non-rate-limiting. We will focus first on strain rate effects on surface integrity and hydrogen uptake, then on hydrogen diffusion in the process zone.

4.2.2 Crack Tip Strain Rate Effects

4.2.21 Background

The classic crack surface film rupture and transient dissolution model suggests that crack tip strain rate is a key factor in governing da/dt and relating da/dt to da/dN. [36,56] Alternately, mechanical disruption of the protective oxide film, and mobile dislocations from sources on the crack surface, both promoted by increasing strain rate or increasing film rupture events, could enhance da/dt by facilitating hydrogen production, entry, and transport in the process zone. [56]

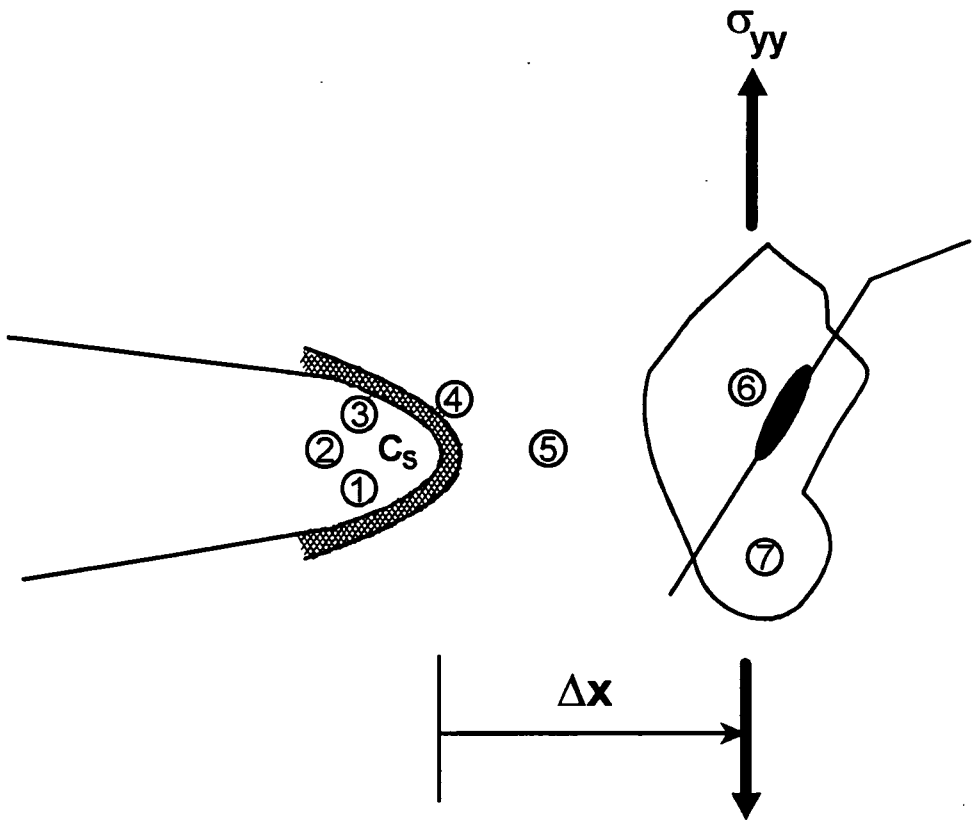

(1) Film rupture by crack tip strain

(2) Cation dissolution, hydrolysis, lowering pH

(3) H^+ and water reduction to H

(4) Transient crack tip film repassivation

(5) Hydrogen transport within crack tip process zone

(6) H partitioning to microstructural trap sites

(7) Process zone embrittlement

Fig. 4.2. Transport and reaction sequences that produce adsorbed hydrogen for interaction with the crack-tip stress field and process zone microstructure; after Gangloff. [3]

Since the crack tip strain rate during fatigue is substantially faster than that during crack growth under constant displacement, monotonic-loading da/dt determined at higher applied strain rates may provide a means to successfully model EFCP da/dN. Crack tip strain rate is estimated for monotonic and cyclic loading conditions, chosen to provide a wide range of strain rates, and compared with da/dt.

4.2.22 Crack Tip Surface Strain Rate Estimations

Crack tip strain rate ($d\epsilon_{CT}/dt$) depends on da/dt, crack tip creep deformation rate, stress intensity and loading rate. Little attention has been paid to estimating $d\epsilon_{CT}/dt$ for quasi-static loading due to the difficulty in quantifying the significant contributions of creep and crack velocity to $d\epsilon_{CT}/dt$. [56] Crack tip surface strain rate under constant K and CMOD conditions is likely much smaller than for rising load and fatigue. [3] Assuming negligible crack tip creep at ambient temperatures for relatively fast monotonic and cyclic loading rates, and for a static crack tip, $d\epsilon_{CT}/dt$ can be quantitatively estimated for rising load and fatigue conditions.

4.2.22A Monotonic Loading Strain Rate Estimation

Continuum fracture mechanics models predict strain and therefore strain rate singularities at the crack tip [57], however, a reasonable true crack tip surface strain (ϵ_{CT}) at a particular stress intensity may be estimated as follows:

$$\epsilon_{CT} = \ln\left(\frac{\delta}{\delta_0}\right) \tag{4.1}$$

where δ is the crack tip opening displacement (CTOD) in the Mode I opening direction, proportional to K^2 by:

$$\delta \approx \frac{K^2}{E\sigma_{YS}} \tag{4.2}$$

δ_0 is an initial gage distance normal to the crack plane. δ_0 is not precisely defined. [36,56]

The rate of change in ϵ_{CT} with time must be determined to obtain $d\epsilon_{CT}/dt$ for monotonic loading and for a stationary crack where da/dt is 0. Differentiating ϵ_{CT} (Eq. 4.1) with respect to time and combining this differentiation with Eq. 4.2 produces a relation for $d\epsilon_{CT}/dt$ in terms of K and loading rate, dK/dt:

$$\frac{d\epsilon_{CT}}{dt} \approx \frac{2}{K}\frac{dK}{dt} \tag{4.3}$$

showing that $d\epsilon_{CT}/dt$ is directly proportional to dK/dt, inversely proportional to K, and a gage length is not required to determine $d\epsilon_{CT}/dt$. Under monotonic loading dK/dt is constant prior to crack growth initiation and, assuming negligible contributions by crack tip creep and da/dt, $d\epsilon_{CT}/dt$ is determined at any instantaneous K level. For this study monotonic loading $d\epsilon_{CT}/dt$ is estimated at K_{TH}.

4.2.22B Fatigue Loading Strain Rate Estimation

For fatigue loading, calculation of $d\epsilon_{CT}/dt$ must assume a gage length and recognize that crack tip strain varies with time during a stress intensity cycle. These factors are uncertain. Alternately, very near-tip crack tip plastic strain range ($\Delta\epsilon_P$) was measured for 7075-T651 loaded cyclically at moderate ΔK levels. [58] Davidson and Lankford calculated $\Delta\epsilon_P$ from stereo measurements of very near-tip crack opening displacement during cyclic loading of 7075-T6 (L-T) in air and vacuum at an R of 0.2. [58] An empirical relation between $\Delta\epsilon_P$ and ΔK was reported:

$$\Delta\epsilon_P = K_0(\Delta K)^r \qquad (4.4)$$

K_0 and r are curve fit parameters. K_0 equalled 5.8×10^{-5} and r ranged from 2.5 to 3.5 where ΔK is in MPa$\sqrt{m}$, with 3.2 producing the best fit of Eq. 4.4 for 7075-T6(L-T) in moist air at ΔK levels of 6 to 12 MPa$\sqrt{m}$.

Average $d\epsilon_{CT}/dt$ over a fatigue stress intensity cycle is estimated by dividing $\Delta\epsilon_P$ by time under tensile loading, Δt:

$$\frac{d\epsilon_{CT}}{dt} = \frac{\Delta\epsilon_P}{\Delta t} \qquad (4.5)$$

If Δt is defined as the rise time (t_R) from K_{MAX} to K_{MIN}, $1/(2f)$ for symmetrical sinusoidal and triangular wave forms, then an average fatigue crack tip strain rate estimation, as a function ΔK and t_R (or f), follows:

$$\frac{d\epsilon_{CT}}{dt} = \frac{K_0(\Delta K)^r}{t_R} \qquad (4.6)$$

Crack tip surface strain rates for moderate ΔK levels are estimated using Eq. 4.6, however, it is not clear whether Eq. 4.6 may be extrapolated to estimate $d\epsilon_{CT}/dt$ for low ΔK ripple loading.

Shoji et al. proposed that crack tip strain rate may be calculated by multiplying measured da/dN for FCP in air by loading frequency and a constant, with da/dN in cm/cycle: [59]

$$\frac{d\epsilon_{CT}}{dt} = (10...100)\ f\ \frac{da}{dN_{AIR}} \qquad (4.7)$$

The presumption is that the time-based mechanical fatigue crack growth rate is directly related to the dislocation emission rate at the crack tip. Ford proposed that the proportionality constant is $(\delta\epsilon/\delta a)_K$, dependent on the change in load line displacement per unit of crack advance (dV_L/da). [56] From finite element calculations of $(\delta\epsilon/\delta a)_K$ versus dV_L/da expected under environmental cracking conditions, Ford suggests the proportionality constant ranges from 10 to 100.

Estimates of fatigue crack tip surface strain rate versus ΔK at 5 Hz using Eq. 4.6 and Eq. 4.7 (with a coefficient of 100), are presented in Fig. 4.3. This calculation demonstrates poor agreement between $d\epsilon_{CT}/dt$ based on stereoimaging measurements of near crack tip $\Delta\epsilon_P$ (Eq. 4.6) and $d\epsilon_{CT}/dt$ predicted by Eq. 4.7. Similar large differences in crack tip displacement-derived $d\epsilon_{CT}/dt$ and $d\epsilon_{CT}/dt$ from Eq. 4.7 were shown for stainless steels. [3,56] Additionally, both methods require

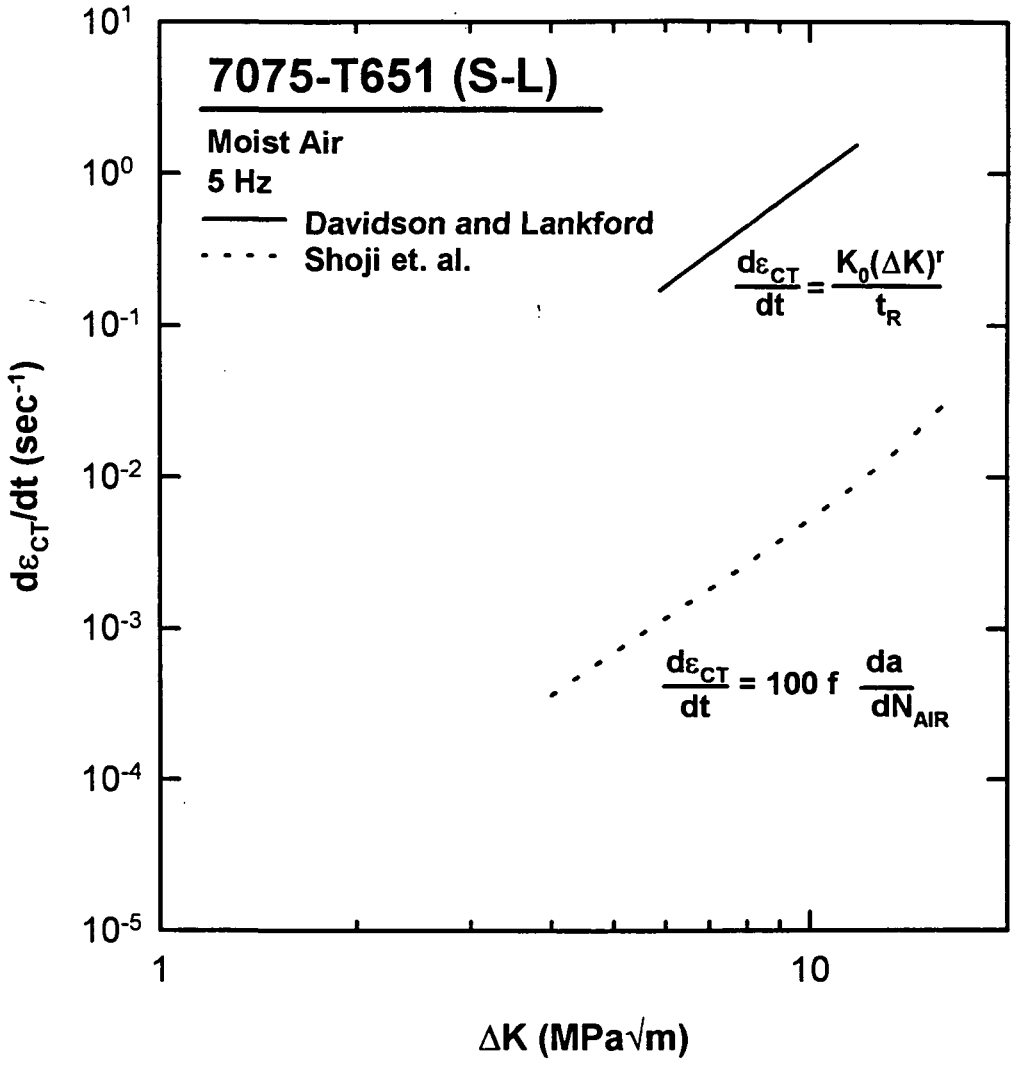

Fig. 4.3. Comparison of crack tip strain rate estimates versus ΔK for 7075-T651 at 5 Hz in moist air.

extrapolation to determine $d\epsilon_{CT}/dt$ for low ΔK ripple loading. Since $d\epsilon_{CT}/dt$ values from Eq. 4.6 are based on quantitative measurements of fatigue crack tip displacements for 7075-T6, Eq. 4.6 is used to estimate $d\epsilon_{CT}/dt$ for corrosion fatigue and extrapolated to estimate ripple loading $d\epsilon_{CT}/dt$.

The different approaches to estimating $d\epsilon_{CT}/dt$ represented in Fig. 4.3 yield a similar power law dependence on ΔK. This behavior results from the fact that both measured $\Delta\epsilon_P$ and da/dN depend on ΔK to the near-third power, coupled with the identical 1/f time dependence in each calculation. This comparison suggests that da/dN is approximately proportional to $\Delta\epsilon_P$. While the ΔK dependent plastic strain range distribution ahead of the crack tip is the driving force for fatigue, there is no modeling basis for expecting this proportionality between $\Delta\epsilon_P$ and ΔK.

4.2.23 Effect of Strain Rate on Environmental da/dt

Figure 4.4 presents da/dt versus estimated crack tip strain rate from either Eq. 4.3 for monotonic loading, or Eq. 4.6 for ripple and trapezoidal fatigue loading, of 7075-T651 (S-L) in chloride. Trapezoidal da/dt was determined via linear superposition to determine da/dN_{SCC} from the mild hold time dependence shown in Fig. 3.10 at a ΔK of 9 MPa$\sqrt{m}$, assuming a da/dN_{MECH} equal to da/dN at the shortest hold time. Da/dN_{SCC} was divided by the hold time at K_{MAX} to calculate da/dt. Trapezoidal $d\epsilon_{CT}/dt$ was calculated using the fast rise time from K_{MIN} to the onset of τ_H at K_{MAX}. The hypothesis is that high $d\epsilon_{CT}/dt$, during fast loading times for a trapezoidal waveform, enhances da/dt for at least a portion of the following

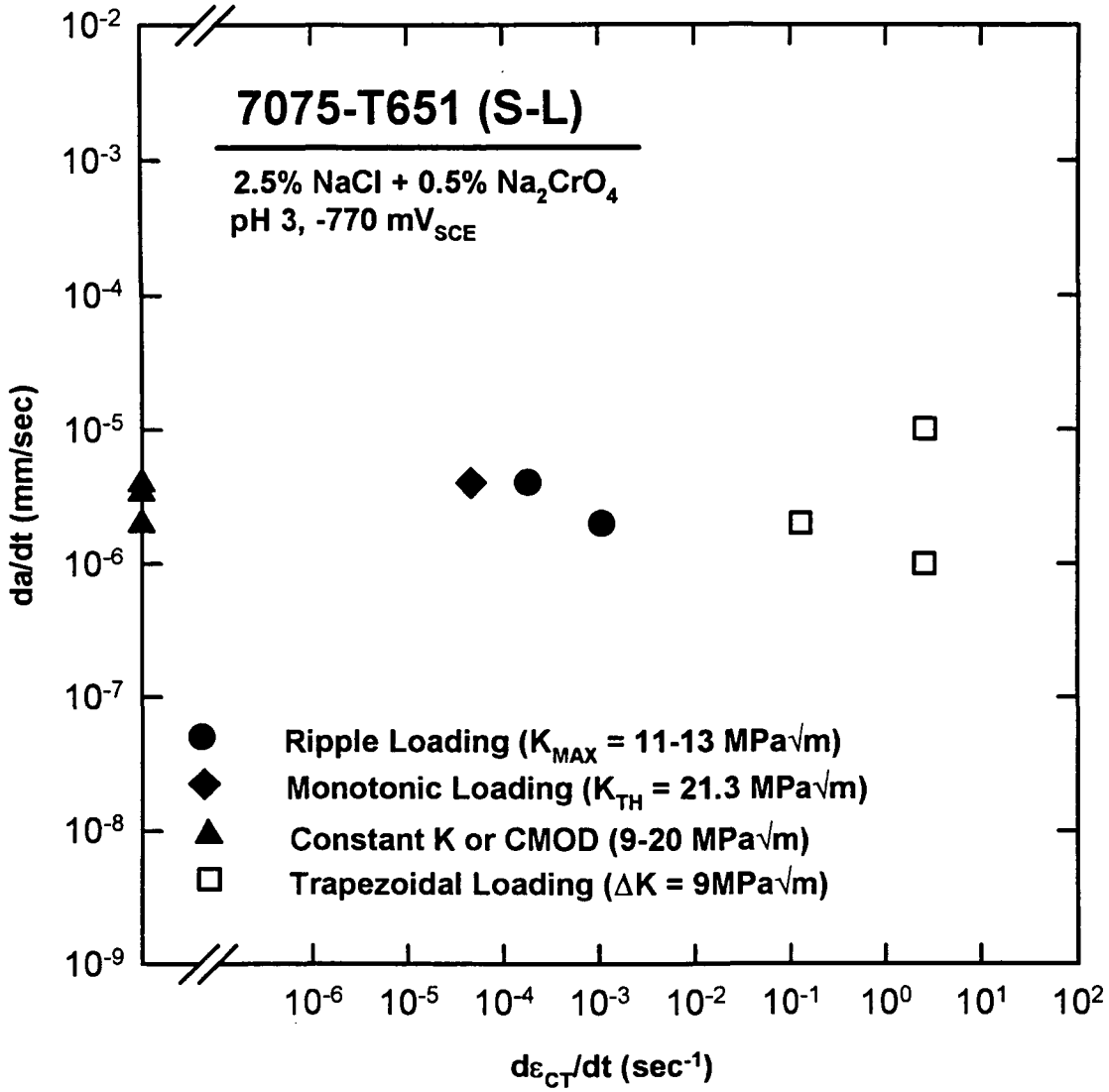

Fig. 4.4. Effect of strain rate on da/dt for 7075-T651(S-L)/NaCl.

hold time at constant K_{MAX}. Otherwise, hold time $d\epsilon_{CT}/dt$ is low and, as with static loading, depends only on da/dt and crack tip creep. If rise time $d\epsilon_{CT}/dt$ enhances da/dt for a portion of τ_H, then trapezoidal hold time da/dt should be enhanced for fast rise times. Short periods of high da/dt may not be detected if da/dt decays rapidly with time to lower da/dt attributed to low $d\epsilon_{CT}/dt$ from static loading during τ_H. Alternately, the amount of enhanced crack growth may be negligible when compared to Δa_H, where Δa_H is equal to the product of τ_H and da/dt_{SCC}.

The results in Fig. 4.4 indicate that da/dt is not strain rate-enhanced, from very low $d\epsilon_{CT}/dt$ for constant stress intensity and constant CMOD loading to $d\epsilon_{CT}/dt$ as high as 2 sec^{-1} during fast rise time trapezoidal loading. Crack tip strain rates for ripple loading are approximately 10 times faster than for monotonic loading, while trapezoidal loading $d\epsilon_{CT}/dt$ are over three orders of magnitude faster. Enhanced da/dt due to the applied CMOD rate for the single monotonic loading experiment in chloride was not detected. Near-K_{TH} da/dt was instead approximately 10^{-6} mm/sec and likely clouded by plasticity and temperature effects on DCPD, as discussed in Section 3.1.22. Monotonic loading at fast $d\epsilon_{CT}/dt$ results in the onset of mechanical cracking at K_{IC}, perhaps because slow step(s) in the HE sequence do not occur even if $d\epsilon_{CT}/dt$ yields high surface concentration of hydrogen. This problem is circumvented for the ripple loading case, but da/dt was still not enhanced.

A hypothesis for the effect of monotonic loading rate on hydrogen production and uptake is illustrated in Fig. 4.5. Crack tip strain versus time is

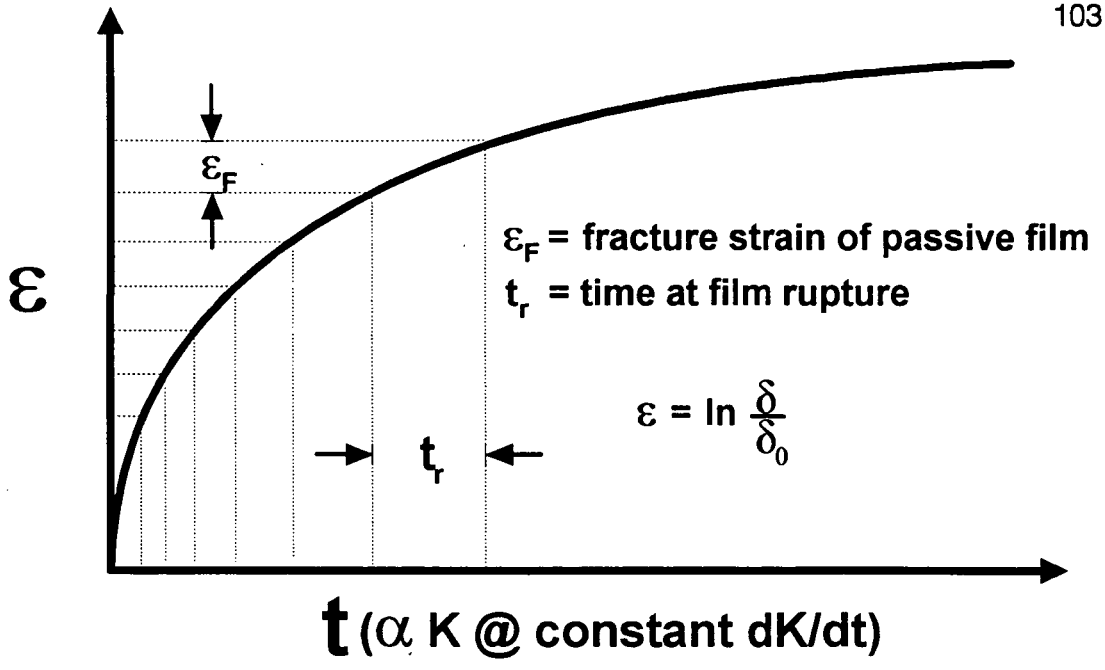

(a)

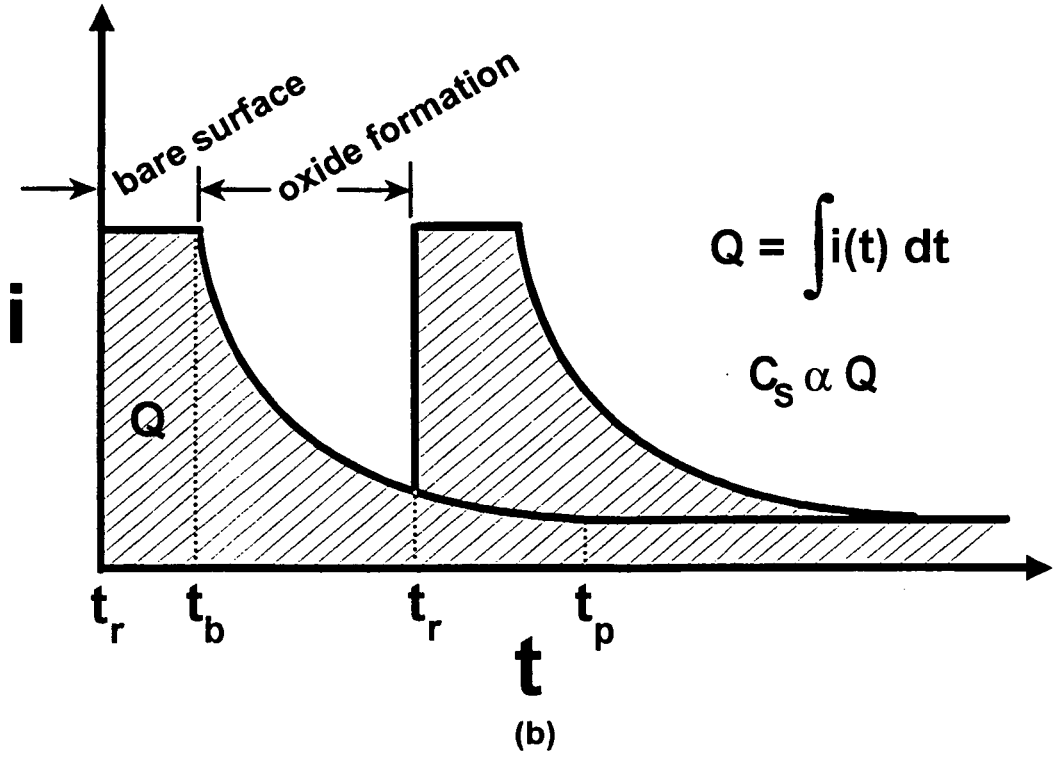

(b)

Fig. 4.5. Schematic showing effect of passive film rupture on Q and C_s.

shown in Fig. 4.5a for a stationary crack and constant dK/dt(Eq. 4.1). The fracture strain (ϵ_F) for the oxide is labeled in Fig. 4.5a, with the time between film rupture events (t_r) indicated along the ordinate. For monotonic loading at constant dK/dt monotonic, K is directly proportional to time.

Crack tip anodic repassivation kinetics for aluminum in aqueous chloride are represented by the anodic current density (i) versus time schematic in Fig. 4.5b. Crack tip oxide formation kinetics are assumed to consist of bare metal surface reaction for the period of time from t_r to the onset of oxide formation (t_b). An exponential decrease in anodic current density with respect to time due to oxide formation follows t_b, and anodic current density reaches steady state anodic charge transfer at the passivation time (t_p). The magnitudes of t_r, t_b, and t_p depend on metallurgical and environmental variables, and are uncertain for the crack tip region in the 7075/NaCl system. The total anodic charge (Q) passed during repassivation of the crack tip is the integral of anodic current density with respect to time. If Q is assumed to be an index of electrochemical activity at the crack tip, then the amount of atomic hydrogen adsorbed on the crack tip surface (C_s) should be proportional to Q.

Figure 4.6 illustrates the proposed dependence of da/dt on $d\epsilon_{CT}/dt$ for $d\epsilon_{CT}/dt$ from creep and da/dt dominated static loading to high strain rates where dynamic loading conditions govern $d\epsilon_{CT}/dt$. Hydrogen enhanced da/dt is expected when C_s is sufficient for HE. The inset schematic for low $d\epsilon_{CT}/dt$ shows mildly increasing da/dt with $d\epsilon_{CT}/dt$ below a threshold strain rate ($d\epsilon_{TH}/dt$) defined

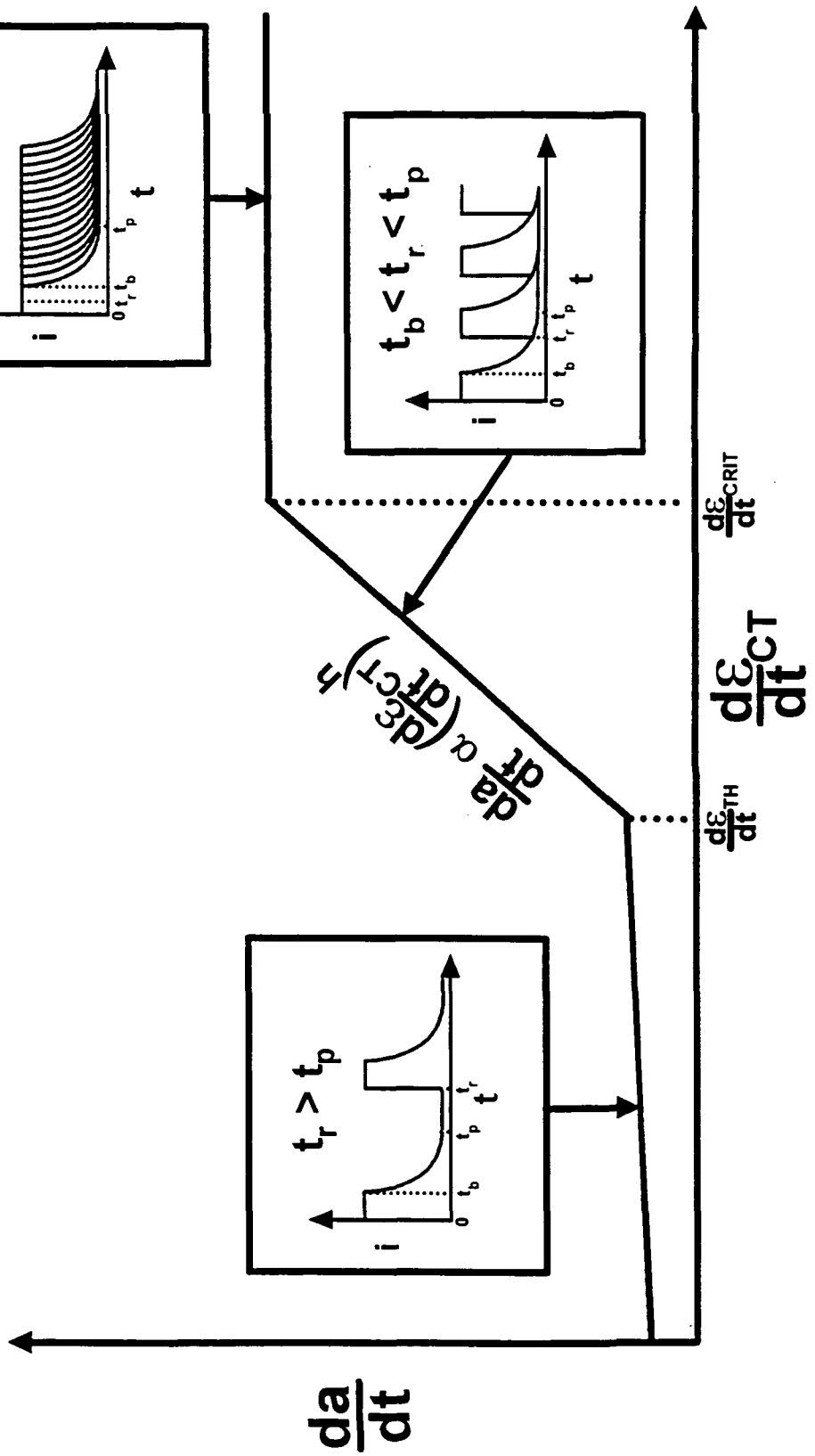

Fig. 4.6. Schematic illustrating effect of $d\varepsilon_{CT}/dt$ on da/dt.

by ϵ_F and t_p. For the constant K and CMOD experimental conditions, where film rupture is infrequent and $d\epsilon_{CT}/dt$ is controlled by crack tip creep and da/dt, $d\epsilon_{CT}/dt$ may be below $d\epsilon_{TH}/dt$ and accordingly da/dt is not rate-dependent.

When the time between film rupture events is less than t_p, film rupture should be sufficiently frequent to substantially increase Q and C_s, and to cause enhanced da/dt due to HE. More frequent film rupture should lead to strongly $d\epsilon_{CT}/dt$-dependent da/dt, as shown in Fig. 4.6 for intermediate $d\epsilon_{CT}/dt$. Ford argues that da/dt is proportional to $(d\epsilon_{CT}/dt)^h$ where h is a repassivation rate constant between 0.5 and 1. [56] Measurement of repassivation kinetics, specifically the exponential dependence of anodic current density decay with time during oxide film formation for 7075-T651 in an environment identical to the occluded crack chemistry, is required to quantitatively predict the dependence of da/dt on $d\epsilon_{CT}/dt$ for intermediate $d\epsilon_{CT}/dt$. No $d\epsilon_{CT}/dt$ dependent da/dt were observed for the range of monotonic and ripple loading $d\epsilon_{CT}/dt$ examined, as shown in Fig. 4.4.

A transition in da/dt versus $d\epsilon_{CT}/dt$ is predicted by this model at a critical crack tip strain rate ($d\epsilon_{CRIT}/dt$) dependent on ϵ_F and the repassivation kinetics of the alloy-environment system. If t_b is large relative to t_r then a sharp transition as indicated in Fig. 4.6 is predicted, equivalent to a continually bare crack tip for all strain rates above the critical value. A more gradual transition is predicted for t_b of zero, as t_r becomes much less than t_p. The slope of da/dt versus $d\epsilon_{CT}/dt$ approaches zero when t_r is sufficiently small to enable a continually bare crack tip;

frequent film rupture events occur and do not allow repassivation to occur. Electrochemical reactions at an oxide-free crack tip should provide near-maximum Q and C_s for HE. At this point C_s is no longer $d\epsilon_{CT}/dt$-dependent and da/dt is not $d\epsilon_{CT}/dt$-limited, at least from the surface reaction perspective.

The threshold and critical strain rates depend on ϵ_F and metal repassivation kinetics at the crack tip. Uncertainties in these parameters, along with the crack tip strain and strain rate singularities, preclude exact calculation of critical strain rates. Ford suggests $d\epsilon_{CRIT}/dt$ of 10^{-2} sec^{-1} for low alloy steels in high purity water at 288°C, based on a 0.1% fracture strain and a 0.1 sec t_b ($d\epsilon_{CRIT}/dt = \epsilon_F/t_b$; Fig. 4.6). [36,56] An estimate of $d\epsilon_{CRIT}/dt$ of 10^2 to 10 sec^{-1}, based on a 1 to 0.1% oxide fracture strain and 10^{-4} sec t_b, may be reasonable for 7075-T651 in room temperature aqueous chloride. [60] An assumed passive current density of approximately 10 $\mu A/cm^2$, leads to an estimated t_b of 10 sec. [60] Dividing the fracture strain by t_b yields an estimate for $d\epsilon_{TH}/dt$ of 10^{-3} to 10^{-4} sec^{-1}.

In contrast the results in Fig. 4.4 show da/dt independent of $d\epsilon_{CT}/dt$ for the range of $d\epsilon_{CT}/dt$ from less than 10^{-6} to 1. Constant K and CMOD $d\epsilon_{CT}/dt$ is assumed to be the lower $d\epsilon_{CT}/dt$ limit for detection of da/dt. Recall that da/dt_{SCC} is equivalent to da/dt for monotonic, ripple, and trapezoidal fatigue loading. If $d\epsilon_{CT}/dt$ for SCC is below $d\epsilon_{TH}/dt$ (Fig. 4.6) then, unless $d\epsilon_{CT}/dt$ for these latter three loading conditions were also below $d\epsilon_{TH}/dt$; $d\epsilon_{CT}/dt$ should exceed $d\epsilon_{TH}/dt$ and an increase in da/dt is expected. The failure to observe any change in da/dt with $d\epsilon_{CT}/dt$ highlights the speculative nature of estimating crack tip strain rates;

$d\epsilon_{CT}/dt$ for the loading conditions presented in Fig. 4.4 may be overestimated, or $d\epsilon_{TH}/dt$ may be higher based on electrochemical considerations. Alternately, $d\epsilon_{CT}/dt$ is above $d\epsilon_{TH}/dt$, but some other step in the HE process, such as time-dependent hydrogen accumulation in the process zone, limits da/dt. But, the ripple load experiment was designed to address this point, however, the expected effect of strain rate was not observed.

Two reasons are evident for the failure of low ΔK ripple loading to enhance da/dt for 7075-T651 (S-L) in chloride. Ripple loading may not increase strain rates at the crack tip, as otherwise predicted by continuum fracture mechanics with strain and strain rate singularities. Accordingly, and oxide rupture events reflect the high constant K_{MAX} only. Ripple loading strain rates are estimated from $\Delta\epsilon_P$ (see Eq. 4.6) extrapolated from results at ΔK levels between 6 and 10 MPa$\sqrt{m}$. At a ΔK of 0.7 MPa$\sqrt{m}$, Eq. 4.5 predicts a $\Delta\epsilon_P$ of approximately 10^{-5}, one hundred times less than the assumed 10^{-3} oxide fracture strain. Low surface strains, or the small cyclic process zone size of approximately 0.05 μm, may have been insufficient to activate slip for crack tip film rupture. Alternately, extrapolation of $\Delta\epsilon_P$ to the low ΔK is invalid.

Second, increased $d\epsilon_{CT}/dt$ for the ripple loading case may not have exceeded $d\epsilon_{TH}/dt$ and measured crack velocities represent $d\epsilon_{CT}/dt$-independent da/dt below $d\epsilon_{TH}/dt$. Ripple loading experiments, at higher frequencies to increase $d\epsilon_{CT}/dt$ without cyclic process zone damage, are necessary to test this hypothesis.

As a consequence of the failure of $d\epsilon_{CT}/dt$ to enhance da/dt, process zone

fatigue damage at the near-threshold ΔK of 0.7 MPa$\sqrt{m}$ caused EFCP by a competitive crack tip damage mechanism, independent of passive film rupture rate. Features on the ripple loading fracture surface, as revealed by SEM fractography (see Figs. 3.17 and 3.18), and da/dN values are similar to results of sinusoidal loading EFCP experiments, suggesting that the amplitude of the ripple load used to disturb the oxide at the crack tip may have caused cyclic process zone damage and EFCP. If da/dt at the ripple loading K_{MAX} of 11 to 13 MPa$\sqrt{m}$ was enhanced by the higher crack tip strain rates, then the crack velocity due to the high sustained K_{MAX} and local strain rates above 10^{-4} to 10^{-3} should have produced a da/dN_{SCC} much greater than near-threshold EFCP da/dN.

Da/dt during the hold portion of the trapezoidal waveform was not enhanced by utilizing fast rise times to K_{MAX} to impose crack tip strain rates of 10^{-1} to 2 sec^{-1}. The da/dt values for trapezoidal loading in Fig. 4.4 are derived from the mild hold time-dependence of EFCP da/dN under trapezoidal loading at ΔK of 9 MPa$\sqrt{m}$ (see Fig. 3.10). Da/dN_{CF} was assumed equivalent to EFCP da/dN at τ_H of 0.1 sec, with the increase in EFCP da/dN at higher τ_H attributed to da/dN_{SCC}. Da/dt_{SCC} at τ_H of 50, 20, and 5 sec, with variable rise time to K_{MAX} and hence strain rate, are presented in Fig. 4.4. These results provide no evidence to support the hypothesis that da/dt determined during hold time at K_{MAX} provides a more effective input to the linear superposition model, or the hypothesis that faster rise times, and hence strain rates, enhance hold time da/dt.

Da/dt is not enhanced by increasing crack tip strain rate due to rapid

monotonic loading rate, applied low amplitude ripple loading, or rapid rise time followed by static loading at K above K_{ISCC}. Uncertainties in modeling near crack tip strains and strain rates, determining the mechanical properties (viz, ductility) of the thin oxide film, with a potentially low defect density, and determining the repassivation kinetics for 7075-T651 in the unknown occluded crack tip environment, complicate application of the passive film rupture model and interpretation of the results in Fig. 4.4. [36] Passive film rupture may not be the rate limiting crack tip damage mechanism governing EAC of 7075-T651 in chloride, as indicated by the nil influence of $d\epsilon_{CT}/dt$ on da/dt.

4.2.3 Time Dependent EFCP da/dN

Figure 1.2 shows the wide range of EFCP da/dN frequency dependencies for 7000 series aluminum alloys in chloride. As discussed in Section 4.1.2, strongly frequency-dependent da/dN for 7075 below 0.001 Hz and 7079 below 1 Hz are equivalent to da/dN_{SCC} (Eq. 1.2). Linear superposition of da/dN_{CF} and da/dN_{SCC} may be successfully applied for some 7000-T6(S-L) series aluminum alloys in chloride environments because strongly frequency-dependent da/dN_{SCC} becomes vanishingly small relative to da/dN_{CF} at high frequencies, or because this SCC contribution is intrinsically small relative to da/dN_{CF} and da/dN_{MECH}. [4,8,17] (This summation is developed in Eq. 4.8.) The series operation of da/dN_{CF} and da/dN_{SCC} that linear superposition presumes is difficult to envision if SCC and EFCP involve different crack tip damage mechanisms and fracture paths. The more likely

interpretation is that da/dN_{CF} is mildly frequency and rise time dependent for 7075 in NaCl for the portion of the time-dependence in Fig. 1.2 where da/dN is not proportional to reciprocal f.

Significant environmental enhancement at frequencies where da/dN_{SCC} contributes little to da/dN_{CF} may be due to an EAC mechanism which is competitive with SCC. Austen and Walker proposed that the CF crack propagates by the fastest available mechanism for a given loading condition. [48] By this view, da/dN_{CF} as a function of frequency is related to the complex interplay between time-dependent solution mass transport processes, process zone hydrogen diffusion, and crack surface reaction rates. [3,34] The rate controlling step governs the form of mechanism-based modeling. [3,34] Models for EFCP da/dN have been developed which relate crack tip solution convection, diffusion in the process zone, hydride formation, or surface reaction rate to EFCP da/dN. [3,34]

4.2.31 Mechanism-Based Linear Superposition Modeling

Mechanism-based models for EFCP da/dN add da/dN_{CF} to the linear superposition model (Eq. 1.1), representing the synergism of the environment and cyclic loading conditions. Wei and coworkers suggested adding da/dN_{CF} that represents one or more fracture micromechanisms acting sequentially with da/dN_{SCC}. Adjusting the linear superposition model (Eq. 1.1), gives:

$$\frac{da}{dN} = \frac{da}{dN_{MECH}}(1-\phi) + \frac{da}{dN_{CF}}\phi + \frac{da}{dN_{SCC}} \qquad (4.8)$$

where da/dN_{CF} is a "pure" corrosion fatigue rate, from the synergism of

environmental and cyclic loading, and ϕ is the fractional area of crack that is undergoing pure corrosion fatigue. [8] For 7075-T651 and high strength steels in water vapor, ϕ correlates with the area fraction of fracture surfaces showing environmental cracking modes, with the balance $(1-\phi)$ being an inert environment fracture morphology. [34] Chemical models for da/dN_{CF} are then formulated from a surface reaction control perspective, with the fractional surface chemical reaction coverage of the crack tip defined as θ, directly proportional to ϕ. [34] For the S-L orientation of 7075-T651 in chloride, fast solution mass transport and surface reaction rates are assumed, and both θ and ϕ are considered to be one; da/dN_{CF} may instead depend on diffusion of hydrogen in the crack tip process zone, with the role of surface reactions restricted to establishing C_s. This view does not contradict a possible role of strain rate in establishing the steady state level of C_s.

Hydrogen embrittlement is attributed to enhanced cracking along grain boundaries and particle interfaces due to hydrogen accumulation at these segregation or trapping sites. [3] Hydrogen accumulation to other potential trapping sites such as dislocation cores and subgrain boundaries could also enhance crack propagation. Alternately, limited evidence of strain induced hydride formation during SCC of Al-Zn-Mg alloys has been reported, based on observed surface films on fracture specimens. [61] A necessary condition for both hydride formation and lattice HE is diffusion of hydrogen ahead of the crack tip.

The hypothesis is that for crack tip hydrogen environment embrittlement, diffusion and accumulation of hydrogen in the highly stressed crack tip process

zone controls EFCP da/dN. This perspective assumes that da/dN equals the extent of crack advance (Δx) per a number of load cycles ($N = f\Delta t$, where Δt is the time expired to produce N) which may be 1 or larger. Δx is governed by the ΔK-based mechanics of process zone fatigue damage. A critical crack growth rate, da/dN_{CRIT}, then corresponds to the value at which hydrogen diffusion is just sufficient to penetrate to a critical concentration over Δx in Δt. Assuming a per cycle crack advance ($N = 1$), Δt corresponds to the cycle period of a critical frequency (f_{CRIT}) below which sufficient hydrogen accumulation is attained over Δx. This relationship was formalized by Holroyd and others to predict the dependence of da/dN_{CRIT} on f_{CRIT}: [9,10]

$$\frac{da}{dN_{CRIT}} = \frac{2}{\sqrt{f_{CRIT}\, N}} \sqrt{D_H}\; erf^{-1} \left(1 - \frac{C_{CRIT}}{C_S} \right) \qquad \textbf{(4.9)}$$

D_H is the diffusivity of hydrogen in aluminum, be it grain boundary, lattice or dislocation transport-based. C_{CRIT} is the amount of hydrogen that must be accumulated for cracking at the deepest point of the fatigue damage distribution within the process zone, and C_S is the concentration of atomic hydrogen on the crack tip surface, in equilibrium with the occluded crack tip solution electrochemistry, as defined in Section 4.2.23.

Equation 4.9 predicts that da/dN_{CRIT} varies as $(f_{CRIT})^{-0.5}$, as would all da/dN-ΔK values above this level if simple parallel slope behavior is operative, as illustrated schematically in Figs. 4.7a and b. Figure 4.7b shows da/dN versus frequency at two ΔK levels, illustrating the frequency dependence predicted by Eq. 4.9 for a

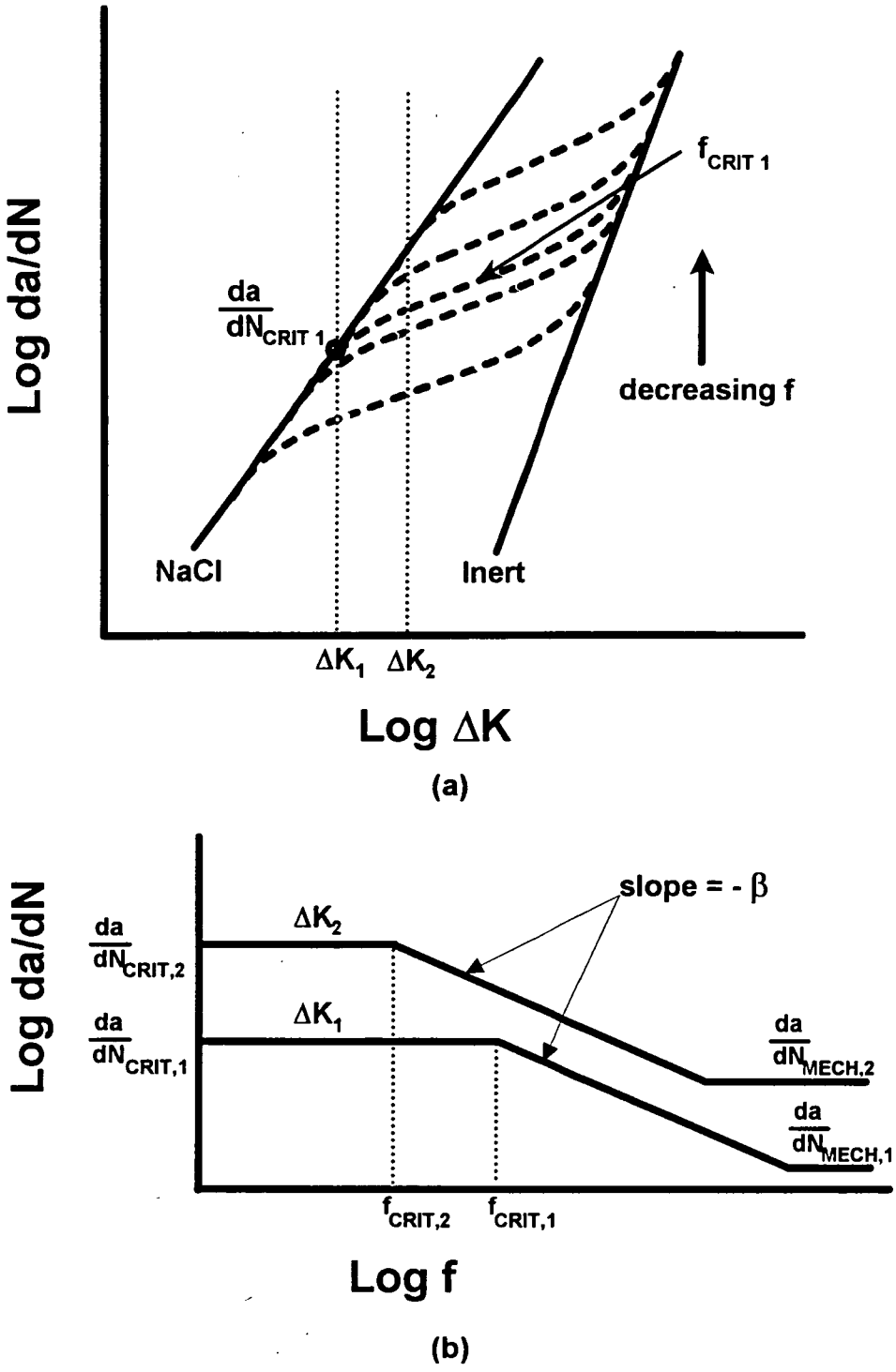

Fig. 4.7. Schematic EFCP da/dN vs. ΔK showing the frequency dependence of da/dN and the ΔK dependence of f_{CRIT} as well as da/dN_{CRIT}.

single alloy and environment at two constant ΔK levels. For constant ΔK and frequencies below f_{CRIT}, da/dN is equivalent to da/dN_{CRIT} and is time-cycle independent; sufficient time is available for hydrogen diffusion in the crack tip process zone. For frequencies above f_{CRIT} da/dN is rate-limited and is some proportion of da/dN_{CRIT}, due to either a decreased Δa due to a transition in fracture mode, or an increased ΔN. When insufficient time for hydrogen accumulation is available, da/dN is not environmentally enhanced and da/dN becomes equivalent to da/dN in an inert environment, independent of frequency.

4.2.32 Mechanistic Interpretation of Frequency Dependent EFCP da/dN

4.2.32A Critical Crack Growth Rate and Frequency

Literature values of environmental fatigue crack propagation da/dN, derived from ΔK-increasing test results at several constant ΔK levels for 7017-T651 (S-L) in seawater, are presented in Fig. 4.8a. [10] Two transitions in EFCP da/dN versus frequency for 7017 are shown for a ΔK level of 12 MPa√m, with frequency independent da/dN for frequencies below 1 Hz and above 30 Hz. Midrange frequency da/dN show a modest time-cycle dependence, as da/dN decreases from da/dN at low frequencies to a lesser environmental enhancement of da/dN at higher frequencies. EFCP da/dN for a ΔK level of 15 MPa√m exhibits frequency independence at frequencies above 10 Hz for the range of frequencies examined.

Green and Knott observed a single transition from time-cycle-independent da/dN to time-cycle-dependent da/dN for 7475-T651 (S-L) in chromate inhibited

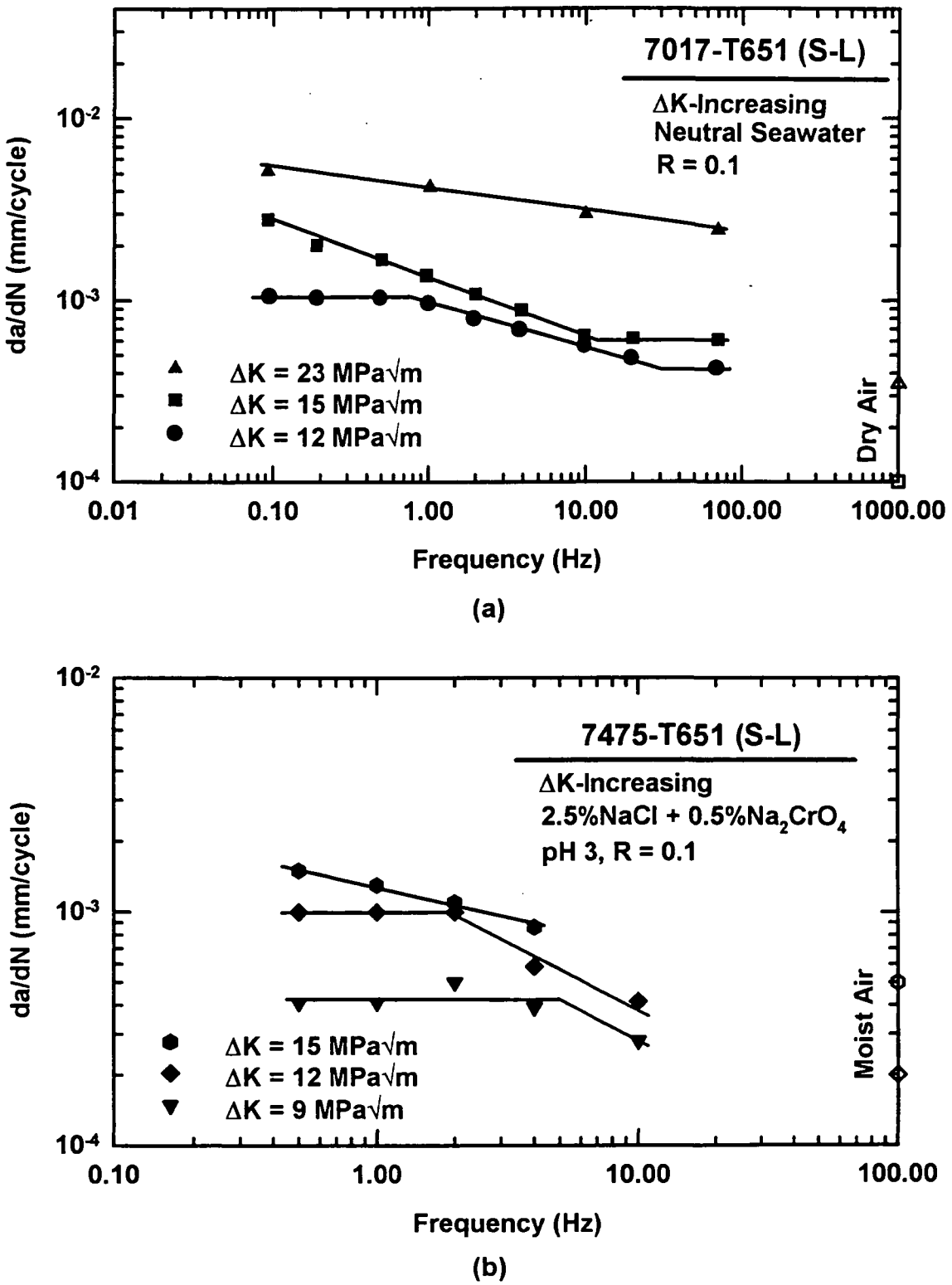

Fig. 4.8. Effect of frequency on EFCP da/dN for (a) 7017 and (b) 7475 in NaCl.

acidified chloride. [9] Figure 4.8b shows da/dN for constant ΔK da/dN versus frequency derived from ΔK-increasing results. These results show time-cycle-figure independent da/dN at low frequencies, with da/dN becoming rate limited for frequencies above f_{CRIT}. Critical frequencies and fatigue crack growth rates from analyses of ΔK-increasing da/dN versus frequency, shown in Fig. 4.8b for ΔK levels of 9 and 12 MPa√m, are equivalent to the da/dN_{CRIT} versus f_{CRIT} behavior for 7475 determined from constant frequency da/dN versus ΔK by the method illustrated in Fig. 4.7a. For the following analyses f_{CRIT} is defined as the frequency where time cycle-independent da/dN transitions to time-cycle-dependent da/dN with increasing frequency.

Considering the f_{CRIT} observed for EFCP da/dN in Fig. 4.8a and b for moderate ΔK levels, an alternate interpretation of the da/dN verses frequency data for sinusoidal loading of 7075-T651(S-L) in chloride at two constant ΔK levels(see Fig. 3.7) is presented in Fig. 4.9. For ΔK of 9 MPa√m, and at frequencies below 1 Hz, da/dN is nearly constant with the exception of the single low growth rate value measured at 0.01 Hz in neutral uninhibited NaCl. This result may be due to the failure of convective mixing to flush corrosion product from the crack tip and associated reduction in da/dN due corrosion product induced closure. The remaining low ΔK da/dN results are time-cycle-independent for frequencies below 1 Hz. Figure 4.9 shows a milder time-cycle-dependent EFCP da/dN for 7075-T651(S-L) in chloride at ΔK of 15 MPa√m for frequencies of 0.01 to 20 Hz and a possible f_{CRIT} of approximately 0.1 Hz. (Clearly the data are insufficient to prove this

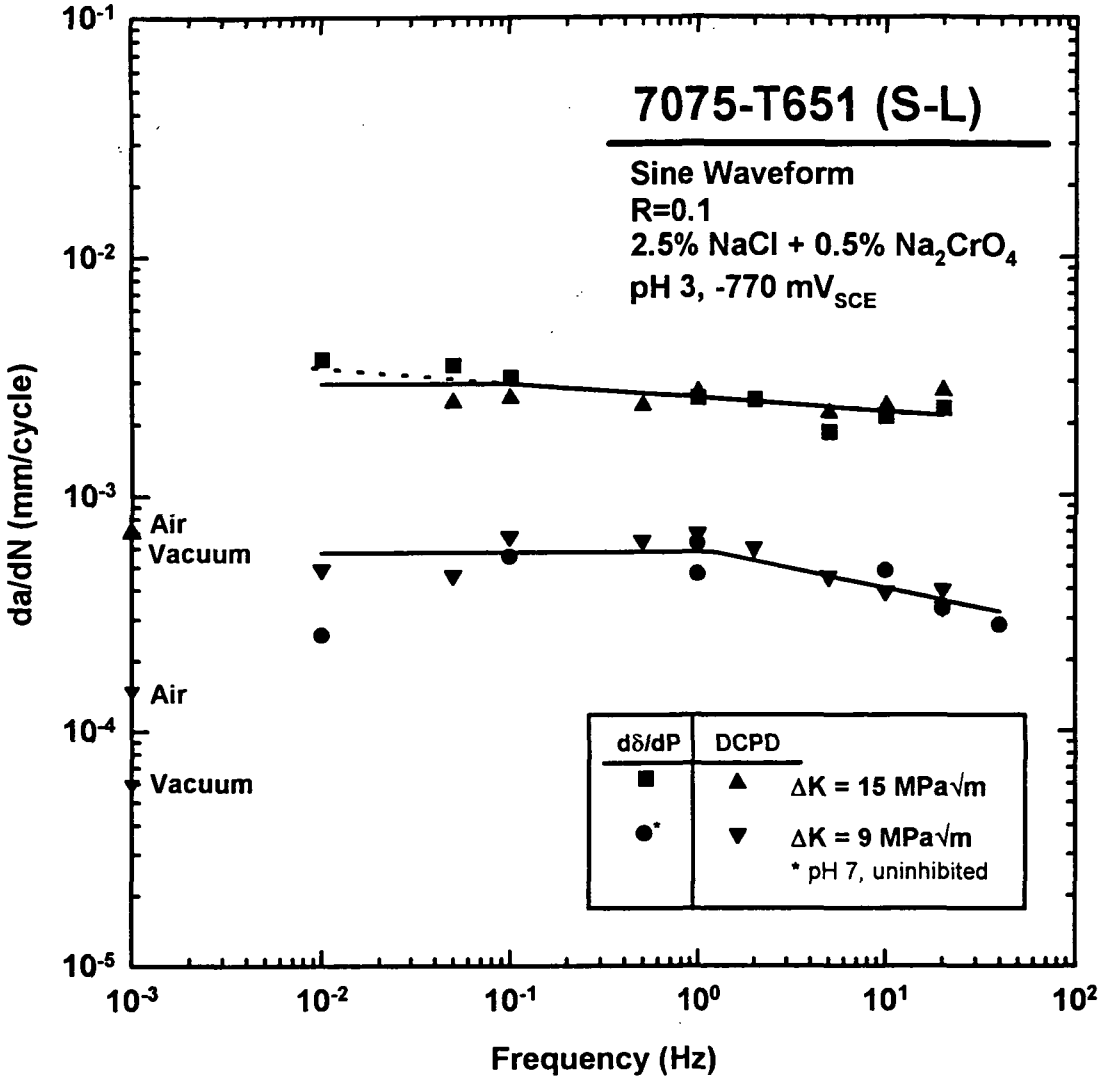

Fig. 4.9. Alternate interpretation of the effect of frequency on EFCP da/dN for constant ΔK loading.

behavior, as illustrated by the dashed line.)

Figure 4.10 shows da/dN_{CRIT} versus f_{CRIT} determined from constant ΔK experiments for 7075-T651(S-L) (●), compared with da/dN_{CRIT} derived by two methods from constant frequency ΔK-increasing results for 7017-T651(S-L)(□, ■) and 7475-T651(S-L)(▲, △). [9,10] The open symbols for 7017(□) and 7475(△) represent da/dN_{CRIT} from constant frequency da/dN versus ΔK-increasing results with da/dN_{CRIT} defined where da/dN becomes rate-limited (Fig. 4.7a). The closed symbols (▲, ■) were determined from the da/dN versus frequency results for 7017 and 7475 presented in Fig 4.8a and b, respectively.[5]

4.2.32B HE Modeling of da/dN_{CRIT} dependence on f_{CRIT}

The view that EFCP da/dN is diffusion-limited when insufficient time is available for hydrogen accumulation to exceed C_{CRIT} over Δx in the process zone implies that da/dN_{CRIT} is proportional to $(f_{CRIT})^{-0.5}$. [9,10] Assuming da/dN_{CRIT} dependent on $(f_{CRIT})^{-0.5}$, a line with slope of -0.5 was fit to the results in Fig. 4.10. These data agree closely with the predicted $(f_{CRIT})^{-0.5}$ dependency for da/dN_{CRIT}.

Since D_H, C_{CRIT}, and C_s are not known, Eq. 4.9 was adjusted to incorporate these factors into a single parameter, γ_{CRIT}:

---

[5] Open and closed symbol results are derived from the same da/dN versus ΔK-increasing data and demonstrate the utility of using constant ΔK to determine da/dN_{CRIT} versus f_{CRIT} behavior. That is, as Fig. 4.10 shows, da/dN_{CRIT} versus f_{CRIT} are equivalent within the scatter of da/dN measurements when the same data are analyzed either at constant frequency or constant ΔK.

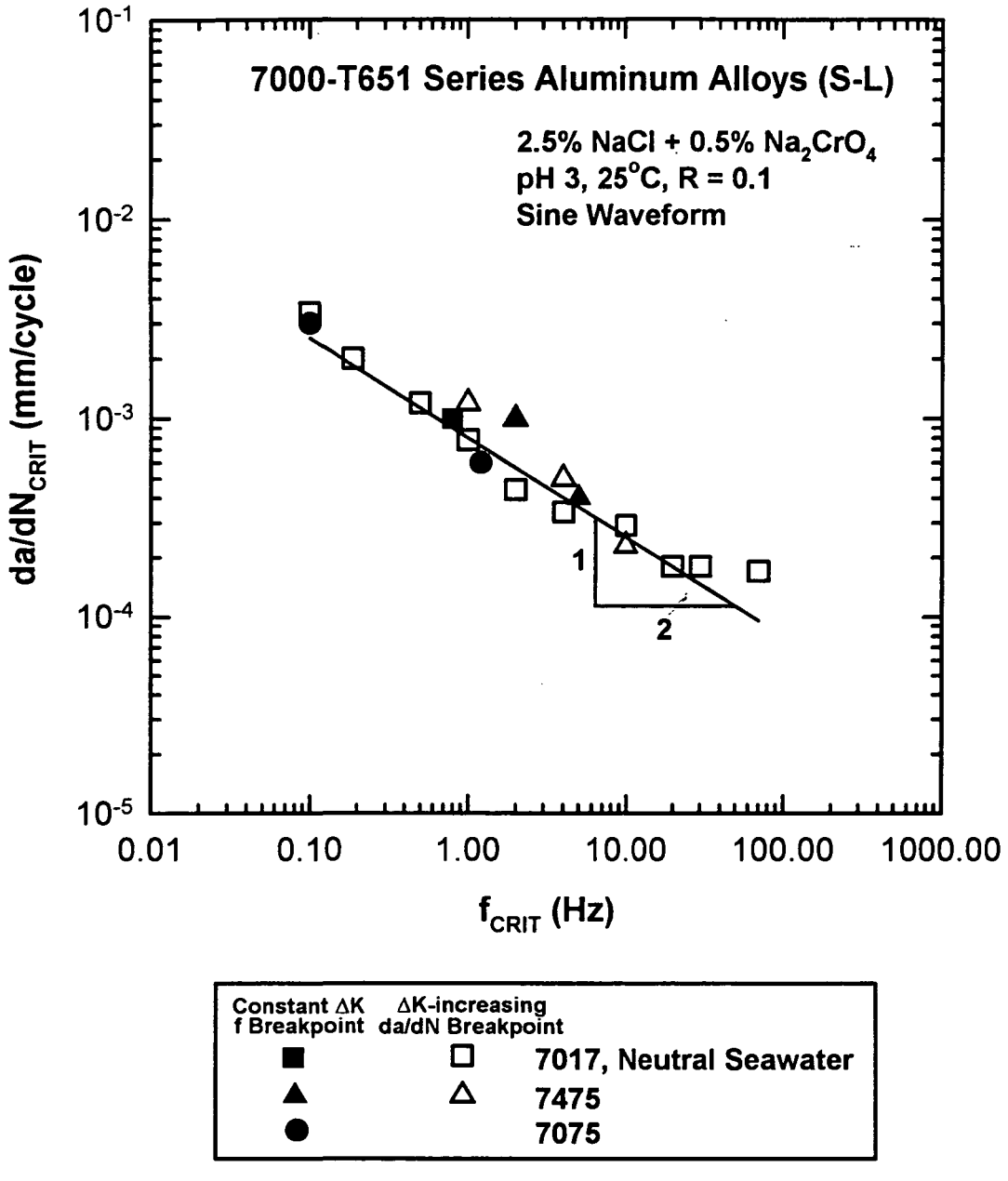

Fig. 4.10. Effect of f_{CRIT} on da/dN_{CRIT} for peak-aged 7000-T651(S-L) series aluminum alloys in chloride. Data for 7017 and 7475 were obtained from the literature. [9,10]

$$\frac{da}{dN_{CRIT}} = \frac{\gamma_{CRIT}}{\sqrt{f_{CRIT}}} \qquad (4.10)$$

where:

$$\gamma_{CRIT} = 2\sqrt{D_H}\,erf^{-1}\left(1 - \frac{C_{CRIT}}{C_S}\right) \qquad (4.11)$$

The least squares line fit to da/dN_{CRIT} versus f_{CRIT} in Fig. 4.10 yielded a γ_{CRIT} of 9.2 x 10^{-7}(±6%) m/√sec.

Figure 4.11 shows C_{CRIT}/C_S for a given D_H using Eq. 4.11 and for a range of γ_{CRIT} from 8.7 to 9.8 x 10^{-7} m/√sec, defined by the ±6% error in the γ_{CRIT} for the line in Fig. 4.10. D_H depends on metallurgical factors as well as the dominant diffusion mechanism, while C_{CRIT} is governed by the embrittlement mechanism and HE susceptibility of the alloy. C_S may depend not only on $d\epsilon_{CT}/dt$ as discussed in Section 4.2.23, but also on environmental and metallurgical variables. As shown in Fig. 4.11, numerous combinations of D_H, C_{CRIT}, and C_S satisfy γ_{CRIT}. Notably, γ_{CRIT} has been shown to change with fracture mode. [10]

4.2.32C Determination of D_H and C_{CRIT}/C_S

Limited results from hydrogen permeation studies of 7075-T651 at 25°C report a D_H of 2 x 10^{-9}cm^2/sec. [10,25] More extensive data for D_H for pure aluminum at 25°C vary from 10^{-7} to 10^{-12}cm^2/sec with the wide range for D_H values attributed to alloy impurities, porosity, grain boundaries, surface contamination, and oxide thickness. [62,63] The efforts to determine D_H for pure aluminum utilized

high temperature (350 to 600°C) desorption studies that yield a calculated ambient temperature D_H by extrapolating high temperature data via an Arrhenius relationship between temperature and D_H.

Figure 4.11 clearly shows that a wide range of possible D_H and C_{CRIT}/C_S, applied to Eq. 4.9 for the onset of rate-limited behavior, produce results that are physically reasonable. D_H could be as small as 5×10^{-10} for C_{CRIT}/C_S of 0.001 and as fast as $10^{-6}cm^2/sec$ for C_{CRIT}/C_S approaching unity. If a D_H of $2 \times 10^{-9}cm^2/sec$ is assumed then C_{CRIT}/C_S is approximately 0.2. However, further measurements of the magnitudes of D_H and C_{CRIT}/C_S are necessary, due to the wide range of D_H and C_{CRIT}/C_S combinations that predict da/dN_{CRIT} versus f_{CRIT} for 7000 series aluminum alloys in chloride.

Holroyd and Hardie estimated D_H and C_{CRIT}/C_S using the two transitions in the frequency dependency for 7017-T651 (S-L), associated fracture mode transitions, and several assumptions regarding C_{CRIT} levels necessary for intergranular and transgranular hydrogen assisted cracking. [10] Holroyd and Hardie noted the transition from time-cycle-dependent to high frequency time-cycle-independent da/dN corresponded to a change in fracture mode from transgranular brittle to transgranular ductile. [10] For frequencies below this transition, more time is available for hydrogen accumulation to C_{CRIT} over Δx and da/dN increases with increasing cycle time (decreasing frequency). Holroyd and Hardie assumed a Δx equivalent to per cycle crack advance and a C_{CRIT}/C_S much less than one ($1-C_{CRIT}/C_S \approx 1$) for transgranular brittle fracture. [10] If the transition from

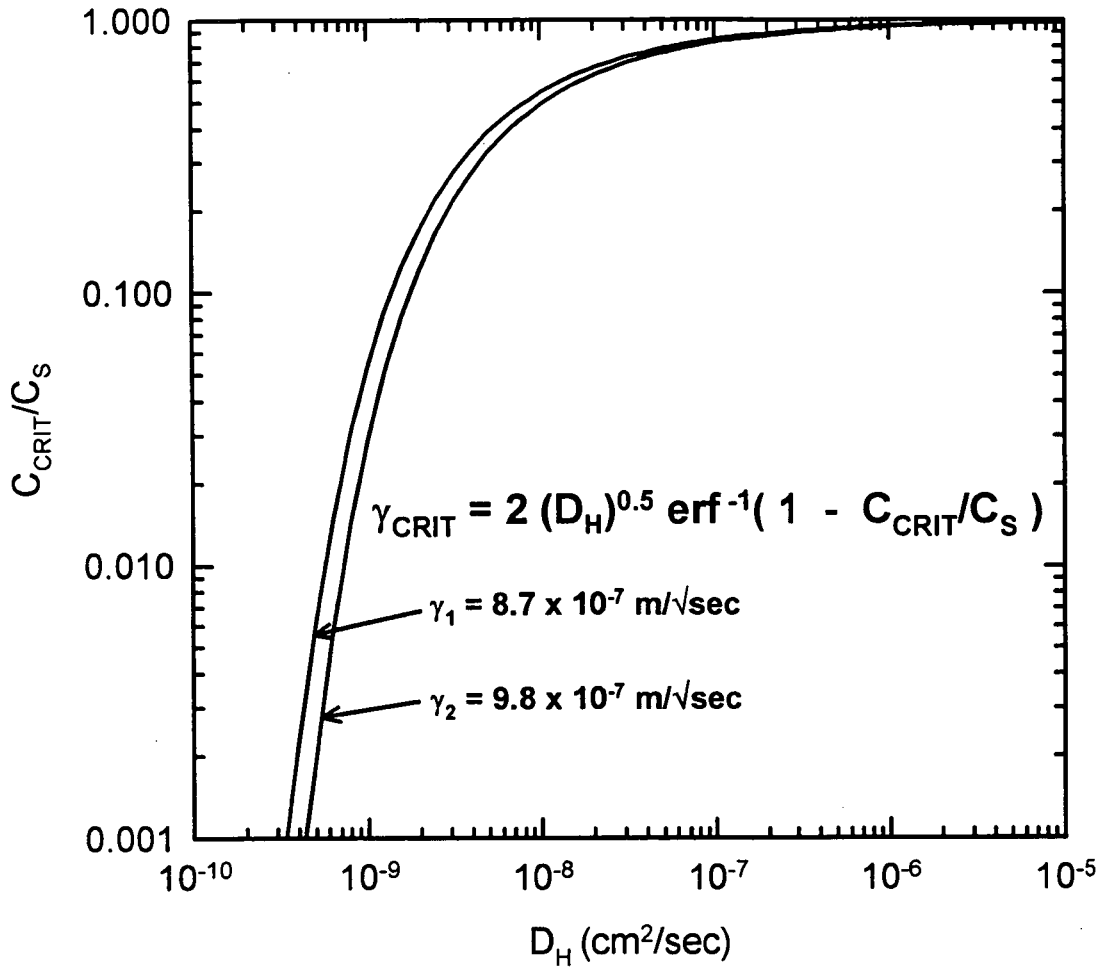

Fig. 4.11. D_H versus C_{CRIT}/C_S for constant γ_{CRIT} determined for 7000 series aluminum alloys in chloride.

transgranular brittle to intergranular at even lower frequencies and higher da/dN is attributed to a much higher C_{CRIT}, and a higher Δx for intergranular fracture versus transgranular fracture, then it seems reasonable to assume as a first approximation that C_{CRIT}/C_S for transgranular brittle fracture is very small ($\gamma_{CRIT} = 4\sqrt{D_H}$). Using a data-derived γ_{CRIT} of 2.2×10^{-6} m/$\sqrt{}$sec, determined with Eq. 4.11 for 7017-T651 and the transition from transgranular brittle to transgranular ductile as well as the assumption of negligible C_{CRIT}/C_S, a D_H of 3.1×10^{-9} cm^2/sec is calculated. [10]

This D_H of 3.1×10^{-9} cm^2/sec is within the wide range of D_H reported for pure aluminum and compares favorably to a D_H value of 2×10^{-9} cm^2/sec, based on hydrogen permeation studies of 7075-T651. [25] Green and Knott chose a D_H of 5×10^{-9} cm^2/sec based on the assumption that, due to dominance of fast grain boundary diffusion, D_H would be higher than that for bulk diffusion and calculated a C_{CRIT}/C_S of 0.14. [9] These calculations are based on a slightly higher γ_{CRIT} calculated for 7475 than the γ_{CRIT} determined for the results for 7017, 7075, and 7475 presented in Fig. 4.11.

If constant D_H of 3.1×10^{-9} cm^2/sec calculated by Holroyd and Hardie for 7017 is assumed for 7075, 7475, and 7017, then Fig. 4.11 shows a C_{CRIT}/C_S of 0.3 for the transition from time-cycle independent to time-cycle-dependent da/dN with decreasing frequency. This C_{CRIT}/C_S is equivalent to the mean value of 0.26 reported by Holroyd and Hardie for the transition from transgranular brittle to transgranular ductile for 7017-T651 in seawater.

If C_{CRIT}/C_S is assumed to be at least an order of magnitude smaller for transgranular brittle fracture than for intergranular fracture, then C_{CRIT}/C_S is at least less than 0.1. This assumption and measured γ_{CRIT} for the high frequency transgranular brittle to transgranular ductile fracture mode transition for 7017 seem to provide a reasonable means for calculating D_H. While this logic is compelling, two potential sources of error are evident in the simplifying assumptions that only C_{CRIT} and Δx change between fracture modes. First, equal D_H is assumed for diffusion of hydrogen to intergranular and transgranular fracture process sites. Since D_H varies with diffusion path, and grain boundary diffusion is believed to be an order of magnitude or more faster than bulk lattice diffusion of hydrogen, some other mechanism for hydrogen diffusion from grain boundaries to the transgranular process zone must be invoked so that hydrogen transport from the grain boundary to the grain interior is not rate-limited by bulk diffusion.

Perhaps grain boundary or subgrain/ dislocation pipeline hydrogen diffusion is important even for transgranular EFCP in these alloys. It has been suggested that dislocation transport could increase D_H to a value as high as 5×10^{-7} cm^2/sec, [19] however, the notion of dislocation transport of hydrogen in aluminum alloys has been challenged. [20] Hydrogen transport may be by enhanced pipe diffusion through the crack tip dislocation structure produced by cyclic plastic deformation. This structure could be deformation mode and alloy-dependent.

Alternately, an intersubgranular fracture path identical to that observed for 7075-T651 at low f and ΔK for this study, rather than fracture along high angle

boundaries as reported for 7017, could have a D_H nearly equivalent to that required for transgranular fracture. That is, a decrease in the distance required for bulk diffusion from the tens of microns that separate the intergranular and transgranular crack tip to the few microns separating the transgranular and intersubgranular makes the notion of nearly equal D_H for intersubgranular and transgranular more reasonable since there is less distance where diffusion may be limited by slower bulk diffusion between the intersubgranular and transgranular crack tips. Reducing the distance of lattice diffusion may decrease the effect of the potential rate limiting step of lattice hydrogen diffusion from grain boundaries to the transgranular process zone. Actual D_H may be nearly equal for hydrogen diffusion to the transgranular process zone and intersubgranular process zone in this case, due to the proximity of low angle subgrain boundaries and transgranular fracture sites. As these arguments suggest, D_H could vary with fracture path, deformation mode, microstructure, and alloy composition. The excellent correlation between alloys in Fig. 4.10 may be due to concurrent changes in C_{CRIT}/C_S which offset variability in D_H.

The concentration of hydrogen at the crack tip surface could be fracture path and alloy-dependent. Compositional differences between fracture paths such as high angle grain boundaries and the grain interior could affect crack tip chemistry and C_S. Segregation of elements, as well as the particles populating grain boundaries and subgrain boundaries, may have a significant effect on C_S. For example, Zn or Mg could be present in varying amounts in precipitates, lattice solid

solution, or segregated to grain boundaries. These elements could preferentially dissolve to enrich the crack solution in cations which in turn could increase C_s by affecting the ratio between the absorption and desorption rate constants involved in H production on the crack surface.[6] [16] A surface film enriched in a segregant could also affect such a change. Magnesium segregation to grain boundaries in 7000 series aluminum alloys has been documented. [21,22,64] Cation effects on electrochemistry, and surface film effects on hydrogen entry, have not been substantiated by either crack chemistry measurements or permeation experiments with aluminum alloys. Alternately, Analybechyi demonstrated that C_s in aluminum is enhanced by solid solution elements such as Li; [65] the role of Mg in this regard is unclear.

The necessary concentration of hydrogen to promote HE over Δx is likely to change with fracture mode, whether it be intergranular, intersubgranular, lattice decohesion or enhanced void nucleation at particles. C_{CRIT} depends on the structure and local strength of the sites of hydrogen-enhanced fatigue damage. It is unknown how this concentration varies with alloy microstructure and cyclic deformation processes.

The results in Fig. 4.10 clearly implicate accumulation of hydrogen ahead of the crack tip as a rate controlling step for EFCP da/dN, however, these results must be interpreted carefully because of the complex dependence of D_H, C_{CRIT}, and C_s on numerous metallurgical, compositional, and environmental parameters.

---

[6] Personal communication with John R. Scully.

While it appears these 7000 series aluminum alloys show a similar dependence of da/dN_{CRIT} on f_{CRIT}, fracture morphology correlations to f_{CRIT} and da/dN_{CRIT} are not consistent among the alloys. The slope of rate-limited EFCP da/dN versus frequency varies widely among 7000-T651(S-L) series aluminum alloys in chloride as indicated in Fig. 1.2 and discussed in 4.2.32E.

4.2.32D Fractographic Evidence for Hydrogen Embrittlement

Figure 4.12 is a schematic showing the results of fractographic evaluation of the fracture surfaces for variable frequency EFCP experiments conducted for the S-L orientation of 7017-T651, 7075-T651, and 7475-T651 in chloride environments. For 7017 and 7475, fracture mode transitions were correlated with a change in frequency dependence, while the conclusions for 7075 are based on the less rigorous evaluation of EFCP fractography presented in Section 3.3.3.

Fracture surfaces for 7075/NaCl, produced at a moderate ΔK of 9 MPa$\sqrt{m}$ and identified as predominantly intersubgranular (eg., Fig. 3.19), are strikingly similar to the fractograph presented as characteristic of intergranular corrosion fatigue for 7017 in seawater. [10] The similar faceted appearance, and the facet size on the order of the subgrain size (10 μm) rather than grain size in the S-plane (200 μm in the T direction and 500 μm in the L direction for 7075) leads to the conclusion that low frequency EFCP occurs by intersubgranular cracking for 7075-T651 in chloride. Similar facets of order 10 μm populate the "intergranular" fracture surface reported for 7017. Since the product forms (hot-rolled plate), thicknesses

Alloy*	f-independent da/dN	rate-limited da/dN	f-independent da/dN
7017-T651	IG	TGB	TGD
7075-T651	ISG	TGB	ND**
7475-T651	TGB	TGD	ND**

* S-L Orientation
** Not Determined

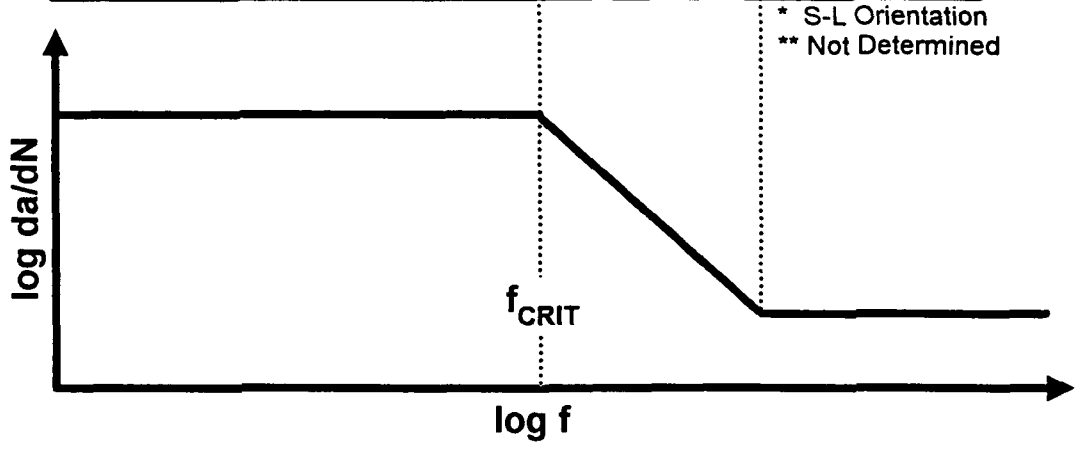

Fracture Modes

IG:	Intergranular
ISG:	Intersubgranular
TGB:	Transgranular Brittle
TGD:	Transgranular Ductile

Fig. 4.12. Observed fracture modes as a function of frequency for moderate ΔK levels (9-15 MPa$\sqrt{m}$) for 7000 series aluminum alloys in NaCl. [9,10]

(58 mm for 7075 and 40 mm for 7017), and compositions of 7075 and 7017 studied were similar, and since both were unrecrystallized, they are likely to have similar microstructures. If the fracture mode for 7017 is instead intersubgranular for low frequency time-cycle-independent da/dN, then 7075 and 7017 show identical fracture modes for frequencies below f_{CRIT}.

As noted in Section 3.3.3, fracture surfaces for 7075-T651 (S-L) in chloride at a constant ΔK level of 9 MPa$\sqrt{m}$ contained no brittle striations for frequencies below 1 Hz. This frequency was independently identified as f_{CRIT} in Fig. 4.9 from da/dN versus frequency results at ΔK of 9 MPa$\sqrt{m}$. The fractograph characteristic of flat transgranular fracture in 7017 is similar to the 7075 fracture surfaces produced by loading at greater than 1 Hz and a ΔK of 9 MPa$\sqrt{m}$. Holroyd and Hardie noted that the 7017 fracture mode transitioned fully within 200 μm of crack growth as ΔK increased continuously for a constant frequency and load range. For 7075-T651(S-L) in this study, the transition appears more gradual and intersubgranular fracture is observed below an apparent f_{CRIT}. The more gradual transition may be associated with the less dramatic change in slope of da/dN versus frequency for 7075 versus the stronger frequency-dependence for rate limited da/dN for 7017 (Fig. 1.2). Ductile fracture modes were not observed on any EFCP surfaces for 7075-T651 (S-L) at moderate ΔK levels of 9 to 15 MPa$\sqrt{m}$. Also, da/dN in chloride never decreased to moist air values as happened for 7017. These limited fractographic comparisons indicate that the transition from frequency-independent intersubgranular to frequency dependent transgranular fatigue is

similar for 7017-T651(S-L) and 7075-T651(S-L) in chloride.

In contrast EFCP for 7475-T651 (S-L) in chromate inhibited acidified chloride was reported to progress by a transgranular brittle mode for time-cycle-independent da/dN and by a transgranular ductile mode for time-cycle-dependent da/dN. A transition from transgranular brittle to transgranular ductile was observed for 7017, however, transgranular brittle EFCP was time-cycle-dependent and transgranular ductile cracking was time-cycle-independent. Furthermore γ_{CRIT} for the transgranular brittle to ductile transition in 7017 is three times lower than that for the intergranular to transgranular brittle transition. It would seem that the same fracture mode transition in 7475 should have an equivalent γ_{CRIT} as the transgranular brittle to transgranular ductile transition in 7017. However, γ_{CRIT} for the transgranular brittle to ductile transition for 7475 as shown in Fig. 4.10 is equivalent to γ_{CRIT} for the intersubgranular to transgranular brittle transition for 7075 and 7017. This observation implies that γ_{CRIT} should be defined for transitions in da/dN versus frequency behavior and not fracture mode transitions.

The single low magnification fractograph presented to characterize transgranular brittle fracture for 7475 [9] makes comparison of 7475 fracture surfaces with those for 7075 and 7017 difficult. Slight compositional and microstructural differences between 7475-T651 and the 7075-T651 studied may cause the quite different appearance of time dependent fracture modes, since time-cycle-independent EFCP da/dN are nearly equivalent and the aqueous environments were identical.

The apparent dominance of single fracture modes on the fracture surfaces for each region of the da/dN frequency dependence indicates that the fracture modes are competitive as opposed to operating in parallel. Concurrent cracking with da/dN proportional to the percentage of the fracture surface (ϕ from Eq. 4.8) undergoing environmentally enhanced cracking, was shown for steels and 7075-T651 in less aggressive water vapor. [34] However, since each region of da/dN-frequency behavior had a single dominant fracture mode, it is more likely that the da/dN versus frequency behavior schematically shown in Fig. 4.12 is due to the operation of competitive fracture modes. That is, the crack path that offers the least resistance to cracking, and is favored by process zone mechanics and environment conditions, will be operative. By this view, frequency-dependent da/dN increases with cycle time at moderate frequencies as time increases to allow greater depth of hydrogen penetration. It is proposed that for this type of time-dependent EFCP, Δa (equivalent to Δx) desired by ΔK cannot be achieved by diffusion. Frequency-independent da/dN at low frequency appears to be intersubgranular fracture dependent on process zone size (ΔK) and is not limited by the kinetics of environmental damage given sufficient cycle time (low enough frequency) to accumulate C_{CRIT} over Δx. In this case, Δx cannot exceed the maximum value allowed by environment and process zone mechanics.

4.2.32E Variability in Rate-limited EFCP da/dN

The schematic in Fig. 4.7 of EFCP da/dN versus ΔK for constant

frequencies shows the parallel slope behavior for da/dN above da/dN_{CRIT} that is expected due to hydrogen kinetics governing time-dependent da/dN. By this notion of time-cycle-dependent da/dN, hydrogen diffusion is the rate limiting step and a slope of -0.5 is expected for da/dN versus frequency above f_{CRIT}. However, the wide range of frequency dependencies shown for time-cycle-dependent da/dN in Figs. 1.2 and 4.13, for 7000 series aluminum alloys in chloride, indicates that the behavior is more complex than represented in Figs. 4.7a and b. If the time-cycle-dependence of da/dN becomes stronger with increasing ΔK, then a trend of increasing slope with ΔK, that may vary with alloy-environment system, is expected in Fig. 4.13. In contrast, no consistent trend in da/dN slope is seen for the three ΔK levels shown in Fig. 4.13. Some combination of many possibly rate-limiting processes involved in EFCP evidently controls time-cycle-dependent EFCP da/dN above f_{CRIT}, with the data in Fig. 4.13 indicating the governing rate-limiting reaction changes with ΔK level.

Since variability in rate-limited EFCP da/dN has been suggested previously based on alloy compositional variations [16,21,22], the magnesium to zinc wt pct ratio and wt pct copper are given in the legend for the four alloys shown in Fig. 4.13. No trend in the time-dependent EFCP, based on these alloy composition differences, is evident. For example, equivalent da/dN versus frequency behavior is observed for low copper 7017 and high copper 7475. Different behavior is indicated for 7075 and 7475, with the only composition difference being lower iron and silicon for higher purity 7475. This analysis does not indicate an effect of

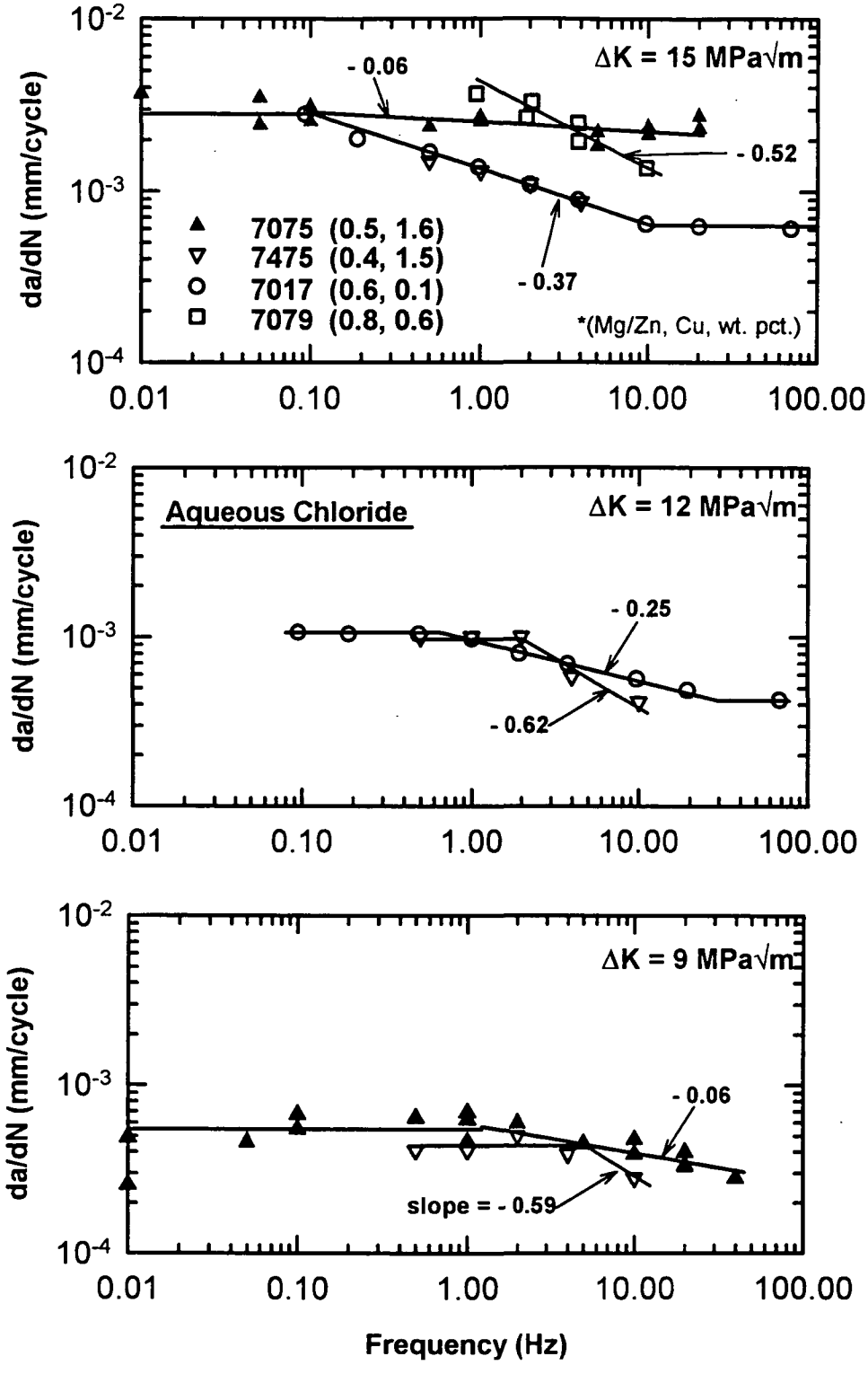

Fig. 4.13. Effect of alloy composition (wt pct Mg/Zn, Cu) and ΔK on EFCP da/dN versus frequency behavior for peak-aged 7000 series aluminum alloys in aqueous chloride. [4,9,10]

magnesium to zinc wt pct ratio, or wt pct copper, on time-dependent EFCP for 7075, 7475, and 7017.

4.2.32F Summary of Mechanistic Interpretation of Frequency Dependent EFCP da/dN

Rate-limited HE is implicated by an analysis of da/dN_{CRIT} versus f_{CRIT} for 7075/NaCl, strengthened by the significant body of evidence implicating HE of aluminum alloys in chloride. Neither fractographic inconsistencies nor the variability in the frequency dependence of rate-limited da/dN preclude the mechanism for EFCP from being hydrogen assisted. These observations indicate that the sequence of reactions that feeds the HE mechanism is multi-featured and complex, and that hydrogen diffusion may enhance EAC in many ways, dependent not only on the alloy-environment system, but also on loading parameters such as ΔK.

4.2.4 Rise Time Dependence

The wide variety of fatigue waveforms studied provides the opportunity to analyze the effect of loading waveform on EFCP da/dN, for example the effect of hold time at K_{MAX} (Section 3.2.4) and rise time from K_{MIN} to K_{MAX}(Section 3.2.5). Figure 3.12 shows that EFCP da/dN depends on $t_R^{-0.1}$ for a wide range of sinusoidal, symmetric and asymmetric triangle, and trapezoidal waveforms for the S-L orientation of 7075-T651 in aqueous chloride. However, the definition of t_R pertinent to EFCP damage must be considered carefully. Specifically, should t_R be

defined as time to reach maximum load, as in Fig. 3.12, or should it be defined as the time from minimum load to first unloading? This question cannot be answered from sinusoidal, triangular, or sawtooth waveform EFCP da/dN since unloading commences immediately upon attainment of K_{MAX} for these similar waveforms.

EFCP da/dN versus cycle time is shown in Fig. 4.14 for trapezoidal loading of 7075-T651(S-L) in chloride, with time defined as time from K_{MIN} to the onset of K_{MAX} (t_R) or from K_{MIN} to first unloading ($t_U = t_R + \tau_H$). The thick solid and dashed lines represent the results from sinusoidal, triangular, and sawtooth waveform da/dN versus t_R shown in Fig. 3.12. Limited trapezoidal loading data show a much stronger dependence of da/dN on t_R than t_U for both ΔK levels. The lower ΔK level of 9 MPa$\sqrt{m}$ is mildly t_U-dependent, while results for a ΔK of 15 MPa$\sqrt{m}$ show a nil effect of t_U on da/dN. Slight changes in da/dN with t_U are due to the mild effect of τ_H on da/dN shown in Fig. 3.10.

The slight dependency of trapezoidal EFCP da/dN on t_U, as opposed to the stronger t_R-dependent da/dN, evident for not only trapezoidal but also sinusoidal, sawtooth, and triangle waveforms; implicates a rise time effect on EFCP. Perhaps hydrogen transport is enhanced during loading by dislocations emitted from the crack tip. Speculatively, the amount of hydrogen transported by dislocations in unit time could depend on the velocity of dislocations in the process zone. As loading rate decreases, the proportion of dislocations with velocity sufficiently slow to drag hydrogen from the surface level (C_s) to trap sites in the process zone would increase. More hydrogen transport per unit time with slower rise times

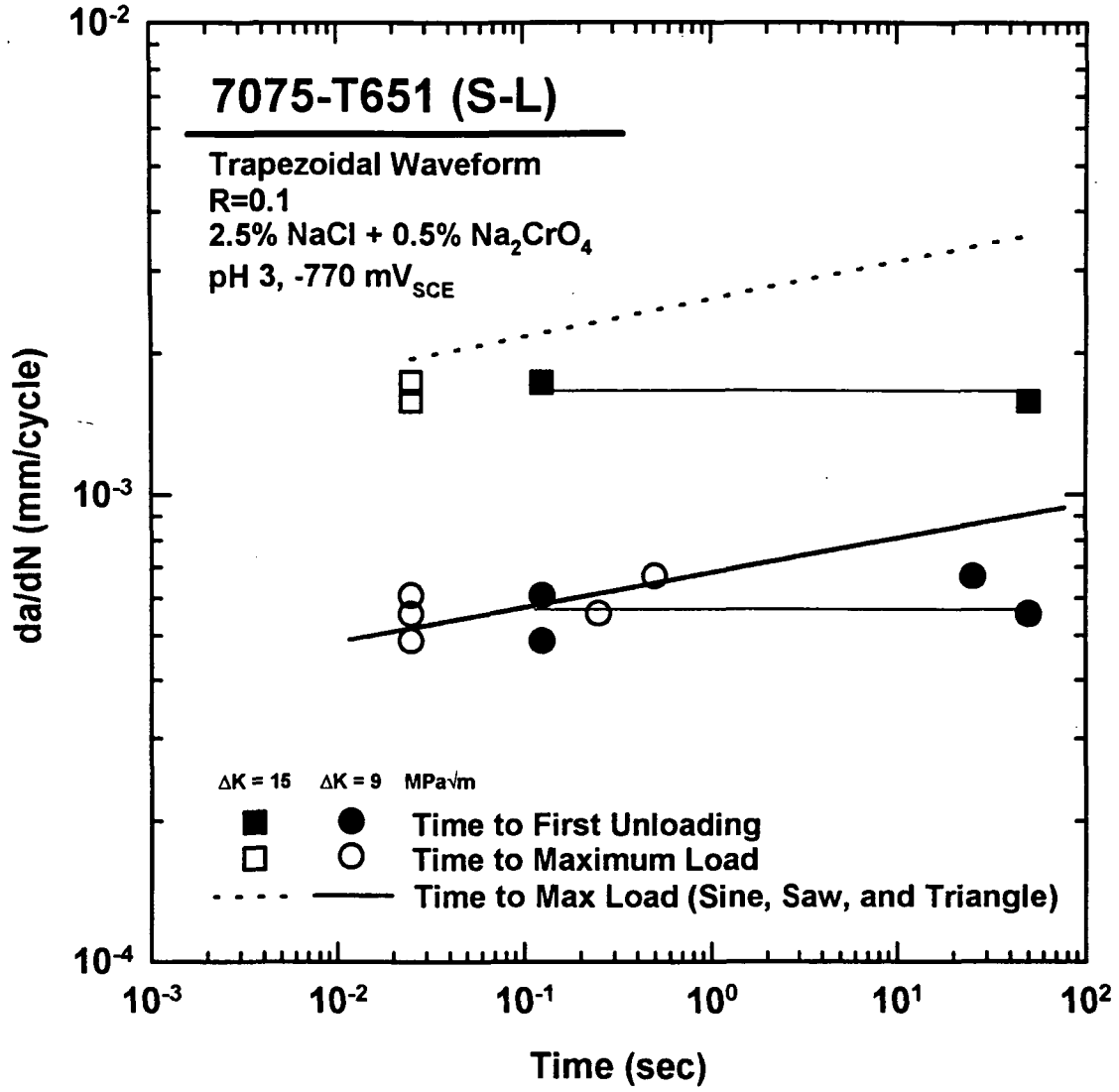

Fig. 4.14. Comparison of EFCP da/dN dependencies on rise time, based on time to maximum or time to first unloading, for 7075-T651(S-L) in NaCl.

produces da/dN proportional to t_R^m. A more general interpretation is that the rate-determining step in the complex hydrogen production and uptake reaction sequence is t_R-dependent.

Alternately, the weak dependence of t_R on da/dN shown in Figs. 3.12 and 4.14 is due to low crack tip strain rates below $d\epsilon_{TH}/dt$. A mild dependence of crack velocity on $d\epsilon_{CT}/dt$ is shown in the schematic in Fig. 4.6 for $d\epsilon_{CT}/dt$ below $d\epsilon_{TH}/dt$. For the range of rise times shown in Fig. 3.5 and a ΔK of 9 MPa$\sqrt{m}$ a $d\epsilon_{CT}/dt$ of 10^{-3} to 1 sec^{-1} is estimated using Eq. 4.5. This $d\epsilon_{CT}/dt$ is greater than the $d\epsilon_{TH}/dt$ of 10^{-4} to 10^{-3} sec^{-1} estimated from approximate values for fracture strain and repassivation kinetics. Since $d\epsilon_{CT}/dt$ is greater than predicted $d\epsilon_{TH}/dt$, a strong (h of 0.5 to 1) dependence of da/dt on $d\epsilon_{CT}/dt$ is expected. In contrast a mild dependence is observed.(For constant ΔK, $d\epsilon_{CT}/dt$ is inversely proportional to t_R.) It is difficult to establish this hypothesis due to the uncertainty of $d\epsilon_{CT}/dt$ and $d\epsilon_{TH}/dt$ estimates, as discussed previously.

The weak frequency dependency shown in Fig. 3.7 for ΔK levels of 9 and 15 MPa$\sqrt{m}$ is equivalent to the mild $t_R^{0.1}$ dependency observed for EFCP in 7075-T651(S-L) in chloride for sinusoidal and symmetric triangle waveforms. Consideration of sawtooth and trapezoidal da/dN indicates that t_R is a more general parameter than frequency for assessing time-dependent EFCP da/dN. Since the time-cycle-dependence of EFCP da/dN has been discussed in terms of the symmetric sinusoidal waveforms, and t_R in this case is inversely proportional to frequency, little else could be gained from analyses of sinusoidal loading da/dN

based on t_R.

4.3 Implications for Life Prediction Modeling

Considering time-cycle-dependent EFCP in the 7000 series alloys represented in Fig. 4.13, the mild frequency dependence for 7075 is an upper bound on more strongly f-dependent growth in 7017 and 7475. This behavior is amplified in Fig. 4.15, a plot of the trend line from Fig. 3.5 with literature data for peak aged 7017 (S-L). [10] Comparison with EFCP results for 7475 in chloride at 0.1 Hz (the lowest f reported for 7475/NaCl) gives an identical result. [9]

From an engineering perspective, EFCP for 7000 series aluminum alloys in chloride could be assumed to be orientation independent and equivalent to the upper bounds shown in Figs. 4.13 and 4.15. Any rate-limited behavior would extend component life, for example by as much as a factor of six for 7017-T651 and 7475-T651 (S-L) at a ΔK level of 15 MPa$\sqrt{m}$. However, the variability in frequency-dependent da/dN among alloys, and likely between environments, is not understood sufficiently to predict *a priori* whether beneficial rate-limited behavior can be expected. The upper bound for EFCP da/dN in Fig. 4.13 corresponds to frequency independent da/dN_{CRIT} or the locus of all da/dN_{CRIT}-ΔK values. A conservative approach using da/dN_{CRIT}, for frequencies above where da/dN_{SCC} becomes negligible, coupled with linear superposition below this frequency, is warranted for damage-tolerant life prediction for 7000 series aluminum alloys in aggressive chloride environments.

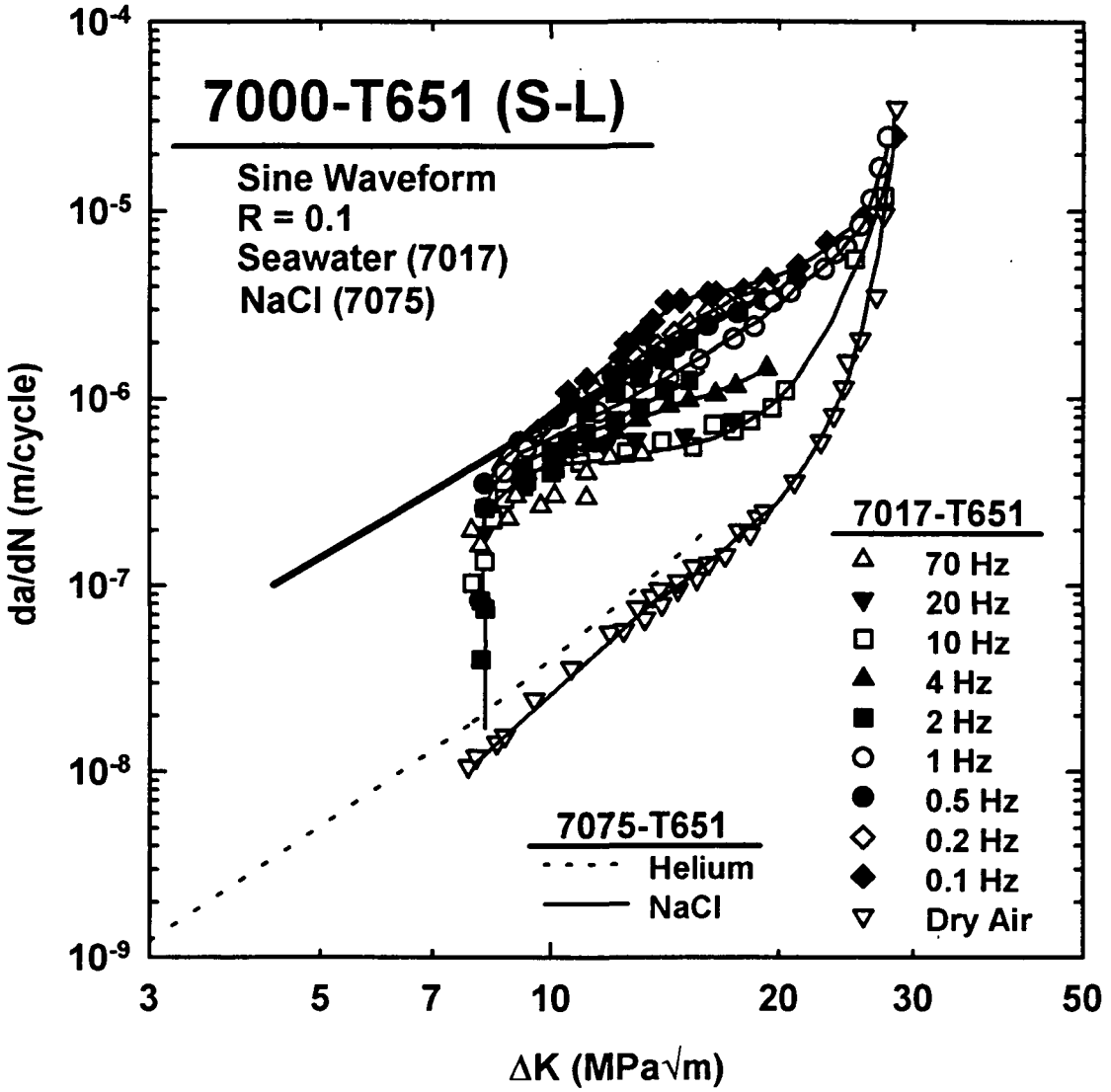

Fig. 4.15. Effect of ΔK on da/dN for peak-aged 7075 and 7017 in aqueous chloride showing upper bound, frequency-independent EFCP.

4.4 Conclusions

1. Linear superposition may be used to predict EFCP da/dN in the 7075-T651(S-L)/NaCl system for corrosion fatigue waveforms having K levels in excess of K_{ISCC} for more than 1000 seconds.

2. Plastic strain range, derived from crack tip displacement measurements for 7075-T651(S-L) in air, coupled with rise time from K_{MIN} to K_{MAX}, provides and estimate of $d\epsilon_{CT}/dt$ for fatigue loading.

3. Alternate methods for establishing da/dt, based on enhanced $d\epsilon_{CT}/dt$, do not provide a means of enabling linear superposition modeling of EFCP da/dN in 7075-T651(S-L)/NaCl.

4. Environment assisted crack velocity for 7075-T651(S-L) in aqueous chloride is not enhanced for crack tip strain rates from 2×10^{-5} to 2 sec^{-1}, imposed by monotonic, ripple, and trapezoidal loading conditions.

5. Passive film rupture may not be the rate limiting crack tip damage mechanism governing EAC of 7075-T651 in chloride, as indicated by the nil influence of $d\epsilon_{CT}/dt$ on da/dt.

6. EFCP da/dN for 7075-T651(S-L) in chloride transitions from time-cycle-independent to time-cycle-dependent da/dN at a critical crack growth rate and frequency. Above f_{CRIT}, shorter cycle periods provide less time for diffusion and accumulation of embrittling hydrogen in the process zone, and da/dN becomes time-cycle dependent.

7. Da/dN_{CRIT} depends on the square root of f_{CRIT} through a proportionality constant γ_{CRIT}. This dependence supports hydrogen embrittlement governed EFCP. The diffusivity of hydrogen in aluminum, the critical concentration of hydrogen in the process zone for embrittlement, and the concentration of hydrogen at the crack tip surface are incorporated into γ_{CRIT}. The complex dependencies of D_H, C_{CRIT}, and C_S on metallurgical, compositional, and environmental parameters cannot be determined from the results of this study.

8. Fractographic comparisons indicate that the transition from frequency-independent intersubgranular to frequency-dependent transgranular (brittle) fatigue is similar for 7017-T651(S-L) and 7075-T651(S-L) in chloride. Fracture modes for the S-L orientations of 7475-T651 and 7075-T651 differ, despite nearly equivalent time-cycle dependent EFCP da/dN.

9. EFCP of 7000-T651(S-L) series aluminum alloys in aqueous chloride is

governed by competitive fracture modes. The crack path that offers the least resistance to cracking, and is favored by process zone mechanics and environment conditions, is operative. For time-dependent EFCP, Δa is limited by the time available for hydrogen diffusion and accumulation in the process zone, producing an decrease in da/dN with decreasing cycle time.

10. A combination of many rate-limiting processes involved in EFCP of 7000-T651(S-L) series aluminum alloys in chloride evidently controls time-cycle-dependent EFCP da/dN above f_{CRIT}.

11. Results from asymmetric triangle loading and trapezoidal loading of 7075-T651(S-L) in chloride indicate that loading time from K_{MIN} to K_{MAX} is a more general parameter than frequency for analyzing time-dependent EFCP da/dN.

12. A conservative approach using da/dN_{CRIT}, for frequencies above where da/dN_{SCC} becomes negligible, coupled with linear superposition below this frequency, is warranted for damage-tolerant life prediction for 7000 series aluminum alloys in aggressive chloride environments.

CHAPTER 5. CONCLUSIONS

Conclusions - Chapter 3. Results

1. Da/dt_{scc} values are consistent with K-independent cracking above a K_{iscc} of 5 to 10 MPa$\sqrt{m}$. However, da/dt_{scc} ranges from 0.3 to 4.4 x 10^{-9} m/sec and is slower than literature results.

2. Primarily intersubgranular fracture at low stress intensity, with an increasing area fraction of overload fracture similar to mechanical overload in air and transgranular steps at stress intensities approaching K_{IC}, is observed for SCC of 7075-T651(S-L) in an acidified chromate inhibited chloride environment under constant CMOD or constant stress intensity loading. High angle boundary cracking was not a prominent feature for SCC for 7075-T651(S-L) in this study.

3. Imposed constant crack mouth opening displacement rate does not accelerate environmentally enhanced da/dt above da/dt_{scc}.

4. Da/dt is not enhanced by high frequency-low amplitude cyclic loading, designed to increase crack tip strain rate, in conjunction with a high sustained stress intensity.

5. SEM fractography of the 5 Hz and 30 Hz ripple loading fracture surfaces shows corrosion fatigue features. No intersubgranular cracking indicative of SCC or low frequency corrosion fatigue is observed.

6. Fatigue crack propagation rates for 7075-T651(S-L) in chromate inhibited, acidified NaCl solution are enhanced five to ten-fold over rates in moist air and are over an order of magnitude faster compared to cracking in helium.

7. Results from a single constant ΔK experiment (9 MPa$\sqrt{m}$), and comparison with literature results for the S-L and L-T orientations, indicate that EFCP da/dN are identical for acidified chromate inhibited and neutral uninhibited environments.

8. EFCP da/dN for 7075-T651(S-L) in NaCl shows a weak time-cycle frequency dependence above 0.001 Hz. Above 0.001 Hz, EFCP da/dN is proportional to $f^{-\beta}$ where β approximately equals 0.1.

9. Corrosion fatigue is predominantly intersubgranular for low frequencies and ΔK levels (below 0.1 Hz for ΔK of 9 MPa$\sqrt{m}$) for the S-L orientation of 7075-T651 in NaCl, with regions of transgranular fracture in the form of brittle striations, and steps between flat areas of intersubgranular fracture. Higher frequencies and ΔK levels showed primarily a transgranular fracture

morphology.

10. For 7075-T651 in the S-L orientation, results from corrosion fatigue experiments at two constant stress intensities indicate a very small effect of hold-time for the loading and unloading rates and times tested.

11. EFCP da/dN is proportional to t_R^m for a wide range of rise times, where m is approximately 0.1 for both symmetric and asymmetric loading waveforms for 7075-T651(S-L) in acidified chromate inhibited NaCl.

12. The NaCl environmental effect on time-cycle-dependent fatigue crack growth is identical for the S-L and L-T orientations of peak aged 7075, suggesting a minimal involvement of anisotropic high angle grain boundaries.

13. Compliance estimations of $K_{CLOSURE}$ and comparison with DCPD results for EFCP of 7075-T651 in NaCl indicate a negligible effect of time-dependent crack closure on frequency and rise time dependencies of da/dN for ΔK of 9 and 15 MPa$\sqrt{m}$. Intrinsic effects of stress ratio on da/dN in chloride were inseparable from the contributions of time-dependent closure.

Conclusions - Chapter 4. Discussion

1. Linear superposition may be used to predict EFCP da/dN in the 7075-T651(S-L)/NaCl system for corrosion fatigue waveforms having K levels in excess of K_{ISCC} for more than 1000 seconds.

2. Plastic strain range, derived from crack tip displacement measurements for 7075-T651(S-L) in air, coupled with rise time from K_{MIN} to K_{MAX}, provides and estimate of $d\epsilon_{CT}/dt$ for fatigue loading.

3. Alternate methods for establishing da/dt, based on enhanced $d\epsilon_{CT}/dt$, do not provide a means of enabling linear superposition modeling of EFCP da/dN in 7075-T651(S-L)/NaCl.

4. Environment assisted crack velocity for 7075-T651(S-L) in aqueous chloride is not enhanced for crack tip strain rates from 2×10^{-5} to 2 sec^{-1}, imposed by monotonic, ripple, and trapezoidal loading conditions.

5. Passive film rupture may not be the rate limiting crack tip damage mechanism governing EAC of 7075-T651 in chloride, as indicated by the nil influence of $d\epsilon_{CT}/dt$ on da/dt.

6. EFCP da/dN for 7075-T651(S-L) in chloride transitions from time-cycle-independent to time-cycle-dependent da/dN at a critical crack growth rate and frequency. Above f_{CRIT}, shorter cycle periods provide less time for diffusion and accumulation of embrittling hydrogen in the process zone, and da/dN becomes time-cycle dependent.

7. Da/dN_{CRIT} depends on the square root of f_{CRIT} through a proportionality constant γ_{CRIT}. This dependence supports hydrogen embrittlement governed EFCP. The diffusivity of hydrogen in aluminum, the critical concentration of hydrogen in the process zone for embrittlement, and the concentration of hydrogen at the crack tip surface are incorporated into γ_{CRIT}. The complex dependencies of D_H, C_{CRIT}, and C_S on metallurgical, compositional, and environmental parameters cannot be determined from the results of this study.

8. Fractographic comparisons indicate that the transition from frequency-independent intersubgranular to frequency-dependent transgranular (brittle) fatigue is similar for 7017-T651(S-L) and 7075-T651(S-L) in chloride. Fracture modes for the S-L orientations of 7475-T651 and 7075-T651 differ, despite nearly equivalent time-cycle dependent EFCP da/dN.

9. EFCP of 7000-T651(S-L) series aluminum alloys in aqueous chloride is

governed by competitive fracture modes. The crack path that offers the least resistance to cracking, and is favored by process zone mechanics and environment conditions, is operative. For time-dependent EFCP, Δa is limited by the time available for hydrogen diffusion and accumulation in the process zone, producing an decrease in da/dN with decreasing cycle time.

10. A combination of many rate-limiting processes involved in EFCP of 7000-T651(S-L) series aluminum alloys in chloride evidently controls time-cycle-dependent EFCP da/dN above f_{CRIT}.

11. Results from asymmetric triangle loading and trapezoidal loading of 7075-T651(S-L) in chloride indicate that loading time from K_{MIN} to K_{MAX} is a more general parameter than frequency for analyzing time-dependent EFCP da/dN.

12. A conservative approach using da/dN_{CRIT}, for frequencies above where da/dN_{SCC} becomes negligible, coupled with linear superposition below this frequency, is warranted for damage-tolerant life prediction for 7000 series aluminum alloys in aggressive chloride environments.

CHAPTER 6. REFERENCES

1. E. Richey III, A.W. Wilson, J.M. Pope, and R.P. Gangloff, "Computer Modeling the Fatigue Crack Growth Rate Behavior of Metals in Corrosive Environments", NASA Contractor Report 194982, NASA, Washington, DC, in press, 1994.

2. D.A. Lukasak and R.M. Hart, "Strong Aluminum Alloy Saves Airframe Weight", Advanced Materials and Processes, Vol. 142, No. 10, pp. 46-49, 1991.

3. R.P. Gangloff, "Corrosion Fatigue Crack Propagation in Metals", in Environment-Induced Cracking of Metals, R.P. Gangloff and M.B. Ives, eds., NACE, Houston, TX, pp. 55-109, 1990.

4. M.O. Speidel, "Stress Corrosion and Corrosion Fatigue Crack Growth in Aluminum Alloys", in Stress Corrosion Research, H. Arup and R.N. Parkins, eds., Sijthoff & Noordhoff, Alphen aan den Rijn, The Netherlands, pp. 117-176, 1979.

5. N.J.H. Holroyd, "Environment-Induced Cracking of High-Strength Aluminum Alloys", in Environment-Induced Cracking of Metals, R.P. Gangloff and M.B. Ives, eds., NACE, Houston, TX, pp. 311-345, 1990.

6. J.A. Feeney, J.C. McMillan, and R.P. Wei, "Environmental Fatigue Crack Propagation of Aluminum Alloys at Low Stress Intensity Levels", Metallurgical Transactions A, Vol. 1, pp. 1741-1757, 1970.

7. R.P. Wei and J.D. Landes, "Correlation Between Sustained-Load and Fatigue Crack Growth in High-Strength Steels", Materials Research and Standards, Vol. 9, No. 7, pp. 25-27,44,46, 1969.

8. R.P. Wei and M. Gao, "Reconsideration of the Superposition Model for Environmentally Assisted Fatigue Crack Growth", Scripta Metallurgica et Materialia, Vol. 17, pp. 959-962, 1983.

9. A.M. Green and J.F. Knott, "Effects of Environment and Frequency on the Long Fatigue Crack Growth of Aluminum Alloy 7475", in Advances in Fracture Research, K. Salama, K. Ravi-Chandar, D.M.R. Taplin, and R.P. Rao, eds., Pergamon Press, Oxford, UK, pp. 1747-1756, 1989.

10. N.J.H. Holroyd and D. Hardie, "Factors Controlling Crack Velocity in 7000 Series Aluminum Alloys During Fatigue in an Aggressive Environment", Corrosion Science, Vol. 23, pp. 527-546, 1983.

11. A. Baldantoni, W. Wallace, M.D. Raizenne, and J.Y. Dickson, "The NRC Contribution to the FACT Programme", in The Fatigue in Aircraft Corrosion Testing (FACT) Programme, R.J.H. Wanhill, J.J. De Luccia, and M.T. Russo, eds., AGARD Report No. 713, NATO, pp. 162-173, 1985.

12. J.J. Thompson, E.S. Tankins, and V.S. Agarwala, "A Heat Treatment for Reducing Corrosion and Stress Corrosion Cracking Susceptabilities in 7XXX Aluminum Alloys", Materials Performance, Vol. 26, No. 6, pp. 45-52, 1987.

13. A.H. Le and R.T. Foley, "Stress Corrosion Cracking of 7075-T651 in Various Electrolytes - Statistical Treatment of Data Obtained Using DCB Precracked Specimens", Corrosion Science, Vol. 39, No. 10, pp. 379-383, 1983.

14. M.O. Speidel, "Stress Corrosion Cracking of Aluminum Alloys", Metallurgical Transactions A, Vol. 6A, pp. 631-651, 1975.

15. J. Rechberger, "The Transition from Stress Corrosion Cracking to Corrosion Fatigue in AA-7075 and AA-8090", Ph.D. Dissertation, University of British Columbia, Vancouver, Canada, 1989.

16. M.E. Mason and R.P. Gangloff, "Modeling Time-Dependent Corrosion Fatigue Crack Propagation in 7000 Series Aluminum Alloys", in FAA/NASA International Symposium on Advanced Structural Integrity Methods for Airframe Durability and Damage Tolerance, C. Harris, ed., NASA Conference publication 3274, Part 1, NASA-Langley Research Center, Hampton, VA, pp. 441-462, 1994.

17. Y.H. Kim and S.D. Manning, "A Superposition Model for Corrosion-Fatigue Crack Propagation in Aluminum Alloys", in Fracture Mechanics: Fourteenth Symposium - Volume 1: Theory and Analysis, ASTM STP 791, J.C. Lewis and G. Sines, eds., American Society for Testing and Materials, Philadelphia, PA, pp. 446-462, 1983.

18. R.D. Carter, E.W. Lee, E.A. Starke Jr., and C.J. Beevers, "The Effect of Microstructure and Environment on Fatigue Crack Closure of 7475 Aluminum Alloy", Metallurgical Transactions A, Vol. 15A, No. 3, pp. 555-563, 1984.

19. J. Albrecht, I.M. Bernstein, and A.W. Thompson, "Evidence for Dislocation Transport of Hydrogen in Aluminum", Metallurgical Transactions A, Vol. 13A, No. 5, pp. 811-819, 1982.

20. J.W. Watson and M. Meshii, "Hydrogen Transported by Dislocations in Aluminum Alloys", in Hydrogen Effects on Material Behavior, N.R. Moody and A.W. Thompson, eds., TMS-AIME, Warrendale, PA, pp. 241-248, 1990.

21. N.J.H. Holroyd and G.M. Scamans, "The Role of Magnesium During Environment-Sensitive Fracture of Aluminum Alloys", Scripta Metallurgica et Materialia, Vol. 19, pp. 915-916, 1985.

22. R.P. Wei, M. Gao, and P.S. Pao, "The Role of Magnesium in CF and SCC of 7000 Series Aluminum Alloys", Scripta Metallurgica et Materialia, Vol. 18, pp. 1195-1198, 1984.

23. R.E. Stoltz and R.M. Pelloux, "Inhibition of Corrosion Fatigue in 7075 Aluminum Alloys", Corrosion, Vol. 29, No. 1, pp. 13-17, 1973.

24. J.E. Dresty and O.F. Devereaux, "The Effect of Specimen Polarization on Fatigue Crack Growth Rates in 7075-T6 Aluminum", Metallurgical Transactions A, Vol. 4, No. 10, pp. 2469-2471, 1973.

25. N.J.H. Holroyd and D. Hardie, "Strain-Rate Effects in the Environmentally Assisted Fracture of a Commercial High-Strength Aluminum Alloy (7049)", Corrosion Science, Vol. 21, pp. 129-144, 1981.

26. M. Gao, P.S. Pao, and R.P. Wei, "Chemical and Metallurgical Aspects of Environmentally Assisted Fatigue Crack Growth in 7075-T651 Aluminum Alloy", Metallurgical Transactions A, Vol. 19A, pp. 1739-1750, 1988.

27. R.J. Selines and R.M. Pelloux, "Effect of Cyclic Stress Wave Form on Corrosion Fatigue Crack Propagation in Al-Zn-Mg Alloys", Metallurgical Transactions, Vol. 3, pp. 2525-2531, 1972.

28. L.M. Young, "Environment Assisted Cracking in Beta-Titanium Alloys", M.S. Thesis, University of Virginia, Charlottesville, VA, 1993.

29. H.D. Dill and C.R. Saff, Environment-Load Interaction Effects on Crack Growth, AFFDL-TR-78-137, McDonnell Douglas Corp., St. Louis, MO, 1978.

30. L.B. Vogelesang and J. Schijve, "Environmental Effects on Fatigue Fracture Mode Transitions Observed in Aluminum Alloys", Fatigue of Engineering Materials and Structures, Vol. 3, pp. 85-98, 1980.

31. H. Ouchi, J. Kobayashi, and I. Soya, "The Effects of Stress Waveform and Frequency on Fatigue Crack Growth Rates in a Steel Immersed in Seawater", in Environment-Assisted Fatigue, P. Scott, ed., Mechanical Engineering Publications, London, pp. 63-79, 1990.

32. J.D. Atkinson and T.C. Lindley, "The effect of Frequency and Temperature on Environmentally Assisted Fatigue Crack Growth Below K_{ISCC} in Steels", in The Influence of Environment on Fatigue, Mechanical Engineering Publications Limited, London, pp. 65-74, 1977.

33. J. Schijve, "Fundamental and Practical Aspects of Crack Growth Under Corrosion Fatigue Conditions", in The Influence of Environment on Fatigue, Mechanical Engineering Publications Limited, London, pp. vii-xiv, 1977.

34. R.P. Wei and R.P. Gangloff, "Environmentally Assisted Crack Growth in Structural Alloys: Perspectives and New Directions", in Fracture Mechanics: Perspectives and Directions, ASTM STP 1020, R.P. Wei and R.P. Gangloff, eds., ASTM, Philadelphia,PA, pp. 233-264, 1989.

35. W. Dietzel, K.H. Schwalbe, and D. Wu, "Application of Fracture Mechanics Techniques to the Environmentally Assisted Cracking of Aluminum 2024", in Fatigue and Fracture of Engineering Materials and Structures, Vol. 12, pp. 139-165, 1989.

36. F.P. Ford, "The Crack-Tip System and Its Relevance to the Prediction of Cracking in Aqueous Environments", in Environmental-Induced Cracking of Metals, R.P. Gangloff and M.B. Ives, eds., NACE, Houston, TX, pp. 139-165, 1990.

37. E.L. Colvin and M.R. Emptage, "The Breaking Load Method; Results and Statistical Modifications from ASTM Inter-Laboratory Test Program", in New Methods for Corrosion Testing of Aluminum Alloys, ASTM STP 1134, V.S. Agarwala and G. Ugiansky, eds., ASTM, Philadephia, PA, pp. 82-100, 1992.

38. H. Tada, P.C. Paris, and G.R. Irwin, The Handbook, Del Research Corp, St. Louis, MO, 1985.

39. J.K. Donald and J. Ruschau, "Direct Current Potential Difference Fatigue Crack Measurement Techniques", in Fatigue Crack Measurement: Techniques and Applications, K.J. Marsh, R.A. Smith, and R.O. Ritchie, eds., EMAS, Ltd., West Midlands, UK, pp. 11-37, 1991.

40. "E-647-91 Standard Test Method for Measurement of Fatigue Crack Growth Rates", in 1991 Annual Book of ASTM Standards, ASTM, Philadephia, PA, pp. 674-701, 1991.

41. J.K. Donald, FCGR5 User's and Programmer's Reference Manual, Fracture Technology Associates, Bethlehem, PA, 1992.

42. M.S. Domack, "Evaluation of K_{iscc} and da/dt Measurements for Aluminum Alloys Using Precracked Specimens", in Environmentally Assisted Cracking: Science and Engineering, ASTM STP 1049, W.B. Lisagor, T.W. Crooker, and B.N. Leis, eds., ASTM, Philadelphia, PA, pp. 391-409, 1990.

43. F.P. Ford and M. Silverman, "Effect of Loading Rate on Environmentally Controlled Cracking of Sensitized 304 Stainless Steel in High Purity Water", Corrosion, Vol. 36, No. 11, pp. 597-603, 1980.

44. P.S. Pao, S.J. Gill, and R.A. Bayles, "Effect of Ripple Loads on Stress-Corrosion Cracking in Al 7075 Alloys", Scripta Metallurgica et Materialia, Vol. 25, pp. 2085-2089, 1991.

45. B.A. Bayles, P.S. Pao, S.J. Gill, and G.R. Yoder, "Ripple-Load Cracking in Three Alloys Systems", in Systems Engineering Approach to Mechanical Failure Prevention, H.C. Pusey, S.C. Pusey, eds., Vibration Institute, Willowbrook, IL, pp. 167-176, 1993.

46. J.S. Santner and M. Kumar, "Corrosion-Fatigue Crack Propagation Rates in Commercial 7075 and P/M X7091 Aluminum Alloys", in Corrosion Fatigue: Mechanics, Metallurgy, Electrochemistry, and Engineering, ASTM STP 801, T.W. Crooker and B.N. Leis, eds., ASTM, Philadelphia, PA, pp. 229-255, 1983.

47. R.S. Piascik and R.P. Gangloff, "Environmental Fatigue of an Al-Li-Cu Alloy: Part I. Intrinsic Crack Propagation Kinetics in Hydrogenous Environments", Metallurgical Transactions A, Vol. 22A, No. 10, pp. 2415-2428, 1991.

48. I.M. Austen and E.F. Walker, "Quantitative Understanding of the Effects of Mechanical and Environmental Variables on Corrosion Fatigue Crack Growth Behavior", in The Influence of Environment on Fatigue, Mechanical Engineering Publications Limited, London, pp. 1-10, 1977.

49. M.G. Fontana, Corrosion Engineering, McGraw-Hill Book Company, New York, 1986.

50. P.E. Bretz, R.J. Bucci, R.C. Malcolm, and A.K. Vasudevan, "Constant-Amplitude Fatigue Crack Growth Behavior of 7XXX Aluminum Alloys", in Fracture Mechanics: Fourteenth Symposium, ASTM STP 791, J.C. Lewis and G. Sine, eds., ASTM, Philadelphia, PA, pp. 67-86, 1983.

51. J.R. Pickens and T.J. Langan, "The Effect of Solution Heat-Treatment on Grain Boundary Segregation and Stress-Corrosion Cracking of Al-Zn-Mg Alloys", Metallurgical Transactions A, Vol. 18, No. 10, pp. 1735-1744, 1987.

52. R.J. Gest and A.R. Troiano, "Stress Corrosion and Hydrogen Embrittlement in an Aluminum Alloy", Corrosion, Vol. 30, No. 8, pp. 274-279, 1974.

53. J. Albrecht, A.W. Thompson, and I.M. Bernstein, "The Role of Microstructure in Hydrogen-Assisted Fracture of 7075 Aluminum", Metallurgical Transactions A, Vol. 10, No. 11, pp. 1759-1766, 1979.

54. J. Albrecht, B.J. McTierman, I.M. Bernstein, and A.W. Thompson, "Hydrogen Embrittlement in a High-Strength Aluminum Alloy", Scripta Metallurgica et Materialia, Vol. 11, pp. 893-897, 1977.

55. A.W. Thompson, M.P. Mueller, and I.M. Bernstein, "Stress-Corrosion Cracking in Equiaxed 7075 Aluminum under Tension and Torsion Loading", Metallurgical Transactions A, Vol. 24, No. 11, pp. 2569-2575, 1993.

56. F.P. Ford, "Status of Research on Environmentally Assisted Cracking in LWR Pressure Vessel Steels", Journal of Pressure Vessel Technology, Vol. 110, No. 5, pp. 113-128, 1988.

57. J.W. Hutchinson, "Fundamentals of the Phenomenological Theory of Nonlinear Fracture Mechanics", Transactions of the ASME, Vol. 50, No. 12, pp. 1042-1051, 1983.

58. D.L. Davidson and J. Lankford, "The Effects of Aluminum Alloy Microstructure on Fatigue Crack Growth", Materials Science and Engineering, Vol. 74, pp. 189-199, 1985.

59. T. Shoji, H. Takahashi, M. Suzuki, and T. Kondo, "A New Parameter for Characterizing Corrosion Fatigue Crack Growth", Transactions of the ASME, Vol. 103, pp. 298-304, 1981.

60. G.S. Frankel, B.M. Rush, C.V. Jahnes, C.E. Farrell, A.J. Davenport, and H.S. Isaacs, "Repassivation Transients Measured with Thin Film Breaking Electrodes", Journal of the Electrochemical Society, Vol. 138, No. 2, pp. 643-644, 1991.

61. A.J. Bursle and E.N. Pugh, "An Evaluation of Current Models for the Propagation of Stress-Corrosion Cracks", in Environment-Sensitive Fracture of Engineering Materials, Z.A. Foroulis, ed., The Metallurgical Society of AIME, New York,NY, pp. 18-47, 1979.

62. K. Papp and E. Kovacs-Csetenyi, "Diffusion of Hydrogen in High Purity Aluminum", Scripta Metallurgica et Materialia, Vol. 15, pp. 161-164, 1981.

63. R.A. Outlaw, D.T. Peterson, and F.A. Schmidt, "Diffusion of Hydrogen in Pure Large Grain Aluminum", Scripta Metallurgica et Materialia, Vol. 16, pp. 287-292, 1982.

64. C.R. Shastry, M. Levy, and A. Joshi, "The Effect of Solution Treatment Temperature on Stress Corrosion Susceptability of 7075 Aluminum Alloy", Corrosion Science, Vol. 21, No. 9, pp. 673-688, 1981.

65. P.N. Anyalebechi, D.E.J. Talbot, and D.A. Granger, "Hydrogen Solution in Al-Li Alloys", in Light-Weight Alloys for Aerospace Applications, E.W. Lee, E.H. Chia, and N.J. Kim, eds., TMS-AIME, Warrendale, PA, pp. 249-270, 1989.

REPORT DOCUMENTATION PAGE

Form Approved
OMB No. 0704-0188

1. AGENCY USE ONLY (*Leave blank*)	2. REPORT DATE	3. REPORT TYPE AND DATES COVERED
	October 1995	Contractor Report

4. TITLE AND SUBTITLE
Time-Dependent Corrosion Fatigue Crack Propagation in 7000 Series Aluminum Alloys

5. FUNDING NUMBERS
G NAG1-745
WU 297-40-00-01

6. AUTHOR(S)
Mark E. Mason

7. PERFORMING ORGANIZATION NAME(S) AND ADDRESS(ES)
University of Virginia
School of Engineering and Applied Science
Charlottesville, VA 22903

8. PERFORMING ORGANIZATION REPORT NUMBER

9. SPONSORING / MONITORING AGENCY NAME(S) AND ADDRESS(ES)
National Aeronautics and Space Administration
Langley Research Center
Hampton, VA 23681-0001

10. SPONSORING / MONITORING AGENCY REPORT NUMBER
NASA CR-198230

11. SUPPLEMENTARY NOTES
Langley Technical Monitor: Robert S. Piascik
Final Report

12a. DISTRIBUTION / AVAILABILITY STATEMENT
Unclassified - Unlimited

Subject Category 24

12b. DISTRIBUTION CODE

13. ABSTRACT (*Maximum 200 words*)

The goal of this research is to characterize environmentally assisted subcritical crack growth for the susceptible short-longitudinal orientation of aluminum alloy 7075-T651, immersed in acidified and inhibited NaCl solution. This work is necessary in order to provide a basis for incorporating environmental effects into fatigue crack propagation life prediction codes such as NASA-FLAGRO (NASGRO). This effort concentrates on determining relevant inputs to a superposition model in order to more accurately model environmental fatigue crack propagation.

14. SUBJECT TERMS
Corrosion fatigue; Environmental fatigue; Time dependence; Stress corrosion; NASGRO; Crack propagation

15. NUMBER OF PAGES
175

16. PRICE CODE
A08

17. SECURITY CLASSIFICATION OF REPORT	18. SECURITY CLASSIFICATION OF THIS PAGE	19. SECURITY CLASSIFICATION OF ABSTRACT	20. LIMITATION OF ABSTRACT
Unclassified	Unclassified		